Research in Optoelectronics (A)

2015 Reprints of
Professor Larry A. Coldren
and Collaborators

Research in Optoelectronics (A)

Reprints published in 2015

by

Professor Larry A. Coldren

and Collaborators

Published as

Technical Report   # ECE 16-01

of

The Department of Electrical & Computer Engineering

The University of California

Santa Barbara, CA 93106

Phone: (805) 893-4486

Fax: (805) 893-4500

E-mail: coldren@ece.ucsb.edu

http://www.ece.ucsb.edu/Faculty/Coldren/

Introduction:

This volume contains papers published by Professor Coldren and collaborators in various journals and conferences in calendar year 2015. Any publication on which Prof. Coldren is named as a co-author is included. The work has a focus on III-V compound semiconductor materials as well as the design and creation of photonic devices and circuits using these materials. The characterization of these devices and circuits within systems environments is also included in some cases.

As in the past, the reprints have been grouped into several of areas. This year these are: **I. Photonic Integrated Circuits,** and **II. VCSELs and Cavity QED.** Most of the work is in the first area, which has been further subdivided into *1A. Beam Sweeping; 1B. Optical Phase-Locked Loops; 1C. Optical Phase-Sensitive-Amplifiers* and*; 1D. Signal Processing with Active Micro-rings.* The second area has also been sub-divided into *IIA. VCSEL Interconnects;* and *IIB. Cavity Quantum Electrodynamics.*

The work was performed with funding from several federal grants, some gift funds from industry, and support from the Kavli Endowed Chair in Optoelectronics and Sensors. Some of the PIC work was funded by the MTO and DSO Offices of DARPA, the VCSEL growths were carried out in the UCSB MBE lab with the support of Prof. Gossard and other personnel there; PIC and VCSEL fabrication was performed in the UCSB Nanofab facility partially supported by the NSF-NNIN. The collaboration of Freedom Photonics in some of the work is also gratefully acknowledged.

Sub-section (*IA.*) contains a Si-photonics optical beam sweeping paper on work led by Prof. John Bowers. It describes the design and fabrication of an integrated chip to produce a free-space beam that can be swept in two dimensions over a 10° range. The hybrid Si-photonic chip contains the widely-tunable laser source, 32 waveguides with surface-emitting gratings , and it is one of the largest such chips ever created.

The second section (*IB.*) contains a conference paper on a highly integrated coherent receiver that uses an optical-phase-locked loop to phase lock its local oscillator to the carrier of the incoming signal. No DSP is utilized, and bit-error-rates $< 10^{-12}$ for data rates up to 35 Gb/s were demonstrated.

The third section (*1C.*) contains four articles—two conference and two journal papers—on optical phase-sensitive amplifiers. Figure 1 shows a schematic and photo of the PIC used along with some key results. The experiments involved using two coherently related optical pumps and a highly-saturated semiconductor optical amplifier (SOA) as the nonlinear medium to demonstrate 'phase-sensitive' amplification.   The pumps are initially created external to the chip as sidebands from an intensity modulated signal. These sidebands then injection-lock two tunable lasers on the PIC—SGDBR-1 and SGDBR-2. These pumps then are recombined with the signal which has passed through a phase modulator before entering the SOA as well as some reference waveguides. When the SOA is highly saturated, there is little linear gain and nearly noiseless phase-sensitive amplification (PSA) should be possible.

This PSA gain is indicated by an interference of the signal with the generated conjugate signal when the phase of the signal is shifted. This is shown in part (c) –blue curve.

(a)

(b)

(c)
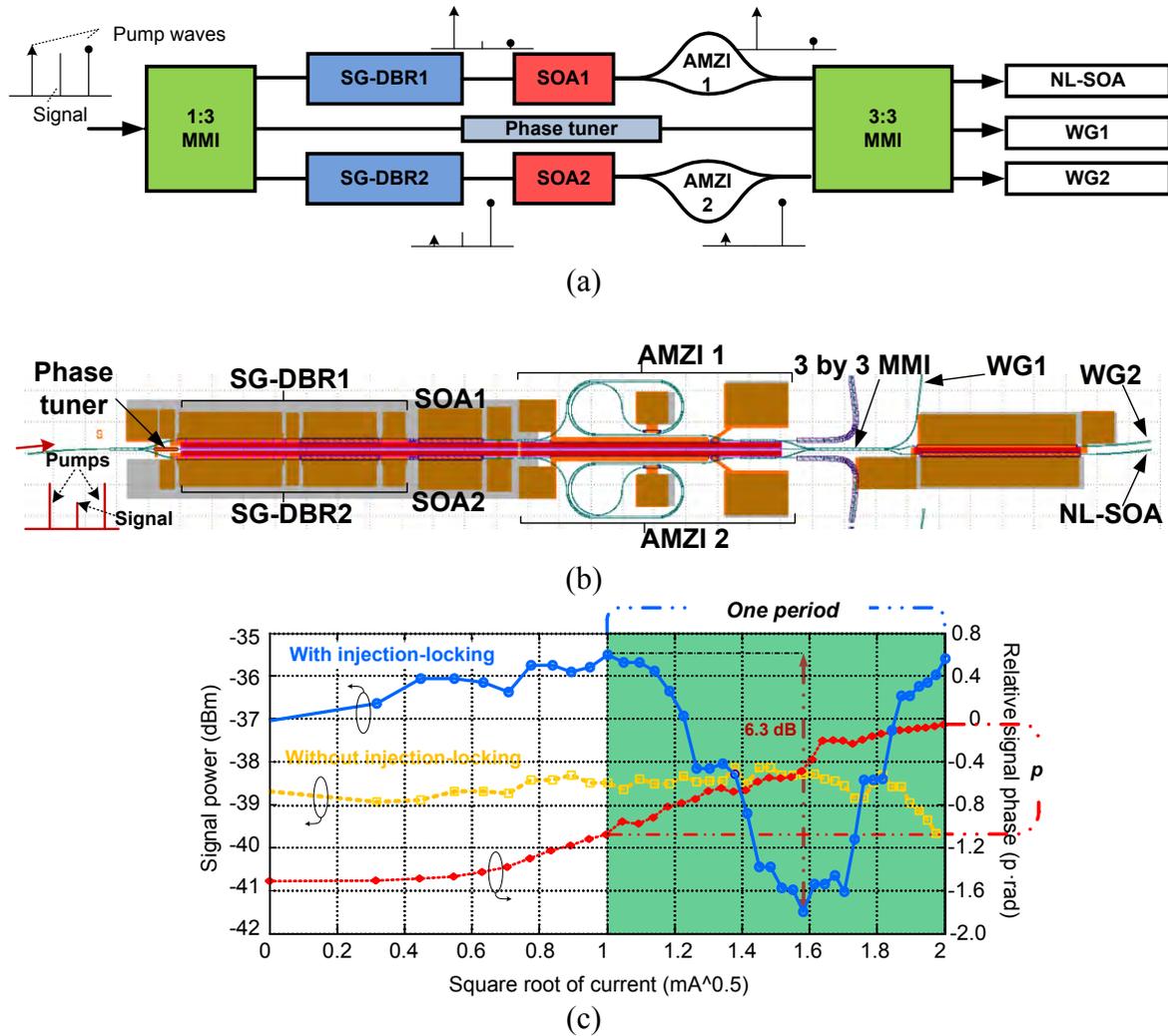
Figure 1. Single-chip phase-sensitive amplifier. (a) Schematic; (b) photo; (c) data. For (c) the blue curve shows the expected interference between the signal wave and its generated conjugate as the current to the phase tuner is increased; the yellow curve is for the SGDBRs pump lasers not injection locked (not phase coherent); the red curve is the measured phase shift applied to the signal wave. Note that the square root of the current to the phase tuner is plotted because the phase shift should be linear with this; however, there is an initial offset due to stored interface charge in the device.

The fourth sub-section in the PIC group (*1D*.) gives a news article that summarizes a few experiments performed by Prof. Yao's group at the Univ. of Ottawa using integrated active programmable ring resonator filters that were designed and fabricated in Prof. Coldren's lab a few years ago. Two kinds of all-optical temporal integrators were demonstrated, each capable of calculating the time integral of an arbitrary input optical waveform having bandwidths exceeding what could be handled by electronic circuits. A full-length *Nature-Photonics* paper has been accepted on this work and will appear in February of 2016.

In Section **II. VCSELs and Cavity QED**, high-Q vertical cavities grown on GaAs by MBE are used first to make efficient vertical-cavity lasers and then in cavity quantum electrodynamics experiments in which electronic transitions of a quantum-dot placed in the cavity are modified by optical coupling.

The first paper in sub-section (*IIA.*) summarizes an invited paper presented at the *OCOI Topical Meeting* that discusses the use of VCSELs for chip-to-chip and on-chip optical interconnects enabled by 2.5 and 3-D integration techniques using interposer technology. This technology facilitates the use of different chiplets to be stably combined on a common Si platform. Some chiplets may be electronic ICs, some may be photonic, some of these may be composed mainly of Si, others mainly of GaAs or InP. The talk also included work on polarization modulation of VCSELs that can double the information carried on a single beam of light.

The second sub-section (*IIB.*) consists of three papers on the cavity QED work led by Prof. Dirk Bouwmeester. The first uses an asymmetric oxide aperture to provide polarization degenerate cavity modes. The quantum-dot transition was tuned through the cavity resonance via the quantum-confined Stark effect with an applied electric field. The second paper presents a technique that enables the determination of the coherence and the phase of light that is transmitted through a polarization degenerate coupled quantum-dot/cavity system. The third paper discusses the effects of charges trapped at the oxide aperture on cavity QED experiments.

Professor Coldren's Group
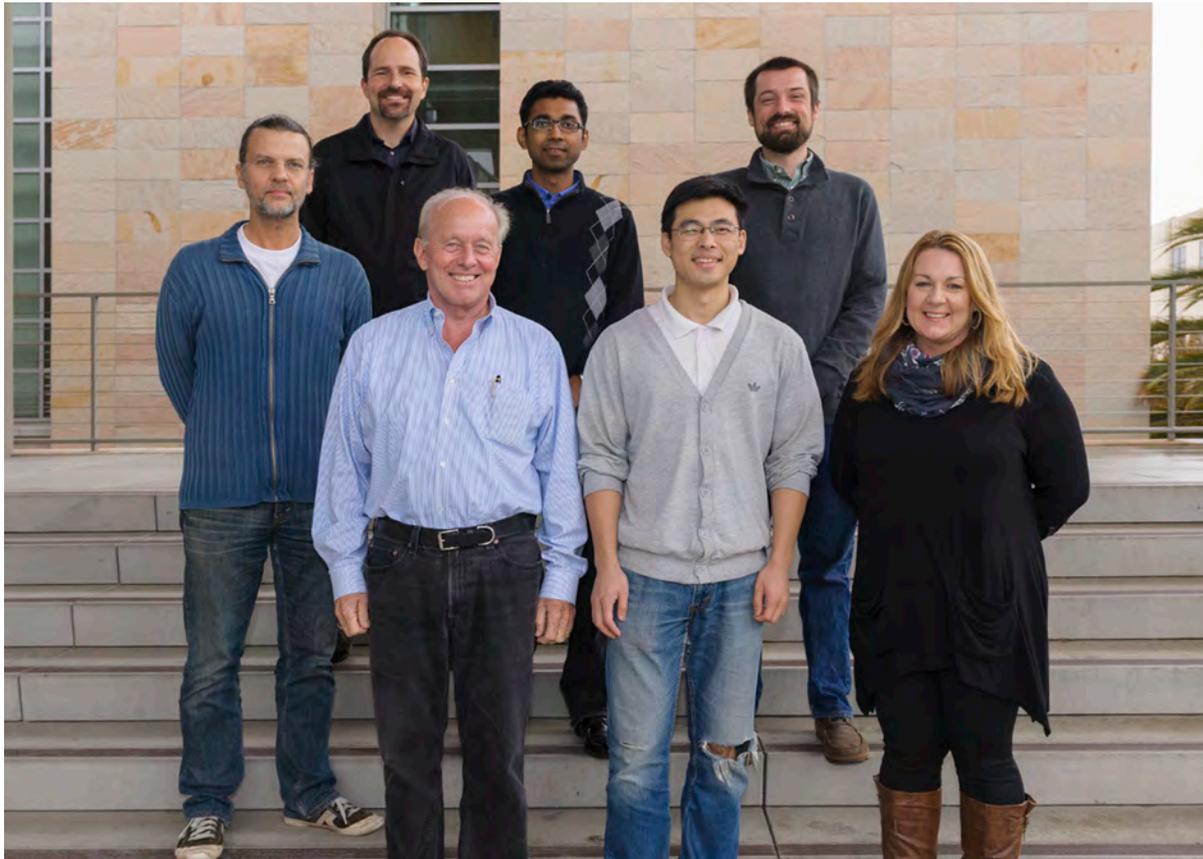
Back Row: Leif Johansson, Milan Mashanovitch, Shamsul Arafin, Danilo Dadic
Front Row: Professor Larry Coldren, Wangzhe Li, Amanda Miller

Professor Coldren's Group

I.   <u>*Researchers*</u>

L. Johansson	Associate Research Engineer, UCSB
M. Masanovic	Associate Project Scientist, UCSB
S. Arafin	Assistant Project Scientist, UCSB
W. Li	Postdoctoral Scholar, UCSB

II.   <u>*Students*</u>

D. Dadic	Graduate Student Researcher

III.   <u>*Staff*</u>

D. Cohen	Principal Development Engineer, reports to Prof Nakamura
A. Miller	Center Assistant, OTC

Collaborators

I.   <u>*Faculty*</u>

J. Bowers	UCSB
M. Rodwell	UCSB
D. Bouwmeester	UCSB
J. Yao	University of Ottawa
M. Li	China Academy of Science
M.P. van Exter	Leiden University, Netherlands
A. Mecozzi	University of L'Aquila via Vetoio 1, L'Aquila, Italy
M. Vasilyev	University of Texas at Arlington
J. Azana	Universidad Politecnica de Madrid, Spain

II.   *Researchers*

M. Lu	Infinera (former Postdoctoral Scholar)
A. Barve	JDS Uniphase (former Postdoctoral Scholar)
E. Bloch	Research Scientist, Technion Israel and UCSB (Rodwell)
E. Norberg	Member of Staff, Aurrion, Inc. (former Graduate Student)
J. Peters	Sr. Development Engineer, UCSB (Bowers)
J. Parker	Photonic Device Scientist, Freedom Photonics (former Graduate Student)
R. Guzzon	Photonic Systems Engineer, Aurrion, Inc.
W. Löffler	Researcher at Leiden University, Netherlands

III.   *Collaborating Students*

J. Bovington	UCSB, Bowers
M. Davenport	UCSB, Bowers
J. Hulme	UCSB, Bowers
J. Doylend	UCSB, Bowers, now at Intel
M. Heck	UCSB, Bowers, now a Professor at Denmark Aarhus
H. Park	UCSB, Rodwell
M. P. Bakker	Leiden University, Netherlands
T. Ruytenberg	Leiden University, Netherlands
H. Snijders	Leiden University, Netherlands
C. Antonelli	University of L'Aquila via Vetoio 1, L'Aquila, Italy
W. Liu	University of Ottawa, Canada
N.B. Huang	Shanghai University, Shanghai
N. Zhu	Chinese Academy of Sciences, China

Table of Contents:

I. Photonic Integrated Circuits

IA. Beam Sweeping

IB. Optical Phase-Locked Loops

IC. Optical Phase-Sensitive-Amplifiers

x

I. Photonic Integrated Circuits

A. Beam Sweeping

Fully integrated hybrid silicon two dimensional beam scanner

**J. C. Hulme,[*] J. K. Doylend, M. J. R. Heck, J. D. Peters, M. L. Davenport,
J. T. Bovington, L. A. Coldren, and J. E. Bowers**

Electrical & Computer Engineering Department University of California Santa Barbara, California 93106, USA
[*]jaredhulme@ece.ucsb.edu

Abstract: In this work we present the first fully-integrated free-space beam-steering chip using the hybrid silicon platform. The photonic integrated circuit (PIC) consists of 164 optical components including lasers, amplifiers, photodiodes, phase tuners, grating couplers, splitters, and a photonic crystal lens. The PIC exhibited steering over 23° x 3.6° with beam widths of 1° x 0.6°.

References and links

1. M. J. R. Heck, J. F. Bauters, M. L. Davenport, J. K. Doylend, S. Jain, G. Kurczveil, S. Srinivasan, Y. Tang, and J. E. Bowers, "Hybrid silicon photonic integrated circuit technology," IEEE J. Sel. Top. Quantum Electron. **19**, 6100117 (2013).
2. K. Van Acoleyen, W. Bogaerts, J. Jágerská, N. Le Thomas, R. Houdré, and R. Baets, "Off-chip beam steering with a one-dimensional optical phased array on silicon-on-insulator," Opt. Lett. **34**(9), 1477–1479 (2009).
3. K. Van Acoleyen, H. Rogier, and R. Baets, "Two-dimensional optical phased array antenna on silicon-on-Insulator," Opt. Express **18**(13), 13655–13660 (2010).
4. D. Kwong, A. Hosseini, Y. Zhang, and R. T. Chen, "1 × 12 Unequally spaced waveguide array for actively tuned optical phased array on a silicon nanomembrane," Appl. Phys. Lett. **99**(5), 051104 (2011).
5. J. K. Doylend, M. J. Heck, J. T. Bovington, J. D. Peters, L. A. Coldren, and J. E. Bowers, "Two-dimensional free-space beam steering with an optical phased array on silicon-on-insulator," Opt. Express **19**(22), 21595–21604 (2011).
6. J. Sun, E. Timurdogan, A. Yaacobi, E. S. Hosseini, and M. R. Watts, "Large-scale nanophotonic phased array," Nature **493**(7431), 195–199 (2013).
7. J. K. Doylend, M. J. R. Heck, J. T. Bovington, J. D. Peters, M. L. Davenport, L. A. Coldren, and J. E. Bowers, "Hybrid III/V silicon photonic source with integrated 1D free-space beam steering," Opt. Lett. **37**(20), 4257–4259 (2012).
8. J. K. Doylend, M. J. R. Heck, J. T. Bovington, J. D. Peters, M. L. Davenport, and J. E. Bowers, "Hybrid III-V silicon photonic steerable laser," IEEE Photonics Conference, Sept 23–27, 2012.
9. J. K. Doylend, M. J. R. Heck, J. T. Bovington, J. D. Peters, M. L. Davenport, L. A. Coldren, J. E. Bowers, "Hybrid silicon free-space source with integrated beam steering," Proc. SPIE 8629, Silicon Photonics VIII, (2013).
10. A. Yaacobi, J. Sun, M. Moresco, G. Leake, D. Coolbaugh, and M. R. Watts, "Integrated phased array for wide-angle beam steering," Opt. Lett. **39**(15), 4575–4578 (2014).
11. C. Zhang, S. Srinivasan, Y. Tang, M. J. R. Heck, M. L. Davenport, and J. E. Bowers, "Low threshold and high speed short cavity distributed feedback hybrid silicon lasers," Opt. Express **22**(9), 10202–10209 (2014).
12. J. C. Hulme, J. K. Doylend, and J. E. Bowers, "Widely tunable Vernier ring laser on hybrid silicon," Opt. Express **21**(17), 19718–19722 (2013).
13. J. K. Doylend, M. J. R. Heck, J. T. Bovington, J. D. Peters, and J. E. Bowers, "Free-space beam steering using silicon waveguide surface gratings," IEEE Photonics Conference, 547–548 (2011).
14. H. Park, Y.-H. Kuo, A. W. Fang, R. Jones, O. Cohen, M. J. Paniccia, and J. E. Bowers, "A Hybrid AlGaInAs-Silicon Evanescent Amplifier," IEEE Photon. Technol. Lett. **19**(4), 230–232 (2007).
15. A. W. Fang, M. N. Sysak, B. R. Koch, R. Jones, E. Lively, Y.-H. Kuo, D. Liang, O. Raday, and J. E. Bowers, "Single-Wavelength Silicon Evanescent Lasers," IEEE J. Sel. Top. Quantum Electron. **15**(3), 535–544 (2009).
16. J. K. Doylend, P. E. Jessop, and A. P. Knights, "Silicon photonic dynamic optical channel leveler with external feedback loop," Opt. Express **18**(13), 13805–13812 (2010).

1. Introduction

Free-space beam-steering is important for light detection and ranging (LIDAR), free space communications, and has potential applications for holographic displays and biomedical imaging. LIDAR employs a moving laser beam to sample the environment for optical "echoes" and rapidly collect high resolution three-dimensional images. One can imagine a world where every vehicle employs a LIDAR system for improved safety, for data collection, or to provide feedback for automated driving. This will require advancement beyond the current state of LIDAR technology – which typically costs tens of thousands of dollars and is so large that is has to be mounted on the roof of the vehicle – to LIDAR technology that can be deployed on bumpers or door frames. However, this is only possible with the great reduction in size, weight, cost, and mechanical wear that a fully-integrated solid-state beam-steering chip provides. As integration of photonic elements increases [1], it becomes possible to integrate a phased array beam steering system on a chip, with much higher stability and performance with lower cost than has been previously possible.

Free-space beam steering using silicon photonic chips has been demonstrated using off-chip lasers [2–4], including 2D beam steering in [5] through the use of optical phased arrays and a fiber-coupled input. 2D steering using a two-dimensional phased array has also been demonstrated with an off-chip laser [6], but all of the above required a fiber-coupled input and an off-chip laser, rendering the device impractical as a single-chip beam-steering solution. 1D steering with an on-chip laser – i.e. a truly "steerable laser" – has been demonstrated on the hybrid silicon platform with the laser, amplifiers, phase tuners, and phased array all integrated and fabricated on-chip by Doylend et al. [7–9], but thus far 2D steering using an on-chip laser has not been achieved.

In this paper we present the first fully integrated two-dimensional steerable laser chip on a hybrid III-V/silicon platform which also, to our knowledge, combines the largest number to date of integrated components (164) on a silicon substrate with integrated lasers. This chip includes 2 tunable lasers, 34 amplifiers, and 32 photodiodes utilizing III-V material, as well as 32 phase shifters, 31 MMI couplers and a graded index (GRIN) lens in the silicon-on-insulator (SOI) layer. These combine wavelength tuning with an optical phased array to accomplish 2D beam-steering without the need for moving parts or an external laser.

2. Concept

Beam-steering and shaping can be performed with an optical phased array (OPA) by splitting the output from a laser into an array of phase tuners and emitter elements. The far-field beam shape can be arbitrarily chosen by individually tuning the phase of each channel, however the quality of the beam is subject to limitations due to the finite emitter size and number of emitter elements. In the case of a two-dimensional OPA the number of control elements rapidly scales beyond reasonable numbers for a photonic integrated circuit since in general N^2 steered elements are required for beam-forming in two axes, where N is the number of elements required for beam-forming in a single axis with the desired beam quality [6]. Recently a 1D OPA has demonstrated beam-steering using a single control element by cascading phase-shifters in series [10]. Although this cascaded method could be applied to 2D OPAs it is limited in the second dimension by large pixel size. Additionally, because this method does not control individual phase shifters it is more susceptible to thermal crosstalk such as is common when integrating gain elements on-chip.

A more efficient method of 2D beam-steering can be performed by tuning the wavelength of the light emitted from a surface grating. As the light propagates through the emitter, power scatters off each tooth with a phase delay dependent on the effective index of the mode and the wavelength of light. This effectively becomes a series of closely packed pixels that add up in the far field as a 1D beam. The angle of emission (θ) can be calculated from the grating period (Λ), the waveguide effective index (n_{eff}), and the wavelength (λ) as shown in Eq. (1)

$$\sin\theta = \frac{\Lambda n_{eff} - \lambda}{\Lambda} \qquad\qquad (1)$$

By combining an OPA with grating emitters and a tunable laser, 2D beam-steering can be achieved with linear scaling of the number of control elements, in fact the number of required elements would be only N + M, where N is the number of phase-tuned elements required for high-quality beam-forming in one axis and M is the number of controllable elements in the tunable laser (typically fewer than 4). We use ψ for the steering axis determined by the OPA, and θ for the axis determined by wavelength via the Bragg equation.
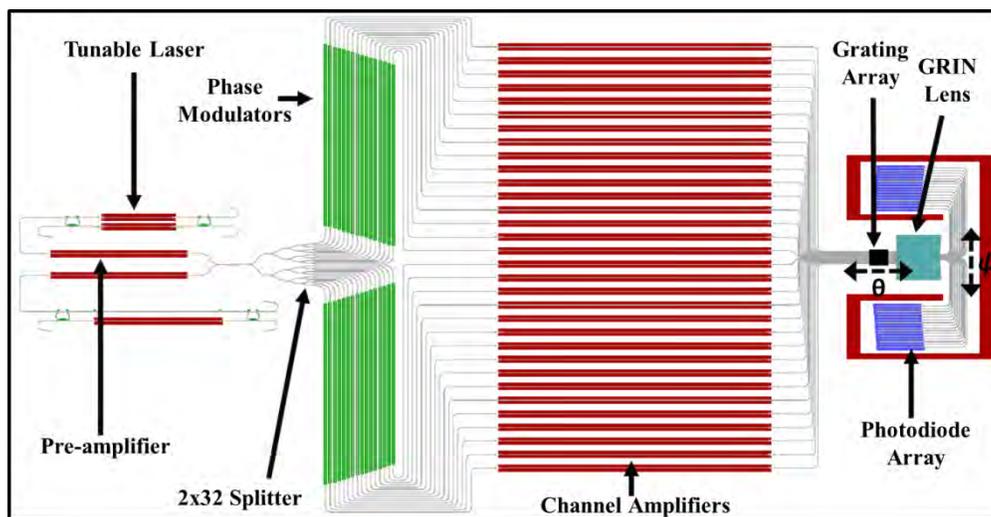
Fig. 1. Layout of the fully integrated PIC. Redundant tunable laser sources are followed by semiconductor optical amplifier (SOA) pre-amplifiers. The signal passes through a 32 channel splitter and is then tuned in both phase and amplitude for each channel. The channels feed a surface grating array where the beam is emitted at an angle determined by wavelength in the θ axis and by relative phase in the ψ axis. A graded index lens images the remaining beam power into the far field and where it is measured by a photodiode array for on-chip feedback.

3. Design

The PIC design begins with two redundant tunable Vernier ring lasers (discussed further below and in Fig. 1). The redundancy can be used to switch between lasers with different tuning ranges to create a much wider wavelength-tuning range overall and thus a wider angular steering range in the θ axis. The laser signal passes through a pre-amplifier prior to being split into 32 channels, each with a phase modulator and an amplifier. For current injection phase tuning, one expects phase-dependent losses, which can be compensated for by the amplifiers to avoid beam distortion. It should be noted that an equal power output from all channels is not ideal for side mode suppression (e.g. as compared with a Gaussian power distribution). Regardless of the desired power distribution, the amplifier array can be used to achieve the desired power distribution with both static adjustments for waveguide and splitter losses and dynamic adjustment for phase tuning induced losses. The optimized beam is emitted from the device via etched waveguide gratings. Any remaining power in the waveguides passes through a graded index (GRIN) lens that images the far field and couples to a photodiode array for on-chip feedback. These elements will now be described in more detail.

3.1 Components

The gain elements for the tunable laser and semiconductor optical amplifier (SOA) are similar to the design reported by Zhang et al. [11] where the mode is shifted upward as it enters a bonded III/V region to partially overlap the pumped quantum wells.

Two laser designs were placed in the PIC and were split between a tested design [12] with 41 nm tuning range and 5.5 mW output power and a new optimized design that is expected to perform similarly but with lower thresholds and higher output powers. Both lasers employ two ring resonators coupled by two bus waveguides with a gain region. The new design omits the gain region from one of the waveguides to reduce losses incurred at the tapered III/V section and replaces it with a thermal phase tuner. The gain region length was also increased from 0.8 to 1.4 mm in the new design to compensate for removing the second gain region. Schematics of the lasers are shown in Fig. 2.
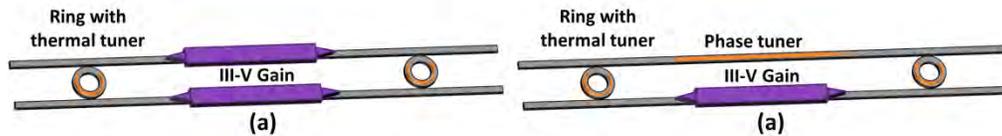
Fig. 2. Schematic of tunable Vernier ring laser with (a) two gain regions and (b) one gain region.

The pre-amplifiers were made 1.5 mm long for amplification of the signal prior to entering the splitter, and the channel amplifiers were made to be 3 mm long to maximize output power from the PIC. It was expected that increasing the length of the pre-amplifier beyond 1.5 mm would not significantly increase the gain due to saturation of the SOA, however the decreased signal following the splitter was expected to see linear gain in the 3 mm amplifiers.

The phase modulators were based on a *p-i-n* silicon diode design [9]. To reduce series resistance, the doped regions were placed 6 μm apart instead of 11, allowing these diodes to move past thermal time constants and rapidly tune using electro-optic phase shifting. This also reduced cross-talk between channels, greatly simplifying the optimization of the output beam.

3.2 Channel output spacing and count

A uniformly spaced OPA generates a main beam as well as undesired side lobes that emit at different angles. These side lobes limit the useful field of view. For a given wavelength, the angular separation between the main lobes and the side lobes is determined by the spacing between emitters as shown in Fig. 3. Thus, decreasing the emitter pitch will increase the useful range of the device until the pitch is limited by waveguide width and mode size.

However, decreasing the total width of the emitter array by decreasing the emitter spacing increases the beam width and reduces the number of resolvable spots. The effect is such that decreasing emitter pitch will keep the number of resolvable spots nearly constant, even though it will increase the field of view, because as the field of view increases so does the size of the spots. A simple way to increase the number of resolvable spots is to keep the emitter pitch small while increasing the array width by increasing the number of channels. However, this adds control complexity since each channel requires individual phase (and possibly amplitude) tuning. Hence 2D steering with a tunable laser and 1D OPA – for which the number of channels scales linearly with array size - becomes much more convenient than a 2D OPA for which the number of channels (and therefore control complexity) scales quadratically with array size.

4
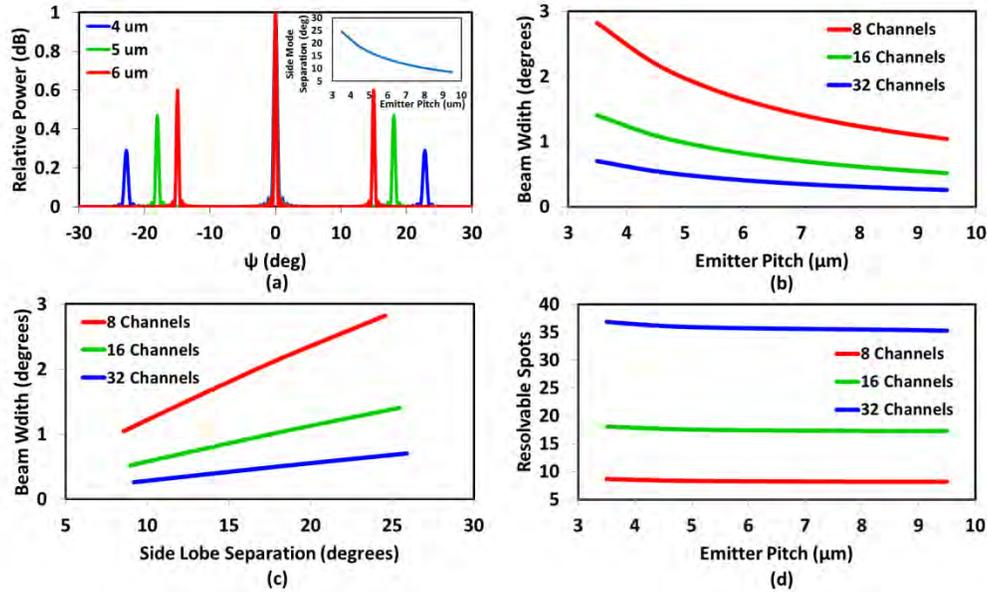
Fig. 3. (a) Calculated angular power distribution for 4, 5, and 6 μm spacing between emitters with an inset of the calculated side mode separation between main lobe peak and side lobe (measured where the side lobe intensity rises to −10 dB relative to main lobe peak which is where the useful field of view ends) vs. emitter pitch, (b) calculated far field beam full width half max (FWHM) vs. emitter pitch for 8, 16, and 32 channels, (c) calculated beam FWHM vs. side lobe separation based on varying emitter pitch, and (d) calculated number of resolvable spots (i.e. side lobe separation divided by beam width) vs. side lobe separation based on varying emitter pitch.

Another approach to increasing side mode suppression is to vary the emitter spacing. For example, using a Gaussian distribution for waveguide pitch results in a very different side mode profile (Fig. 4) with the first major side lobe reduced to the level of the other side lobes. As the chosen angle shifts and the main lobe decreases in intensity the difference becomes even more noticeable. At 0° the uniform array is calculated to contain 53% of the emitted power in the main lobe with a side mode suppression ratio (SMSR) of 5.4 dB, while at 10° it contains only 46% of power with an SMSR of 0.5 dB. The Gaussian array is more uniform across the tuning space with a much better SMSR – the main lobe contains 48% at 0° with an SMSR of 13.9 dB and 45% at 10° with an SMSR of 8.2 dB. However within a field of view that excludes the first major side lobe, the uniform array maintains a higher SMSR over a greater tuning range.

Calculations were made for other configurations, but the uniform and Gaussian array spacing appeared most promising and were selected for fabrication. The uniform array was designed with a 4 μm emitter pitch and 126 μm total width, and the Gaussian array was designed with a 3.4 μm center emitter pitch, 7.1 μm outer emitter pitch, and 144 μm total width. Both arrays used emitters consisting of gratings with a pitch of 550 nm shallowly etched on 2.3 μm wide waveguides. At this pitch the emitters are expected to tune 0.127 ± 0.02 ° / nm at wavelengths of 1555 to 1605 nm [13].
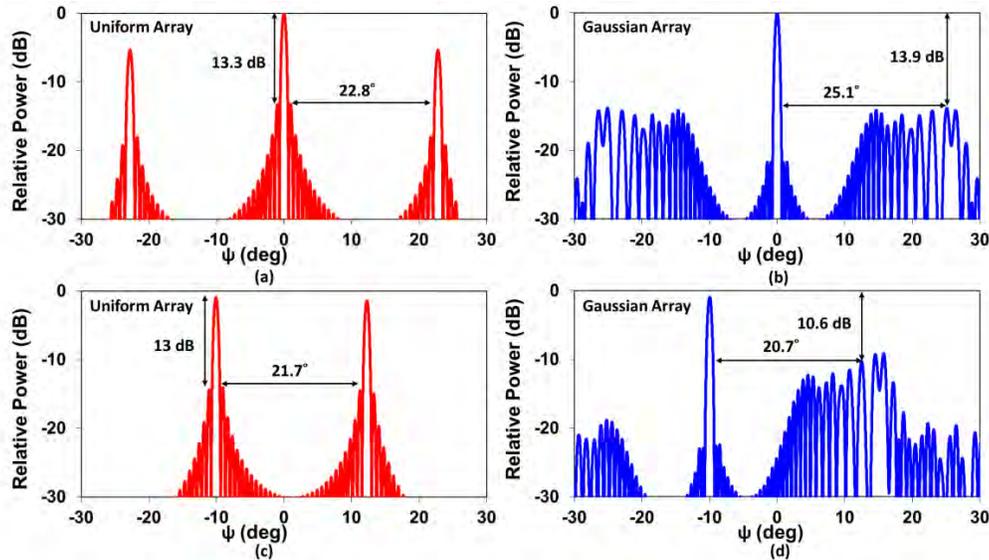
Fig. 4. Calculated far field for (a) uniform and (b) Gaussian emitter spacing using no relative phase or output power differences between channels. Calculated far field for (c) uniform array with linear relative phase shift and (d) Gaussian array with linear relative phase shift adjusted for irregular spacing to tune the main lobe to −10°. The Gaussian array performs better when considering the full signal, but (c)-(d) illustrate the larger tuning range of the uniform array within a field of view while maintaining greater than 10 dB side mode suppression.

3.3 Lens and photodiode array

Most of the optical measurements on this PIC were performed by directly measuring the output beam off-chip using an infrared camera and a lens system as described in Section 5. This technique works well for initial characterization but is insufficient for periodic monitoring, calibration, and control of a field device. Temperature variations can affect the channel amplifier gain, which necessitates a shift in injection current to maintain the proper power distribution. Shifting the injection current also shifts the phase so the phase modulators also require dynamic control. Use of a beam-steering chip requires a feedback mechanism that does not interfere with the output signal and is included on-chip. Such a device has been demonstrated in [16] for power from a 2-channel interferometer, but for the PIC described in this work a means of tracking the interference pattern between all 32 channels was required. To that end, an on-chip measurement system was designed using a 1D graded index lens to image the far field of the ψ axis. The imaged field is placed at the beginning of an array of waveguides that feed a photodiode array to measure the beam angle (Fig. 1).

The lens was fabricated by shallowly etching sub-wavelength holes of varying diameter in an SOI slab that was then covered in PECVD SiO_2. The hole diameters were selected so as to vary the effective index of the slab parabolically across its width, effectively forming a graded index (GRIN) lens. Figure 5 shows a cross-section of the calculated index profile and the simulated intensity throughout the lens with zero relative phase shift between channels.

The waveguides feeding the photodiode array were placed at the calculated focal length (473 μm) with a total width of 64 μm. There are 32 photodiodes in the array that are expected to span 41° in the far field (the total expected width between the first-order side lobes) with a resolution of 1.3°. This resolution is not high enough to resolve individual spots but is sufficient for coarse recalibration of phase alignment from thermal fluctuations.

A calculation of the beam intensity at the lens focal point is shown in Fig. 6 for several different values of linear phase difference between adjacent channels.
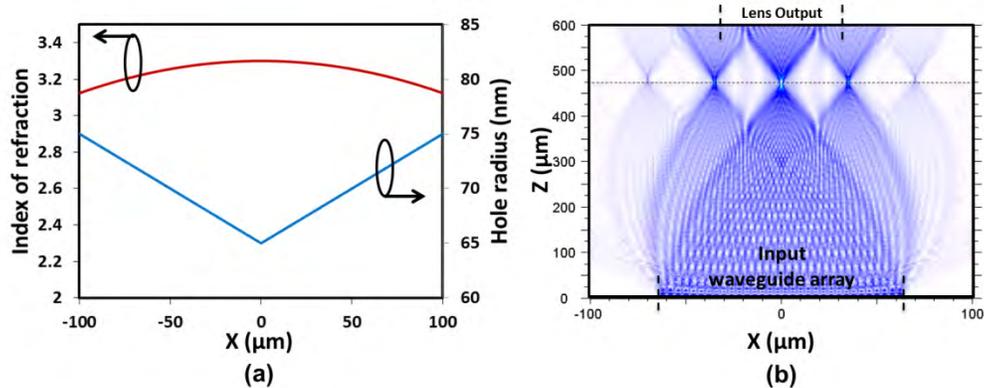
Fig. 5. (a) A cross-section of the calculated refractive index profile for the GRIN lens. The cross section is taken at 250 μm into the lens. (b) Simulated intensity passing through the lens with zero phase shift between channels. The focal length is marked at 473 μm.
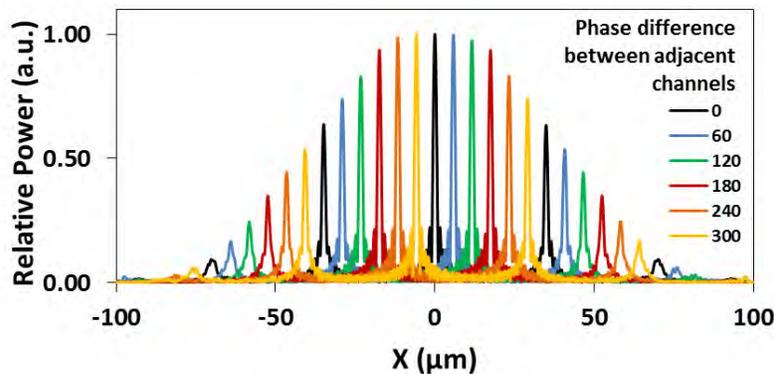
Fig. 6. Calculated lens output power for linear relative phase delays between adjacent channels in degrees.

4. Fabrication

The PIC was fabricated on 500 nm SOI with 1 μm buried oxide. Rib waveguides were patterned using 248 nm DUV lithography and etched 275 nm. *P-i-n* diodes for the phase modulators were made with boron and phosphorus implantation of and a 1050°C anneal. Emitter gratings were then formed over the waveguides by e-beam lithography and etching 50 nm. The gain regions were formed by bonding III-V epitaxial material to the top silicon as per the hybrid silicon process described in [14,15]. The III-V substrate was removed with a mechanical polish and wet-etch. The III-V was then patterned and dry-etched to create gain elements in the laser and amplifier sections but avoid losses in the silicon waveguides. Metal contacts were added through e-beam deposition for gain and phase modulator sections. A buffer layer of SiO_2 was deposited by PECVD. Vias were etched to the contacts and probe metal was deposited.

5. Packaging and test setup

The finished chip was diced and then thinned by mechanically polishing the backside down to 100 μm in order to reduce thermal impedance between the active devices and the heat sink. The backside was metalized for better thermal conduction and then bonded to a gold pad on a BeO carrier using a thin thermally conductive epoxy. The carrier was placed in a copper

mounting block that connected the carrier to a water cooled block with additional epoxy. The signal pads from the chip were wire-bonded to matching pads on the carrier. A pogo-pin adaptor connected the pads on the carrier to a printed circuit board where a series of wires linked the board to the driver and measurement devices. A total of 101 separate signals were required to fully use this chip. Pictures of the finished 6 mm x 11.5 mm chip can be seen in Fig. 7.
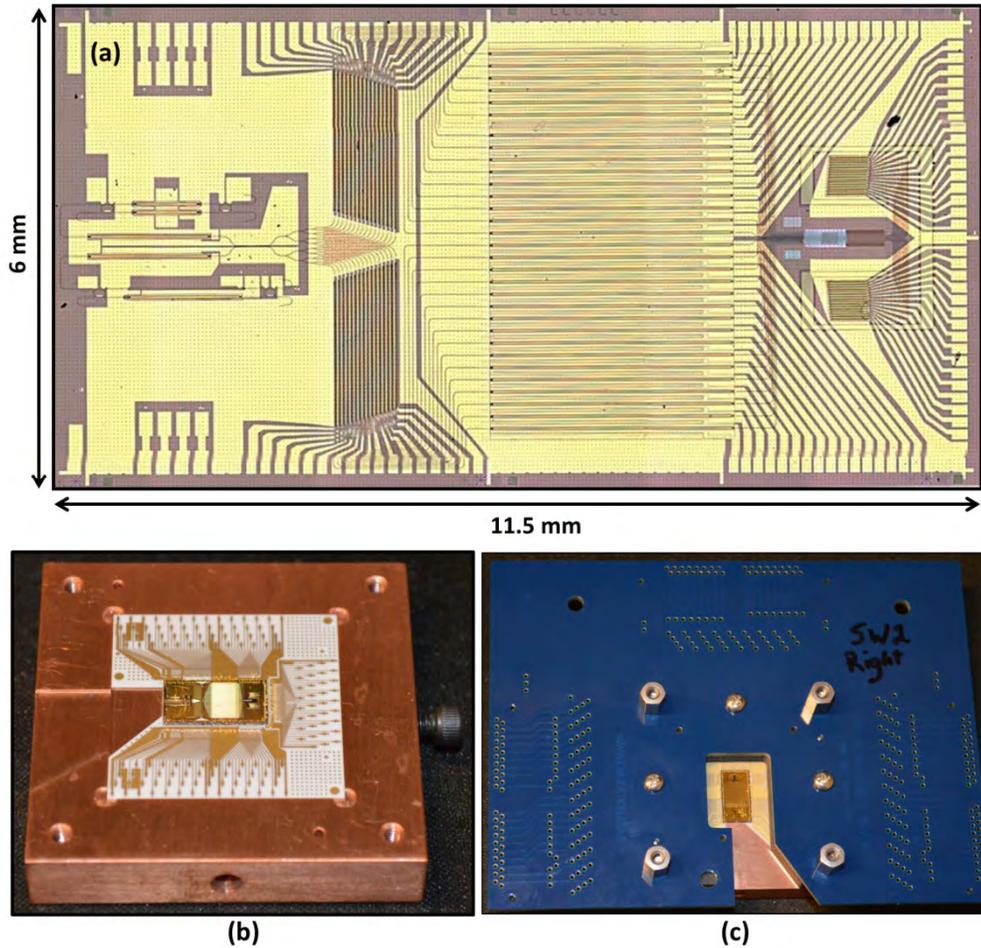
Fig. 7. (a) Confocal microscope picture of the fully integrated beam-steering PIC. The chip size is y x z cm2. (b) Photos of the mounted and wire-bonded chip placed in a water-cooled copper block and (c) the PCB attached to the assembly.

The optical output from the device was measured using two configurations. First, a lens to fiber was placed over the chip to measure the optical spectrum of the device for wavelength characterization. The second configuration is shown in Fig. 8 and used a total of three lenses: Lenses 1 and 3 were used to image the output from the device onto an IR camera and Lens 2, an aspheric lens with high numerical aperture, was used to image the far-field. Lens 2 was placed in a rotating mount to provide easy switching between far- and near-field imaging, as were several neutral density filters to avoid saturating the camera. A polarization controller was also used to align the polarization along the TE axis.
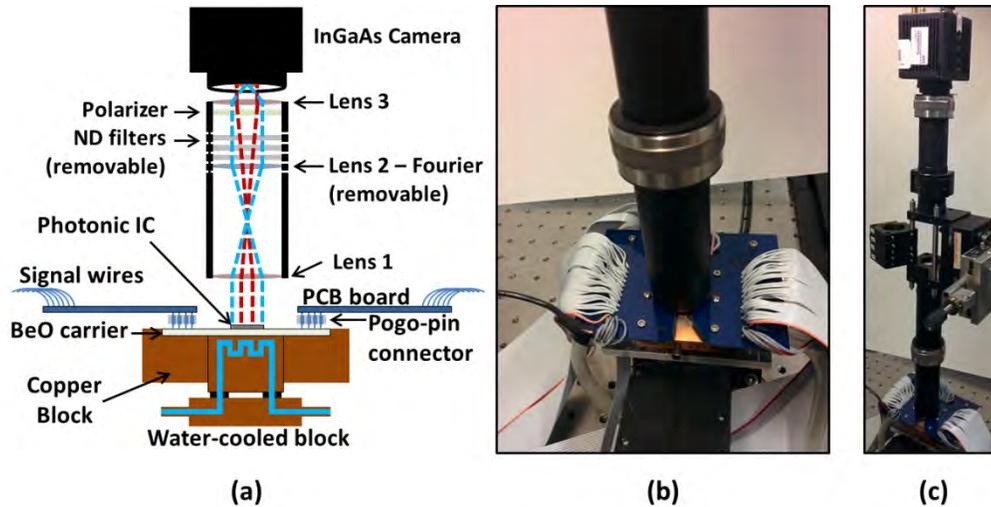
Fig. 8. (a) Schematic of the test setup and (b)-(c) images of the test setup.

6. Results

6.1 Lasers and amplifiers

SEM images of the laser and amplifiers are shown in Fig. 9. Wavelength measurements were performed with a fiber collimator placed over the chip that captured the light after being emitted from the PIC.

The single-gain-section laser performed significantly better than the dual-gain-section lasers (see Fig. 2) with respective threshold currents of 94 and 168mA. The SOAs also exhibited lasing at currents between 200 and 400 mA due to small reflections off of the tapers.

To characterize wavelength tuning the laser gain was pumped at 260 mA, the pre-amplifier was pumped at 180 mA, and the rest of the chip was un-pumped. Scattered light from the laser and pre-amplifier was collected using the fiber collimator for direct measurement. The laser exhibited tuning over 34.5 nm (Fig. 10). Additional testing with the lens setup showed good correlation of measured and expected angle tuning (based on wavelength measurements), thus verifying that the grating couplers are working as designed. Wavelength tuning efficiency of 0.28 nm/mW was achieved from the laser that gives a predicted angle tuning efficiency of 0.030 °/mW. The measured angle tuning efficiency was 0.034 °/mW. The beam was steered a total of 4.4° in θ with a tuning efficiency of 0.127°/nm as designed and predicted in Section 3.2.

The yield on working gain elements was 93% leaving 3 channels with un-pumped amplifiers.

9
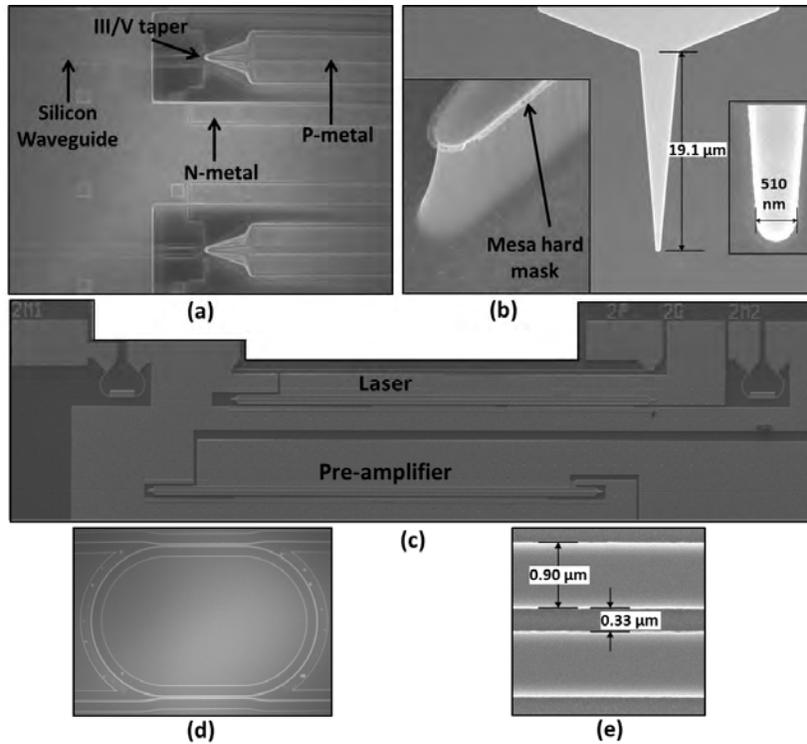
Fig. 9. SEMs of (a) laser and pre-amplifier gain elements, (b) InP tapers for adiabatic transitions between III/V gain and silicon waveguides with magnified images of the taper tip immediately following mesa etching, (c) completed laser and pre-amplifier, (d) ring mirror and (e) ring-to-bus coupler.
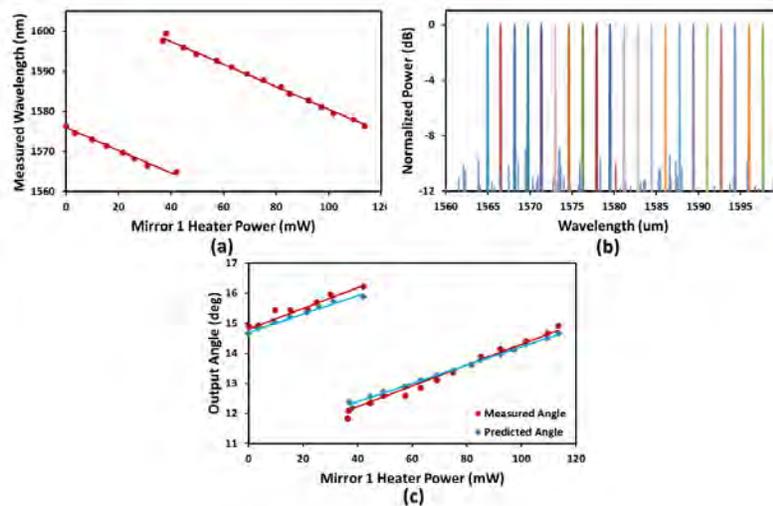
Fig. 10. (a) Measured peak wavelength vs. tuning power from one mirror, (b) measured optical spectra, and (c) measured output angle vs. predicted output angle (from wavelength measurement). A wavelength tuning efficiency of 0.28 nm/mW was achieved and the tuning efficiency of predicted and measured angle were 0.030 and 0.034 °/mW respectively. Since the laser was integrated on-chip it was unable to be measured individually so the full spectra SMSR is not available.

10

6.2 Phase modulators

The phase modulators were characterized using Mach-Zehnder test structures. Although designed to work electro-optically they worked almost entirely in the thermo-optic (TO) regime as evidenced by a clear dependence on power rather than a dependence on current (Fig. 11). When electro-optic (EO) tuning is present, phase tuning typically begins in a current-dependent regime that gives way to a power-dependent regime as thermal effects dominate. In silicon, TO and EO tuning shift the index of refraction in opposing directions (TO causes positive change with increasing injected electrical power while EO causes negative index change with increasing injected electrical current) so the crossover between the two is easily discerned. In the case of this chip the thermal tuning was almost immediately dominant and a tuning efficiency of 160 mW/π was measured.

The thermo-optic dominance is attributed to a high resistance in the silicon layer from process contamination. Test runs of the modulators without III/V bonding showed EO tuning with efficiencies of 14 mA/π (a low power regime where TO tuning is minimal) and a 3dB bandwidth greater than 50 MHz. It is believed that damage to the contacts, as well as possible damage to the trench region around the rib, is the cause of the discrepancy between the test devices and the phase modulators on the full PIC – i.e. increased resistance in the current path led to increased joule heating. A comparison of transmission line measurements (TLMs) between the two processing runs shows that the sheet resistance on the integrated phase modulators was greater than 7 times that of the devices processed without III/V. The integrated modulators exhibited a 3 dB bandwidth greater than 300 kHz.

The phase-modulator yield was 97% on the beam-steering PIC.
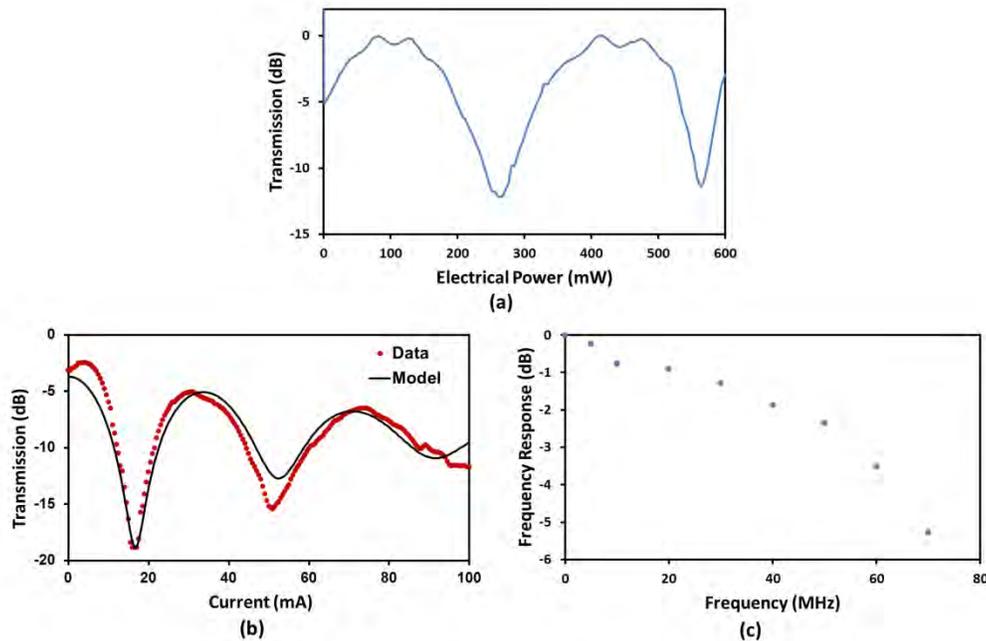
Fig. 11. (a) Transmission through a 2 mm Mach-Zehnder test structure showing a phase modulator dependency on power implying a thermo-optically dominated device on the integrated chip. Test run measurements of similar devices showing (b) 14 mA/π tuning efficiency with data and modeled fit and (c) a 3dB bandwidth greater than 50 MHz.

6.3 Lens and photodiode array

SEM images of the lens and output gratings are shown in Fig. 13, and a larger image of the lens and photodiode array is shown in Fig. 14. Unfortunately, errors in the proximity correction of the e-beam lithography meant that attempts to characterize the beam angle using the lens and photodiode array were unsuccessful as the photo-current produced in each photodiode was not well correlated with the angle.

Characterization of the lens and photodiode array was done by pumping one of the central channel amplifiers at high enough current to induce lasing from taper reflections and then measuring the reverse photocurrent in the photodiode array. Test photodiodes were also measured with an external laser to determine the responsivity and quantum efficiency (Fig. 12). For the wavelengths available in the PIC, the quantum efficiency averaged 45% and the responsivity averaged 0.57 A/W for 470 μm long photodiodes. 100% yield on the photodiodes was achieved.
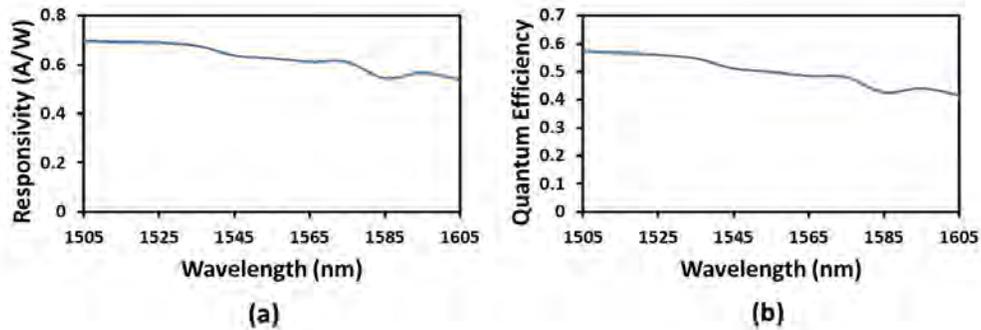
Fig. 12. (a) Responsivity and (b) quantum efficiency of the 470 μm long photodiodes at −5 V.
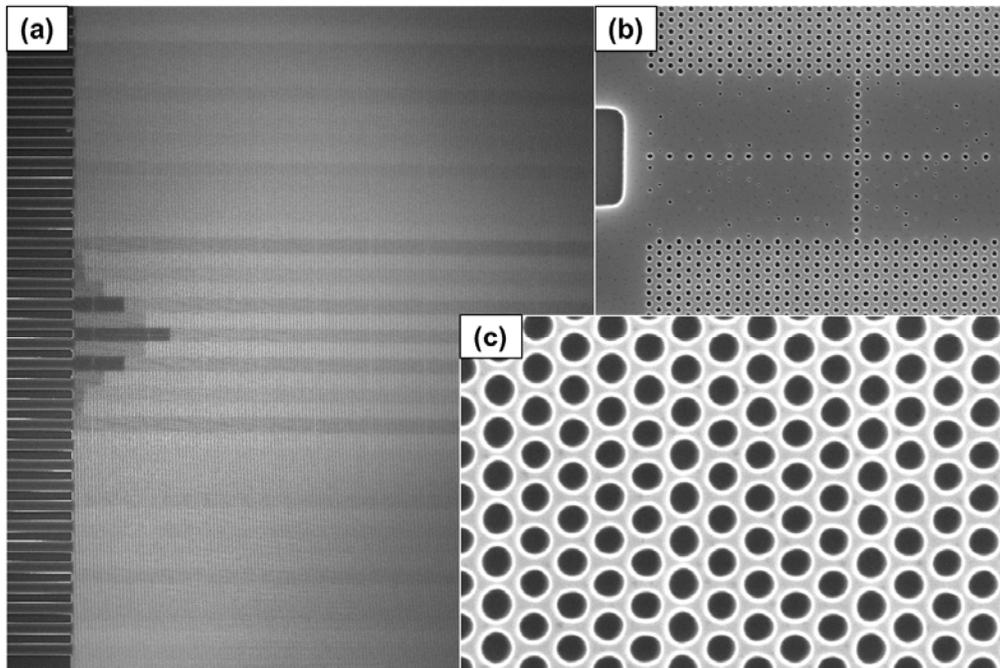
Fig. 13. SEMs of (a) input waveguides and the beginning of the GRIN lens, (b) a zoomed in SEM of insufficiently etched holes that led to lens distortion of the beam, and (c) a close-up image of the photonic crystal lens etched spots.

12
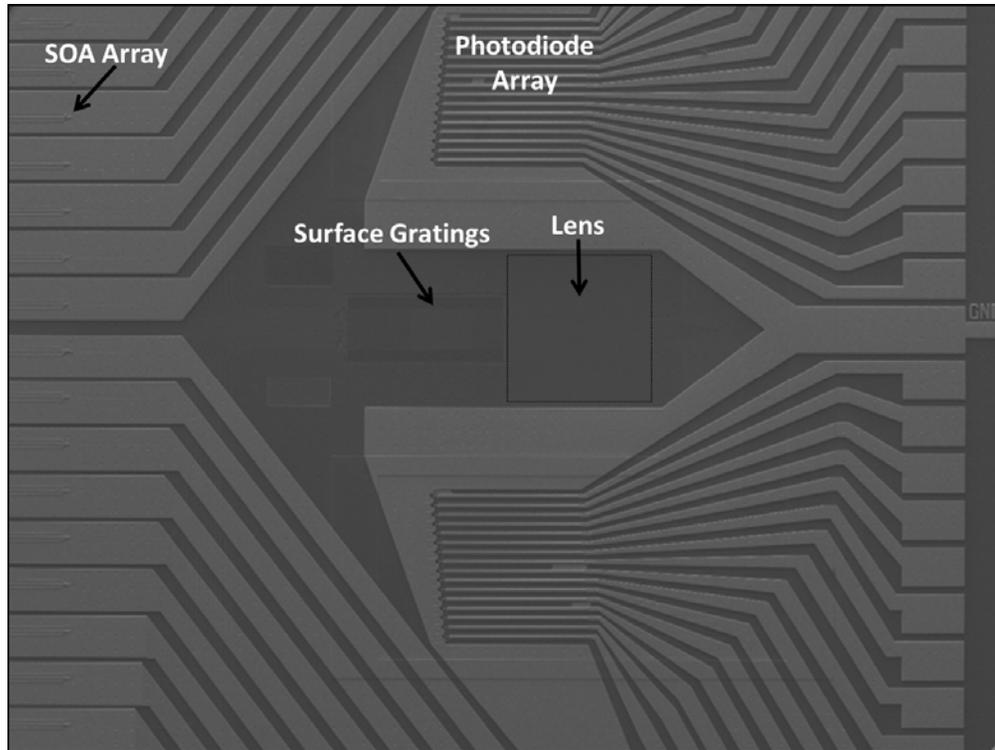
Fig. 14. SEM of output grating array, lens and photodiode array.

6.4 Integrated 32 channel device

For two-dimensional beam-steering the laser gain current was set to 260 mA and the pre-amplifier gain current was set to 240 mA. After tuning the laser's mirror and phase heaters to select the desired wavelength, the phase modulator and channel amplifier currents were optimized by use of a hill-climbing algorithm as described in [5]. The beam optimization is measured as the power at the desired angle divided by the maximum power of the side lobes within a window of angles. For a given phase modulator channel the beam optimization is measured for several current shifts around the last value where the shift is a multiple (−2, −1, 0, 1, 2) of some delta. The delta is chosen by taking a fit of the beam optimization at each current, calculating a slope, and shifting the current for that channel in the direction of improved beam optimization. More intricate algorithms were attempted, but it was found that the simple hill-climbing algorithm was best able to optimize the beam. Beam-steering of 23° (ψ) x 3.6° (θ) was achieved (Fig. 15) with respective beam widths of 1° x 0.6° and greater than 70% background suppression. This corresponds to 23 x 6 (a total of 138) resolvable spots. The side lobe suppression was limited to 70% by a combination of inconsistent gain characteristics across the amplifier array, multimode output from some channels, and 3 failed channel amplifiers.

13
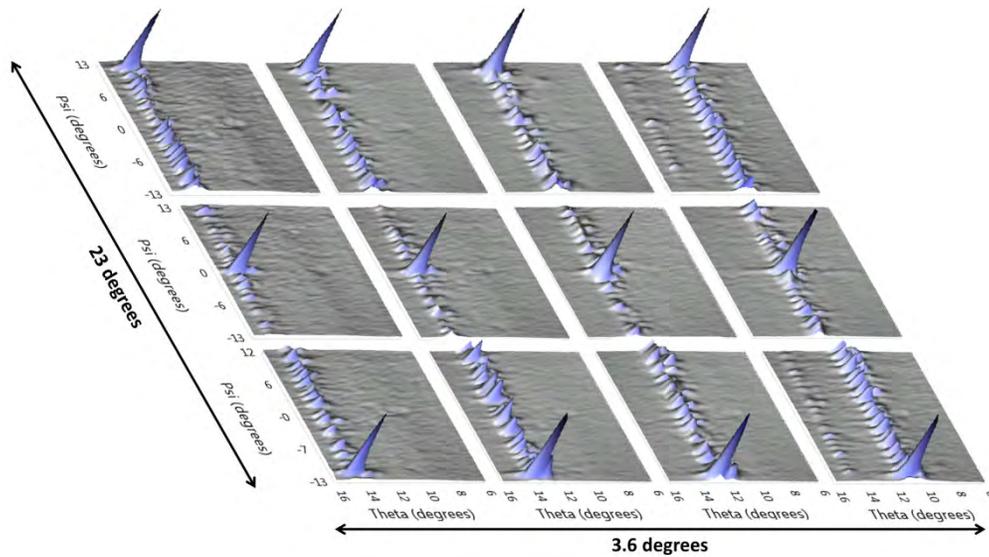
Fig. 15. Two-dimensional beam-steering plots spanning 23° in ψ and 3.6° in θ.

7. Conclusion

We have presented the first fully-integrated free-space beam-steering chip on the hybrid-silicon platform. The PIC incorporates a total of 164 components with 9 different component types. Steering over 23° x 3.6° was exhibited with beam widths of 1° x 0.6° giving a total of 138 resolvable spots in the far field with 5.5 dB background suppression.

Acknowledgments

14

I. Photonic Integrated Circuits

B. Optical Phase-Locked Loops

Highly Integrated Homodyne Receiver for Short-reach Coherent Communication

Mingzhi Lu[1*], Hyun-Chul Park[1], Eli Bloch[2], Leif A. Johansson[1], Mark J. Rodwell[1], and Larry A. Coldren[1,3]

[1]*Department of Electrical and Computer Engineering, University of California, Santa Barbara, CA, 93106, USA.*
(*M. Lu currently with Infinera Corp., Sunnyvale, CA 94089, USA)
[2]*Department of Electrical Engineering, Technion – Israel Institute of Technology, Haifa 32000, Israel.*
[3]*Department of Materials, University of California, Santa Barbara, CA, 93106, USA.*
lumz85@gmail.com

(Invited)

Abstract: A highly integrated homodyne receiver has been demonstrated within a footprint of 1 cm^2. The receiver successfully receives 40 Gbit/s BPSK and error free is achieved up to 35 Gbit/s. Theoretical analysis has been also carried out showing the feasibility of integrated 16 QAM homodyne coherent receivers.
OCIS codes: (250.5300) Photonic integrated circuits; (060.2840) Heterodyne; Optical phase-locked loop; optical frequency synthesis

1. Introduction

Recently, a resurgence of effort is being devoted to the research of coherent optic fiber communications, because its advantages of higher sensitivity, better noise tolerance, and more importantly, its compatibility with complex modulation format, such as QPSK, 16 QAM. Based on advanced digital signal processor (DSP) technology, DP QPSK coherent links have been deployed widely, and 16 QAM links also start to be applied to metro or even long haul applications. Modern DSP-based intradyne receivers solve most of the problems in coherent communication systems, but it also gives rise to a very high power consumption (roughly 1 W/Gbps or higher) and high cost, both of which limit its application within long-haul or long-distance metro links. In order to solve the high-cost and high power consumption problems that intradyne receiver inherently have, optical phase-locked loop (OPLL) based homodyne receivers become an alternative [1].

Although research in 1980s and 1990s indicates the difficulties of the implementation of OPLL-based homodyne receiver, especially its stringent limit on linewidth and physical loop delay [3], photonic and electronic integration technology have solved this problem to a great extent [1,2]. By integrating all the optical components on the same chip and combing with the ASIC, the system size decreases dramatically and the physical loop delay reach the order of sub-ns [1,2,4]. Therefore the stringent limit on laser linewidth. It not only makes homodyne receiver practically feasible, but also make it excel intradyne receiver in many aspects, including power consumption, size, and baud rate.

2. Experimental demonstrations

In this work, a highly integrated Costas loop is proposed and demonstrated. By photonic and electronic integration, the whole receiver is realized within a footprint of 10 mm × 10 mm area, and 120 ps loop delay is achieved. The architecture of the Costas loop is shown in Fig. 1. The receiver consists of three main parts: a photonic integrated circuit (PIC), and an electronic integrated circuit (EIC) and a hybrid loop filter (Fig. 1) [1].

The incoming signal and the LO are mixed in the optical 90 degree hybrid, and I/Q signals are then generated on four photodetectors. The I/Q signals are then mixed at the XOR gate on the EIC, and therefore the data-OPLL cross-talk is eliminated by the phase doubling. The XOR gate together with the delay line works as a quadric-correlator frequency detector, and the XOR itself also acts as a phase detector. The phase/frequency error signals are then fed back to the laser phase tuning section through the loop filter, as shown in Fig. 1.
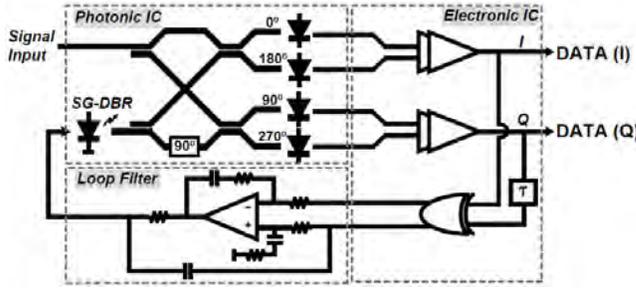
Fig. 1. Homodyne receiver architecture.
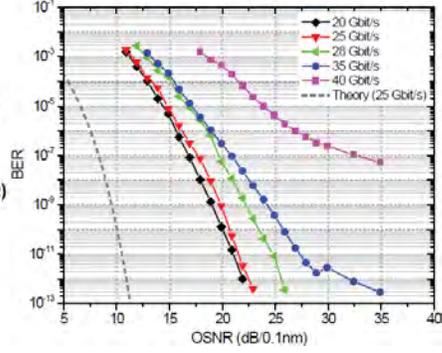
Fig. 2. Measured BER of the homodyne receiver.

On the PIC, a widely tunable sampled-grating DBR (SG-DBR) laser, a directional-coupler-based 90 degree hybrid, four uni-travelling-carrier (UTC) photodetectors and microstrip transmission lines are integrated monolithically [5].

The PIC, EIC, and loop filter are connected together using wirebonds. A BPSK transmitter is built using commercial components for the testing purpose. 2^{31}-1 PRBS data is applied to the transmitting laser using the NRZ BPSK format. A VOA and an EDFA are used to control the OSNR of the received signal. The BPSK signal is coupled into the PIC through a lensed fiber, and the power of the SG-DBR laser is coupled out through another lensed fiber, and beat with the transmitting laser on a high-speed photodetector for the monitoring purpose. Bit error rates (BERs) are also measured [1].

We successfully locked the optical phase of the SG-DBR laser to the phase of the transmitting laser. The beating spectrum measured by the ESA showed 1.1 GHz closed-loop bandwidth. BER is also measured with various OSNR of the input signal. Error free (BER < 10^{-12}) is achieved with a data rate up to 35 Gbit/s. Both measured BER and the theoretical BER are plotted in Fig. 4. The power consumption of the system is around 3 Watt, not including the TEC cooling. [1]

3. Theoretical analysis for 16 QAM receiver [6]
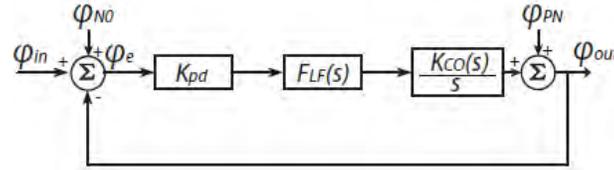
Fig. 3. Noise analysis model for PLL.

In the previous experiment, the LO laser linewidth has a seemingly large spectral linewidth of >10 MHz. However, no linewidth-related performance degradation is observed. It is because that the noise suppression bandwidth the homodyne receiver, the closed loop bandwidth, is large enough to suppress most of the phase noise from the local oscillator [1,3].

An OPLL model is shown in Fig. 3, where noise are introduced from two locations, ϕ_{N_0} from the input of the phase detector, and ϕ_{PN} from the output of the CCO. The summed effects of ASE noise, shot noise, the thermal noise and RIN are represented by ϕ_{N_0}, and the laser phase noise is ϕ_{PN}. The system performance can be expressed in the following equation.

$$\left(\phi_{N_0} + \phi_{in} - \phi_{out}\right) \cdot K_{pd} \cdot F_{LF}(s) \cdot \frac{K_{CO}(s)}{s} + \phi_{PN} = \phi_{out},$$

where $K_{pd} \cdot F_{LF}(s) \cdot \frac{K_{CO}(s)}{s}$ indicates the open loop response of the homodyne receiver. Within the loop bandwidth, the LO phase noise is suppressed by the closed-loop response function, while on the other hand ASE noise, thermal noise, laser RIN and shot noise are passed through within the loop bandwidth. As for laser phase noise modeling, both ASE noise and 1/f carrier-injection noise are considered. Parameters used in this calculation are listed in Table 1.

16

Using the parameters listed in Table 1, the phase noise spectrum of the OPLL can be obtained and therefore the laser residue phase error variance can be obtained. Based on the residue phase noise and the other white noises, the Q-factor of receiver can be obtained. The detailed derivation can be found in [6]. By utilizing this receiver as a 16 QAM receiver, the BER is calculated (Fig. 4). As we can see, with a 1 GHz loop natural bandwidth, the receiver can work in an error-free (BER<1e-12) condition with no digital signal processing. When the loop bandwidth is 2-3 GHz, the receiver performance is optimized. When the assumed loop bandwidth reaches 10 GHz, the low SNR performance is degraded due to the high ASE noise level. It is worth mentioning that the calculation is based on the summed laser linewidth of 3 MHz, which is higher than most of the published 16 QAM receiver work.

Parameter	Value
Summed laser linewidth ($\Delta\nu$)	3 MHz
Reference laser power on each photodetector (P_{sig})	1.25 mW
LO laser power on each photodetector (P_{LO})	1.25 mW
Photodetector responsitivity ($\Re$)	0.8 A/W
Photodetector load resistor (R)	50 Ω
Photodetector bandwidth (Δf)	25 GHz
Data symbol rate ($R_s = \Delta f$)	25 Gbaud/s
Imperfect power balance of the balanced photodetector (η)	95 %
LO laser RIN (RIN)	-140 dBc/Hz
OPLL loop type and order	Second order type II
OPLL damping factor (ζ)	0.7
TIA noise figure (F)	20 dB
Reference bandwidth for OSNR (B_{ref})	0.1 nm

Table 1. Parameters used in calculation.
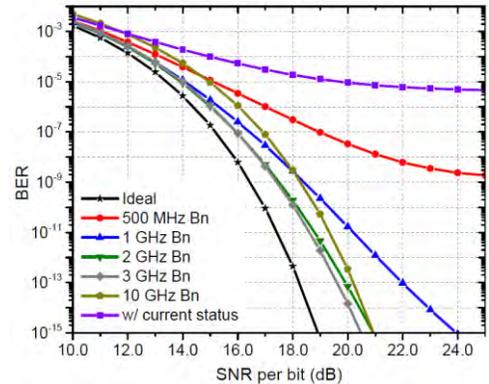
Fig. 4. Calculated BER of the 16 QAM receiver with various loop bandwidths.

4. Conclusion

A 40GB/s OPLL-based homodyne receiver has been demonstrated with very low power consumption and good overall performance. Utilizing the same OPLL model, the feasibility of a 16 QAM receiver is theoretically proved, and with a 1 GHz loop bandwidth error-free reception can be achieved with a 3 MHz linewidth laser as local oscillator. It provides a good solution for relatively short distance, cost effective, efficient coherent communication.

Acknowledgement

Reference:

[1] M. Lu, H. Park, E. Bloch, A. Sivananthan, J. S. Parker, Z. Griffith, L. A. Johansson, M., J. W. Rodwell, and L. A. Coldren, "An Integrated 40 Gbit/s Optical Costas Receiver," Journal of Lightwave Technology, Vol. 31, Iss. 13, pp. 2244–2253 (2013).

[2] M. Lu, H. Park, E. Bloch, A. Sivananthan, A. Bhardwaj, Z. Griffith, L. A. Johansson, M.J. Rodwell, and L.A. Coldren, "Highly integrated optical heterodyne phase-locked loop with phase/frequency detection," Opt. Express 20, 9736-9741 (2012).

[3] L. Kazovsky, "Decision-driven phase-locked loop for optical homodyne receivers: Performance analysis and laser linewidth requirements," Lightwave Technology, Journal of, vol. 3, no. 6, pp. 1238-1247 (1985).

[4] S. Ristic, A. Bhardwaj, M. Rodwell, L. Coldren, and L. Johansson, "An optical phase-locked loop photonic integrated circuit," Lightwave Technology, Journal of, vol. 28, no. 4, pp. 526-538 (2010).

[5] M. Lu, H. Park, E. Bloch, A. Sivananthan, J. S. Parker, L. A. Johansson, M. J. W. Rodwell, and L. A. Coldren, "Monolithic Integration of a High-speed Widely-tunable Optical Coherent Receiver," Photonics Technology Letters, Vol. 25, No. 11 (2013).

[6] M. Lu, "Integrated Optical Phase-locked Loops", Ph.D. dissertatioin, University of California, Santa Barbara (2013).

I. Photonic Integrated Circuits

C. Optical Phase-Sensitive-Amplifiers

First Demonstration of an Integrated Photonic Phase-Sensitive Amplifier

Wangzhe Li, Mingzhi Lu, Leif Johansson, Milan Mashanovitch, Danilo Dadic, Shamsul Arafin and Larry A. Coldren

Department of Electrical and Computer Engineering, University of California, Santa Barbara, California 93117, USA

coldren@ece.ucsb.edu

Abstract: For the first time, an integrated photonic phase-sensitive amplifier is reported. Approximately 6.3 dB extinction of on-chip phase-sensitive gain based on a signal-degenerate dual pump four-wave mixing architecture has been achieved.

OCIS codes: (190.4380) Nonlinear optics, four-wave mixing; (190.4410) Nonlinear optics, parametric processes; (250.5300) Photonic integrated circuits; (250.5980) Semiconductor optical amplifiers

1. Introduction

Optical phase-sensitive amplifiers (PSAs) have been attracting increasing research attention in the past few years [1] due to its well-known advantage of realizing noiseless amplification and potential 0 dB noise figure (NF). Compared to conventional phase-insensitive amplifiers (PIAs) featuring 3-dB quantum-limited NF, PSAs' noise-free amplification could significantly improve the performance of the optical amplifier and provide a wide range of applications, such as optical telecommunication, optical sensing, optical spectroscopy, and LIDAR. Although PSAs have been demonstrated using parametric down-conversion in $\chi^{(2)}$-based nonlinear material [2], and using four-wave mixing (FWM) in $\chi^{(3)}$-based nonlinear media like optical fibers [3] and semiconductor optical amplifiers (SOAs) [4], in all demonstrated PSAs so far, their implementations are based on bulky bench-top systems, which makes it difficult to use them in real-world scenarios. Photonic integration that enables the combination of key optical components and reduction in scale would great benefit the implementation of PSAs for practical applications.

In this paper, for the first time, we report an integrated photonic signal-degenerate dual pump PSA based on a highly nonlinear SOA (NL-SOA) and demonstrate its 6.3 dB extinction of on-chip phase-sensitive gain. To the best of our knowledge, it is also the first time to use an SOA for non-degenerate phase-sensitive amplification.

2. Principle

Figure 1 and Figure 2 show respectively the schematic and the photo of the signal-degenerate dual pump PSA. The coherent input light waves, which are coupled into the chip, consist of two pumps and one signal to be amplified, and are here generated based on external modulation. The modulator can also be integrated on the photonic IC.
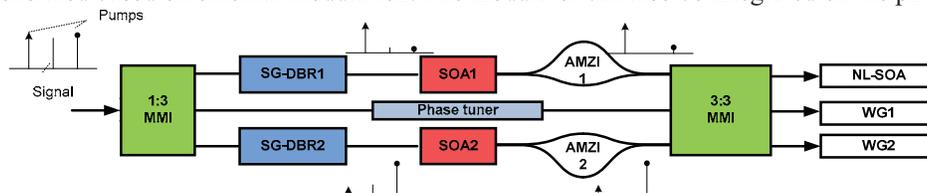
Fig.1 Schematic of the signal-degenerate dual-pump PSA
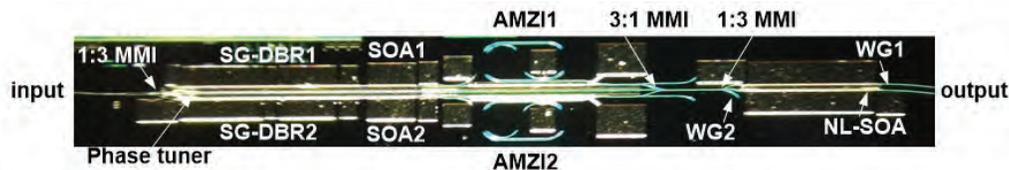
Fig. 2 Photo of the fabricated photonic integrated circuit of the proposed PSA

To achieve low NF, wavelength selective switches should be used to split and combine signal and pumps. However, to reduce the complexity of the chip in this first demonstration, the input light waves are here split into three paths via a 1 by 3 multimode interference (MMI) coupler. Among two of three paths, there are two sampled grating distributed Bragg reflector (SG-DBR) lasers, each of which is injection locked by the corresponding pump that is then selectively amplified. After further amplified by the followed SOA, the pump is filtered by an asymmetric Mach-Zehnder interferometer (AMZI) to remove the residual signal and the noise falling in the signal's

spectrum, which avoids signal interference among three paths and enables the signal to be shot-noise limited. Along the third path, there is a phase tuner to phase shift the signal based on quantum-confined stark effect, therefore, the adjustable and stable phase relationship among the signal and two pumps can be achieved for observing the variation in signal power after phase sensitive amplification as a function of signal's phase. The light waves along three paths are combined together and split again by a 3-by-3 MMI coupler to a NL-SOA where phase-sensitive amplification occurs, a long passive waveguides (WG) as potential alternative and a short WG as a reference. The SOA is particularly used as a PIA and its PIA gain caused by population inversion maybe interfere with the nonlinear parametric process and undermine the phase-sensitive amplification. To overcome or minimize this issue, the NL-SOA would be saturated to optimize the FWM and suppress the amplified spontaneous emission noise.

To monolithically integrate the single-chip PSA, we have chosen an InP/InGaAsP centered quantum well (CQW) platform with 10 quantum wells. Quantum well intermixing (QWI) technology [5] is used to define active and passive areas. CQW platform maximizes the mode overlap with the QWs, and therefore more significant nonlinear effect has been achieved. Moreover, the passive waveguide with intermixed quantum wells still have quite strong quantum stark effect, which is ideal for low-loss phase tuner. On the chip, both surface ridge waveguide and the deeply etched ridge waveguides are defined. Surface ridge is used for the SG-DBR laser for better heat dissipation and single-mode operation. Deeply etch waveguide is used for rest of the chips, which leads to better flexibility for waveguide routing and better SOA nonlinear efficiency due to higher confinement factor.

3. Experimental results

Coherent incident light waves are generated via external modulation with a RF frequency of about 10 GHz, which is half of the free spectral range of the AMZIs. Each SG-DBR laser is configured properly to be injection locked by the corresponding pump. The output power of each SG-DBR is about 12 dBm, and each AMZI is configured to maximize the pumps and suppress the signal along the path. The current applied to the phase tuner is tuned from 0 to 4 mA and the relative phase of the signal is measured as shown in Figure 3. The total power of the pump and signal waves sent to the NL-SOA is about 0 dBm, which is enough to enable the NL-SOA saturated. Given that the injection locking is enabled or not, the signal power at the output of the NL-SOA is measured as the current applied to the phase tuner is swept from 0 to 4 mA, which is shown and compared in Figure 3 as well.
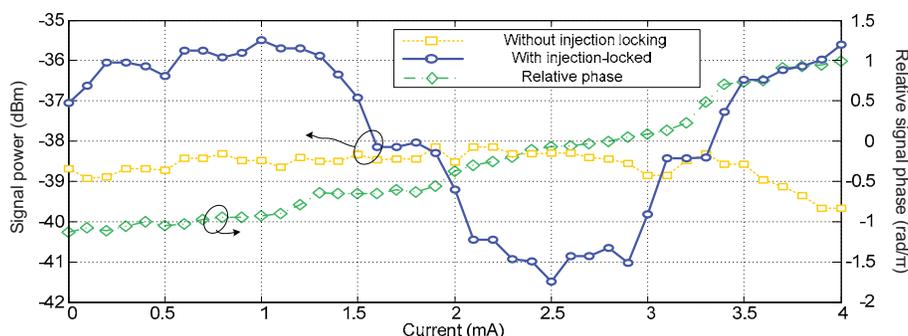
Fig. 3 Measured signal power at the output of the NL-SOA with and without injection locking, and measured relative phase change of the signal as the current applied to the phase tuner is increasing from 0 to 4 mA.

As can be seen in Figure 3, when two SG-DBR lasers run independently, there is no phase-sensitive amplification due to random phase drifting among the pump and signal waves. The measured average signal power is about -38.5 dBm with approximate ±0.4 dB fluctuation when the current is lower than 3.5 mA. Once the injection locking is enabled, the pump and signal waves become as coherent as the incident light waves and phase sensitive amplification is realized, the signal power goes up to -35.3 dBm and decreases to -41.6 dBm, exhibiting a sine-curve like change as the signal phase is swept over 2π. Approximately 6.3 dB extinction of phase-sensitive on-chip gain is demonstrated. This is to the best of our knowledge the demonstration of a fully integrated photonic PSA.

4. References

[1] J. Hansryd, P. A. Andrekson, M. Westlund, J. Li, and P.-O. Hedekvist, "Fiber-based optical parametric amplifiers and their applications," IEEE Select. Topics Quantum Electron. **8**, 506–520 (2002).
[2] K. J. Lee, F. Parmigiani, S. Liu, J. Kakande, P. Petropoulos, K. Gallo, and D. J. Richardson, "Phase sensitive amplification based on quadratic cascading in a periodically poled lithium niobate waveguide," Opt. Express **17**, 20393–20400 (2009).
[3] Z. Tong, C. Lundström, P. A. Andrekson, C. J. McKinstrie, M. Karlsson, D. J. Blessing, E. Tipsuwannakul, B. J. Puttnam, H. Toda, and L. Grüner-Nielsen, "Towards ultrasensitive optical links enabled by low-noise phase-sensitive amplifiers," Nat. Photonics **5**, 430–436 (2011)
[4] A. D. Ellis and S. Sygletos, "Phase sensitive signal processing using semiconductor optical amplifiers," in OFC2013, paper OW4C.1
[5] E. Skogen, J. Barton, S. Denbaars, and L. Coldren, "A quantum-well-intermixing process for wavelength-agile photonic integrated circuits," IEEE J. Sel. Top. Quantum Electron. **8**, 863–869 (2002).

Single-chip dual-pumped SOA-based phase-sensitive amplifier at 1550nm

L. A. Coldren[1*], W. Li[1], A. Mecozzi[2], M. Lu[1], S. Arafin[1], M. Vasilyev[3], D. Dadic[1], and L. Johansson[1]

[1]Dept. of Electrical and Computer Engineering, University of California, Santa Barbara, California, USA
[2]Dept. of Physical and Chemical Sciences, University of L'Aquila via Vetoio 1, L'Aquila, Italy
[3]Dept. of Electrical Engineering, University of Texas at Arlington, Texas, USA
[*]coldren@ece.ucsb.edu

Invited Paper

Abstract—A saturated semiconductor-optical-amplifier exhibited 6.3 dB of phase-sensitive gain using two tunable laser pumps coherently injection-locked from sidebands of a modulated tone, all integrated on a single InP chip.

Keywords—phase sensitive amplifier, semiconductor optical amplifier, photonic integrated circuit, four wave mixing

I. INTRODUCTION

All optical signal processing based on noiseless phase-sensitive amplification (PSA) has been attracting increasing attention in recent years [1] and has been demonstrated in various bench-top systems using either parametric down-conversion in $\chi^{(2)}$-based nonlinear materials [2], or four-wave mixing (FWM), in $\chi^{(3)}$-based nonlinear mediums such as optical fibers [3] and semiconductor optical amplifiers (SOAs) [4]. However, it is difficult to use these bulky setups in practical scenarios. Photonic integration that enables the combination of key optical components and reduction in scale would greatly benefit the implementation of PSAs for practical applications.

In this paper, an integrated photonic signal-degenerate dual-pumped PSA at 1550 nm, based on a saturated SOA, is demonstrated. The performance of the SOA is characterized. Chip-scale PSA gain is theoretically analyzed, and a 6.3 dB extinction ratio of gain is realized.

II. CHIP-SCALE PSA

To monolithically integrate the single-chip dual-pumped PSA, an InP/InGaAsP centered quantum well (CQW) platform with 10 quantum wells (QWs), which can maximize the mode overlap with the QWs in an SOA and enhance the nonlinearity, is used. Quantum well intermixing (QWI) technology [5] is employed to define active and passive areas. Fig. 1 shows a schematic and a photo of the chip. Two pump sidebands and one signal generated from an external modulated tone are coupled into the chip and split into three paths via a 1-by-3 multimode interference (MMI) coupler. Along upper and lower paths, there are two sampled-grating distributed-Bragg-reflector (SG-DBR) lasers. Each laser is injection locked by one sideband, suppressing the other wavelengths. Each pump is amplified by an SOA, and noise is suppressed by an asymmetric Mach-Zehnder interferometer (AMZI). Along the

middle path, there is a phase tuner to phase-shift the signal based on quantum-confined stark effect; therefore, an adjustable and stable phase relationship among the signal and the two pumps can be achieved for observing the phase-dependent gain of the signal. The light waves along the three paths are combined together in a 3-by-3 MMI coupler and split to a nonlinear SOA (NL-SOA) where PSA occurs, as well as long and short passive waveguides (WG) as references. The NL-SOA is saturated to optimize the FWM and suppress the amplified spontaneous emission noise.
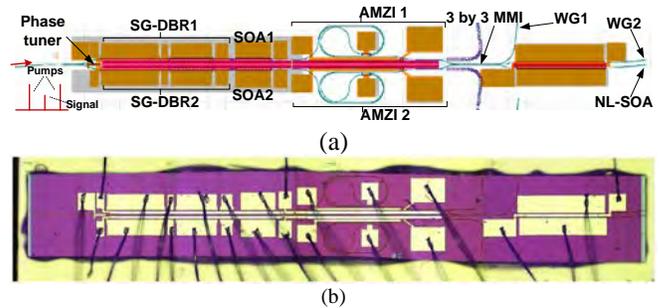
Fig. 1. Schematic and photo of the signal-degenerate dual-pumped PSA.

III. SOA CHARACTERIZATION

To theoretically investigate the chip-scale PSA in a NL-SOA, some identical SOAs with different lengths were made on the same wafer for characterization. Some of results are shown here. First of all, the gain profile of a 1-mm SOA, consisting of three cascaded 330-µm SOAs, was measured, which is shown in Fig. 2. The measured transparent current density is about 1 kA/cm^2. The peak gain is 47.5 dB/mm at 1560 nm when current density is about 9 kA/cm^2.
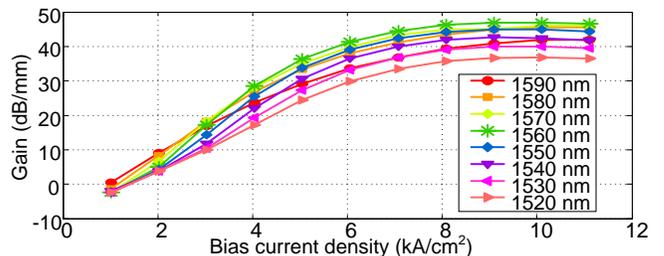
Fig. 2. Measured gain profile of a 1-mm SOA.

The dispersion was measured as well using a 2.3-mm SOA based on a setup shown in Fig. 3. An intensity-modulated light wave is sent to the SOA. The RF signal is from a vector network analyzer (VNA). Due to the dispersion of the SOA, nonlinear phase shifts would be applied to incident tones and the recovered RF signal at the PD. From the recorded phase change obtained from the VNA when sweeping the wavelength of the carrier, we can calculate the total dispersion of the SOA as shown in Fig. 4. As we can see, dispersion is about 0 from 1550 nm to 1570 nm, and reaches -700 fs/nm near 1530 nm.
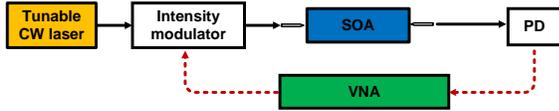
Fig. 3.   Setup of the SOA dispersion measurement.
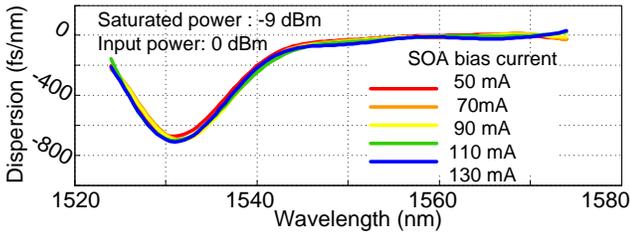
Fig. 4.   Measured dispersion of a 2.3-mm SOA.

The SOA carrier lifetime was measured using a 50-μm SOA, which is shown in Fig. 5. The carrier lifetime decreases quickly as the input power goes up, and reaches about 180 ps at a high input power of 20 mW.
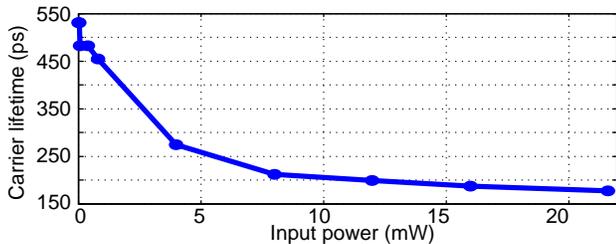
Fig. 5.   Measured carrier lifetime with respect to input light wave power.

IV. THEORETICAL SIMULATION AND EXPERIMENTAL RESULT

The injection current to the NL-SOA is set to be about 90 mA. The total power of the pump and the signal waves sent to the NL-SOA is set to be 0 dBm, saturating the NL-SOA. Using the parameters obtained from SOA characterization, a theoretical simulation of the PSA gain based on coupled differential equations [6] is presented in Fig. 6, showing a 6.5 dB extinction ratio of the phase-sensitive gain.

An experiment was performed to evaluate our simulation. Since the signal power after PSA varies with the signal phase, which should vary linearly with the square root of the injected current, the measured signal power at the output of the SOA with respect to the square root of the injected current was measured, which is shown in Fig. 7. For comparison, the signal power without injection locking and the relative phase change of the signal were measured, which are shown in Fig. 7 as well. The relative phase change was measured in a man-

ner similar to that shown in Fig. 3. When two lasers are in free-running modes, there is no PSA due to random phase drifting. Once the injection locking is enabled, however, there is no obvious PSA or phase change of the signal until after the current is larger than 1 mA. Such a delay in phase shift has been observed in tunable lasers and could be caused by an N^+ sheet charge that occurs at the regrowth interface due to surface contamination. As the current is increased from 1 mA to 4 mA, there is a π phase shift to the signal and one cycle of signal power change is observed. Approximately 6.3 dB extinction of phase-sensitive on-chip gain is achieved, which agrees well with the simulation over this current and phase-shift range.
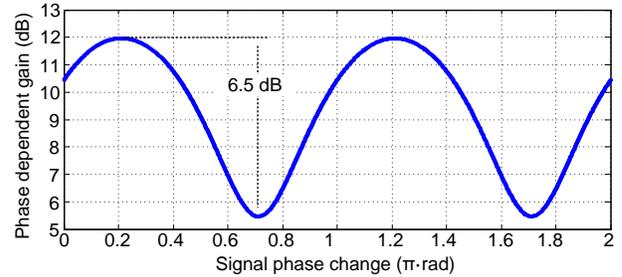
Fig. 6.   Simulation result of the phase-sesitive gain of the chip-scale PSA.
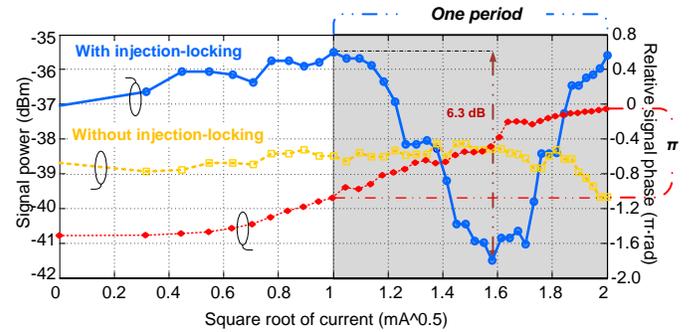
Fig. 7.   Measured relationship among the signal power, the signal phase and the square root of the current applied to the phase tunner.

REFERENCES

[1] J. Hansryd, P. A. Andrekson, M. Westlund, J. Li, and P.-O. Hedekvist, "Fiber-based optical parametric amplifiers and their applications," IEEE Select. Topics Quantum Electron. vol. 8, pp. 506–520, May/Jun. 2002.

[2] K. J. Lee, F. Parmigiani, S. Liu, J. Kakande, P. Petropoulos, K. Gallo, and D. J. Richardson, "Phase sensitive amplification based on quadratic cascading in a periodically poled lithium niobate waveguide," Opt. Express, vol. 17, pp. 20393–20400, Oct. 2009.

[3] Z. Tong, C. Lundström, P. A. Andrekson, C. J. McKinstrie, M. Karlsson, D. J. Blessing, E. Tipsuwannakul, B. J. Puttnam, H. Toda, and L. Grüner-Nielsen, "Towards ultrasensitive optical links enabled by low-noise phase-sensitive amplifiers," Nat. Photonics, vol. 5, pp. 430–436, Jun. 2011.

[4] A. D. Ellis and S. Sygletos, "Phase sensitive signal processing using semiconductor optical amplifiers," in OFC2013, paper OW4C.1

[5] E. Skogen, J. Barton, S. Denbaars, and L. Coldren, "A quantum-well-intermixing process for wavelength-agile photonic integrated circuits," IEEE J. Sel. Top. Quantum Electron. vol. 8, pp. 863–869, Jul. /Aug. 2002.

[6] J. Mørk and A. Mecozzi, "Theory of the ultrafast optical response of active semiconductor waveguides," J. Opt. Soc. Am. B, vol. 13, pp. 1803-1816, Aug. 1996.

Efficient and accurate modeling of multi-wavelength propagation in SOAs: a generalized coupled-mode approach

Cristian Antonelli, Antonio Mecozzi, *Fellow, OSA, Fellow, IEEE*, Wangzhe Li, and Larry Coldren, *Fellow, OSA, Fellow, IEEE*

Abstract—We present a model for multi-wavelength mixing in semiconductor optical amplifiers (SOAs) based on coupled-mode equations. The proposed model applies to all kinds of SOA structures, takes into account the longitudinal dependence of carrier density caused by saturation, it accommodates an arbitrary functional dependencies of the material gain and carrier recombination rate on the local value of carrier density, and is computationally more efficient by orders of magnitude as compared with the standard full model based on space-time equations. We apply the coupled-mode equations model to a recently demonstrated phase-sensitive amplifier based on an integrated SOA and prove its results to be consistent with the experimental data. The accuracy of the proposed model is certified by means of a meticulous comparison with the results obtained by integrating the space-time equations.

Index Terms—Semiconductor optical amplifiers, nonlinear optics, wave mixing.

I. INTRODUCTION

Semiconductor optical amplifiers (SOAs) have been in the spotlight for many years, attracting ever growing interest in multiple areas of applications. These include all-optical signal processing in fiber-optic communication networks, cost-effective local area transmission, and, more recently, integrated silicon photonics, where SOAs are the building blocks for the implementation of large-scale integrated photonic circuits. Many of these applications rely on the mixing of the wavelength components of the propagating electric field, and their theoretical study can be performed by numerically integrating the coupled nonlinear equations describing the evolution of the electric field envelope in the longitudinal direction along the SOA, and the temporal carrier dynamics [1], [2]. Obviously, this approach is not suitable for the efficient design of an SOA, owing to the intensive computational effort that it involves. The search for computationally efficient and analytically tractable models has yield the formulation of what is sometimes referred to as a *reduced model* for the nonlinear SOA response [3], where the space-time equations reduce to a single ordinary differential equation [3], suitable for the analytic study of multi-wave mixing (see e.g. [3]–[5]). The formulation of a reduced model hinges upon two major assumptions. The first is that the spontaneous carrier

recombination rate is proportional to the carrier spatial density, and the second is that the material gain also depends linearly on the carrier density. These assumptions emanate from early studies of semiconductor lasers. Indeed, in lasers the carrier density dynamics is characterized by small deviations from a steady state value which is set by the threshold condition of gain equalling the cavity loss. The small deviations around this value are only caused by amplified spontaneous emission (ASE) and by some spatial hole burning, which is however of little significance because in most structures the intra-cavity optical intensity is only moderately inhomogeneous. Consequently, in laser structures, gain and spontaneous emission rate can be accurately described by a linearized expression around the steady state carrier density. Early studies on SOA structures also used linear expressions for gain and carrier recombination, and in this case the linearization, albeit less accurate, found its ground on its simplicity and, more importantly, on the limited gain of legacy SOAs, which implied a limited longitudinal inhomogeneity of the optical field in the optical waveguide.

Unfortunately, these assumptions do not reflect the characteristics of modern SOAs, as is clarified in what follows. Modern SOAs may have linear gain in excess to 40dB, implying a pronounced longitudinal inhomogeneity of the field intensity and hence of gain saturation. This may cause, in some cases, that the gain is only slightly saturated at the waveguide input, whereas it is almost zero at the waveguide output, where saturation is so high that the carrier density approaches its transparency value. When this is the case, a linear expression for the gain is reasonably accurate only if the gain does not deviate significantly from the linear expansion around the transparency carrier density over a range of values. The nowadays widely accepted forms for the dependence of the material gain on carrier density do not meet this requirement, because over such wide range of carrier density values the nonlinearity cannot be neglected, especially in quantum-well (QW) SOAs devices [6]. This makes the use of linear forms for the gain not an option for an accurate and quantitative description of the SOA dynamics. In addition, advances in material fabrication have made in modern devices the contribution of defect-induced carrier recombination, which is proportional to the carrier density N, negligible, with the consequence that spontaneous carrier recombination is dominated primarily by radiative recombination, whose rate is proportional to N^2, and secondarily by Auger recombination, whose rate is proportional to N^3 [6]. This reality makes the linearization

of the spontaneous recombination rate also a questionable approximation. All these arguments together suggest that the accuracy of models of the nonlinear SOA response based on linearization of the carrier recombination rate and gain may be, in state-of-the-art devices, highly inaccurate.

A natural approach to the study of wave mixing in SOAs, which closely reminds coupled-mode theories, is the one based on the derivation of evolution equations for the complex amplitudes of the field frequency components. Somewhat surprisingly, studies of wave mixing in modern SOAs (that is, SOAs characterized by a nonlinear dependence of the recombination rate and material gain on carrier density) based on this approach seem to be absent in the literature. In a couple of recent papers [7], [8], the authors assume a linear gain and a polynomial recombination rate, as it would be appropriate for bulk SOAs. However, they express the recombination rate as $R(N) = N/\tau_c(N)$, where $\tau_c(N) = N/R(N)$ has the meaning of an equivalent spontaneous carrier lifetime and, in the derivation of the coupled-mode equations, they replace $\tau_c(N)$ with some time- and space-independent value. This makes, again, the assumed carrier recombination rate linear.

Another distinctive assumption of all existing coupled-mode approaches to multi-wave mixing in SOAs is that the carrier density modulation induced by the mixing is characterized by a single harmonic component [8]. This is a reasonable assumption when a single frequency component is dominant over the others, like for instance, in four-wave mixing (FWM) experiments where a single pump and a frequency-detuned weak signal are injected into the SOA. On the contrary, this assumption is not satisfied when multiple frequency components, detuned by a few gigahertz, have comparable intensities. This configuration characterizes for instance experiments where two strong pumps are injected at frequencies $-\Omega + \omega_0$ and $\Omega + \omega_0$, and one is interested in the amplification of a weak signal injected at the central frequency ω_0. In this case, the strongest carrier modulation occurs at the beat frequency 2Ω between the two strong pumps, but the signal amplification is mainly affected by the, possibly weaker, carrier modulation at frequency Ω. This configuration recently became of great interest because it describes the operation of a relevant class of SOA-based phase sensitive amplifiers (PSAs) [9]–[12].

In this paper, we derive coupled-mode equations describing multi-wavelength mixing in SOAs characterized by arbitrary functional dependencies of the recombination rate and material gain on carrier density. These include both QW and bulk SOAs. The proposed model, which in what follows we refer to as the *couple-mode model*, takes into account the frequency dependence of the material gain, as well as all orders of the waveguide dispersion, and accommodates input optical waveforms consisting of arbitrary combinations of multiple frequency components.[1] The implementation of the model is illustrated in detail in the case of a QW SOA characterized by a logarithmic dependence of the optical gain on the carrier density N, and by a cubic-polynomial carrier recombination rate $R(N)$. The accuracy of the coupled-mode model is successfully tested (unlike in previous related studies) by means of a meticulous comparison with the results obtained by integrating the space-time equations of the SOA full model. Remarkably, owing to their inherent simplicity, the coupled-mode equations imply computational costs by orders of magnitude smaller that those required by the space-time equations, thus enabling the efficient characterization of multi-wave mixing in SOA structures, which would be otherwise highly impractical. We then apply the derived coupled-mode equations to studying the operation of a recently demonstrated dual-pumped PSA based on an integrated QW SOA [11]. We prove the results to be consistent with the experimental data, and confirm the excellent agreement with the results obtained by using the full SOA model.

II. COUPLED-MODE EQUATIONS FOR MULTI-WAVELENGTH PROPAGATION IN SOAS

We denote by $E(z,t)$ the slowly-varying complex envelope of the electric field propagating in the SOA in the temporal reference frame that accommodates the field group velocity v_g, corresponding to the real field

$$\mathcal{E}(z,t) = \mathrm{Re}\left[E\left(z, t - \frac{z}{v_g}\right) e^{-i[\omega_0 t - \beta(\omega_0)z]}\right], \quad (1)$$

with ω_0 being the optical frequency. The field envelope E is normalized so that that $|E|^2$ is the optical power flowing through the transverse waveguide section. It is related to the photon flux P in photons per unit time and area through the relation

$$|E|^2 = \hbar\omega_0 S_{\mathrm{mod}} P, \quad (2)$$

where $S_{\mathrm{mod}} = S/\Gamma$ is the modal area of the waveguide, with S denoting the effective SOA area and Γ the optical confinement factor. The evolution of $E(z,t)$ along the SOA is governed by the familiar equation

$$\frac{\partial E}{\partial z} = \frac{1}{2}\left[(1 - i\alpha)\Gamma\hat{g} - \alpha_{\mathrm{int}}\right] E + i\hat{\beta}E + r_{\mathrm{sp}}, \quad (3)$$

where α is the Henry factor, α_{int} is the SOA internal loss coefficient, and r_{sp} is the spontaneous emission noise term. By $\hat{g}$ and $\hat{\beta}$ we denote the material gain operator and the wavenumber operator. The operator formalism allows us to

---

[1]We consider here only the nonlinearity that comes from carrier modulation, neglecting ultrafast nonlinearity arising from carrier heating, two photon absorption and spectral hole burning. This choice has been motivated to keep the analysis simple, and also because we are interested to cases where nonlinearity is large enough to be used in all-optical processing applications or to be an issue in applications where linearity is sought for. In these cases, the frequency detuning does not exceed a few tens of gigahertz, and in this detuning range the nonlinear modulation is mostly caused by carriers. The inclusion of ultrafast processes, however, does not pose any conceptual difficulties, and can be done along the lines of ref. [14] assuming that the gain depends on quantities other than carrier density, like e.g. the carrier temperature for carrier heating, or the energy-resolved population of carriers for spectral hole burning, and assuming linear decay process of these quantities towards their steady state values.

conveniently accommodate the frequency dependence of the gain as well as the waveguide dispersion to any order. Within this formalism the two operators can be expressed as

$$\hat{g} = \sum_{m=0}^{\infty} \frac{1}{n!} \frac{\partial^n g(N,\omega_0)}{\partial \omega_0^n} \left(i\frac{\partial}{\partial t} \right)^n \tag{4}$$

$$\hat{\beta} = \sum_{m=2}^{\infty} \frac{1}{n!} \frac{d^n \beta(\omega_0)}{d\omega_0^n} \left(i\frac{\partial}{\partial t} \right)^n, \tag{5}$$

where $g(N,\omega)$ is the gain coefficient expressed as a function of the carrier density N and the optical frequency ω, and $\beta(\omega)$ is the frequency-dependent field propagation constant. The expressions for $\hat{g}$ and $\hat{\beta}$ in Eqs. (4) and (5) are obtained by expanding $g(N,\omega)$ and $\beta(\omega)$ around the carrier frequency ω_0. The fact that the sum in Eq. (5) starts from $n=2$ is consistent with the definition of $E(z,t)$ in Eq. (1), which already accounts for the effect of $\beta(\omega_0)$ and $d\beta(\omega_0)/d\omega_0 = 1/v_g$.

The spontaneous emission noise term r_{sp} is modeled as a zero-mean, complex phase independent random process. It depends explicitly on the carrier density, besides time and space, i.e. $r_{sp} = r_{sp}(N,t;z)$. Its correlation function is

$$\mathbb{E}\left[r_{sp}^*(N,t;z) r_{sp}(N,t';z') \right] = \hbar\omega_0 R_{sp}'(N,t-t')\delta(z-z'), \tag{6}$$

where by the symbol $\mathbb{E}$ we denote ensemble averaging. Here the term $\delta(z-z')$ accounts for the fact that different longitudinal waveguide sections provide statistically independent contributions to the noise term, and

$$R_{sp}'(N,t'-t) = \int e^{-i(\omega-\omega_0)(t'-t)} n_{sp}(N,\omega)\Gamma g(N,\omega) \frac{d\omega}{2\pi}, \tag{7}$$

is the spontaneous emission rate into the waveguide mode and in the field propagation direction, with n_{sp} denoting the population inversion factor. Spontaneous emission is a small perturbation of the propagating field, so that we may safely replace N with its temporal average, thus neglecting the effect of its small fluctuations around this value. Within this approximation the process of spontaneous emission can be modeled as a stationary process in time.

The equation for the carrier density is

$$\frac{\partial N}{\partial t} = R_J - R_{sp} - R_{nr} - R_{st} \tag{8}$$

where

$$R_J = \frac{J w_a L}{V} = \frac{J}{ed}, \tag{9}$$

is the carrier injection rate into the active volume $V = SL = w_a dL$, where w_a is the active region width, L is the active region length, and d is the active region thickness. The term $R_{sp}(N)$ is the recombination rate associated to spontaneous emission, and its well approximated by the quadratic expression $R_{sp}(N) = BN^2$. By $R_{nr}(N)$ we denote the non-radiative recombination rate, which we express as $R_{nr}(N) = AN + CN^3$, where the linear contribution AN is mostly due to defect-induced recombination, and the cubic contribution CN^3

to Auger recombination[2]. As for the stimulated recombination, under the assumption that each stimulated emission process corresponds to the emission of one photon and the annihilation of one carrier, the stimulated recombination rate R_{st} (which also accounts for spontaneous emission within the waveguide mode) is related to the photon flux P through

$$R_{st}Sdz = S_{mod}\left[P(z+dz)-P(z)\right] \Longrightarrow R_{st} = \frac{1}{\Gamma}\frac{\partial P}{\partial z}. \tag{10}$$

By combining the various mechanisms, Eq. (8) becomes

$$\frac{\partial N}{\partial t} = -R(N) + \frac{J}{ed} - \frac{1}{\hbar\omega_0 S}\frac{\partial |E|^2}{\partial z}, \tag{11}$$

where by $R(N)$ we denote the familiar recombination rate[3]

$$R(N) = AN + BN^2 + CN^3. \tag{12}$$

By expanding the derivative $\partial|E|^2/\partial z$ and using Eq. (3), Eq. (11) assumes the form

$$\frac{\partial N}{\partial t} = -R(N) + \frac{J}{ed} - \frac{1}{\hbar\omega_0 S}\text{Re}\left[E^*(1-i\alpha)\Gamma\hat{g}E\right], \tag{13}$$

where we used the fact that $\hat{\beta}$ is a Hermitian operator, and hence it does not contribute to $\partial|E|^2/\partial z$. The last term at the right-hand side of Eq. (13) reduces to the familiar form $\Gamma g|E|^2/\hbar\omega_0 S$ if the gain coefficient is assumed to be frequency independent. In Eq. (13), we neglected the rate of carrier depletion associated to the photons spontaneously emitted in the guided mode, i.e. the term $R_{sp}'(N,0)$ that comes from $\partial|E|^2/\partial z$ of Eq. (11), because this term is small compared the carrier depletion rate caused by the photons spontaneously emitted over all spatial modes BN^2, which is part of $R(N)$.

We note that Eqs. (3) and (13) can be generalized so as to include the field polarization in the analysis. While this task is rather straightforward and does not involve any conceptual challenge, we intentionally ignore polarization-related issues in order to keep the focus on the main objective of this work, which is the study of multi-wavelength propagation.

We express the multi-wavelength electric field and the carrier density as follows,

$$E(z,t) = \sum_k E_k(z)e^{-ik\Omega t} \tag{14}$$

$$N(z,t) = N_0(z) + \sum_k \Delta N_k(z)e^{-ik\Omega t}, \tag{15}$$

where the coefficients ΔN_k must satisfy the equality $\Delta N_{-k}(z) = \Delta N_k^*(z)$ for $N(z,t)$ to be real. The term

[2]We note that, while the resulting cubic polynomial expression $AN + BN^2 + CN^3$ has been shown to fit very well the experimental data in most cases [6], the one-to-one correspondence between the three terms of the polynomial and the three recombination mechanisms is not always as neat as is illustrated in the main text. For instance, in the case of non-parabolic bands (the normal case), radiative recombination is also non-parabolic and is best modeled with a bit of linear component; carrier leakage (due to finite QW barriers) has an exponential dependence and requires a polynomial fit, affecting the numerical values of A, B, and C.

[3]This expression of $R(N)$ is widely established and is given here for consistency with previous studies. We stress, however, that the analysis that follows does not make use of it explicitly, and rather applies to arbitrary expressions of $R(N)$.

$N_0(z) + \Delta N_0(z)$ is the z-dependent time-independent value of the carrier density that characterizes the system when it achieves its stationary state, and $N_0(z)$ is defined as the solution of

$$\frac{J}{ed} = R(N_0) + \frac{\Gamma}{\hbar\omega_0 S} \sum_k g(N_0, \omega_k)|E_k|^2. \quad (16)$$

For values of the frequency spacing $\Omega/2\pi$ that exceed the SOA modulation bandwidth, the temporal fluctuations of $N(z,t)$ around its stationary value are filtered by the carrier dynamics and hence they can be treated within a perturbation approach. A consequence of this situation is that the deviation $\Delta N_0(z)$ of the stationary carrier density value from $N_0(z)$ is also a perturbation, and is small compared to $N_0(z)$. In this framework, all carrier-density dependent quantities that appear in Eqs. (3) and (13) can thus be expanded to first order with respect to $\Delta N = N - N_0$, namely

$$R(N) = R(N_0) + \frac{\Delta N}{\tau(N_0)} \quad (17)$$

$$g(N, \omega) = g(N_0, \omega) + g_N(N_0, \omega)\Delta N, \quad (18)$$

where by the subscript N we denote differentiation with respect to N. The quantity

$$\tau(N_0) = R_N(N_0)^{-1} = \left[\left.\frac{dR(N)}{dN}\right|_{N=N_0} \right]^{-1}, \quad (19)$$

is the spontaneous carrier lifetime, and

$$g_N(N_0, \omega) = \left.\frac{\partial g(N, \omega)}{\partial N}\right|_{N=N_0}, \quad (20)$$

is the differential gain. We stress that *these are z-dependent quantities*, owing to the fact that $N_0 = N_0(z)$, and hence their values evolve along the SOA. We also notice that the effective carrier lifetime governing the dynamics of carrier modulation around the steady state value is the *differential* carrier lifetime $\tau(N_0)$ given in Eq. (19) and also introduced in [15], and not the *total* carrier lifetime $\tau_c(N_0) = N_0/R(N_0)$ used in Refs. 7 and 8. The difference between these two quantities is approximately a factor of 2 when the radiative bimolecular recombination BN^2 is the dominant contribution to $R(N)$, or 3 when the Auger recombination CN^3 is dominant. By inserting Eqs. (17) and (18) into Eq. (3) and Eq. (13) we obtain

$$\frac{\partial E}{\partial z} = \frac{1}{2}\left[(1 - i\alpha)\Gamma(\hat{g}_0 + \Delta N\hat{g}_N) - \alpha_{\text{int}}\right]E + i\hat{\beta}E + r, \quad (21)$$

and

$$\frac{\partial \Delta N}{\partial t} = -\frac{\Delta N}{\tau(N_0)} - \left[R(N_0) - \frac{J}{ed}\right]$$
$$- \frac{\text{Re}\left[E^*(1 - i\alpha)\Gamma\hat{g}_0 E\right]}{\hbar\omega_0 S}$$
$$- \Delta N\frac{\text{Re}\left[E^*(1 - i\alpha)\Gamma\hat{g}_N E\right]}{\hbar\omega_0 S}, \quad (22)$$

where the operators $\hat{g}_0$ and $\hat{g}_N$ are defined as in Eq. (4), provided that $g(N, \omega)$ is replaced with $g(N_0, \omega)$ and $g_N(N_0, \omega)$, respectively.

26

The evolution equation for the electric field coefficient E_k is obtained by inserting the expression of the field (14) in Eq. (21) and by equating the coefficient of the term $\exp(-ik\Omega t)$ at the two sides of the resulting equation. As a result, one finds

$$\frac{dE_k}{dz} = \left[\frac{1}{2}(1 - i\alpha)\Gamma g(N_0, \omega_k) - \alpha_{\text{int}} + i\beta(\omega_k)\right]E_k$$
$$+ \frac{1}{2}(1 - i\alpha)\sum_n \Delta N_{k-n}\Gamma g_N(N_0, \omega_n)E_n + r_k, \quad (23)$$

where we used $\hat{g}_0 E = \sum_k g(N_0, \omega_k)E_k \exp(-ik\Omega t)$ and $\hat{g}_N E = \sum_k g_N(N_0, \omega_k)E_k \exp(-ik\Omega t)$, with $\omega_k = \omega_0 + k\Omega$. The noise term r_k is defined by

$$r_k(N; z) = \int dt e^{ik\Omega t} r_{\text{sp}}(N, t; z), \quad (24)$$

has zero mean $\langle r_k(N; z)\rangle = 0$, and its variance follows from

$$\langle r_k^*(N; z)r_h(N; z')\rangle = \delta(z - z')\hbar\omega_0$$
$$\times \int dt \int dt' \exp[i\Omega(kt' - ht)]R'_{\text{sp}}(N, t' - t). \quad (25)$$

Using the stationarity of R'_{sp}, we may express the above as

$$\langle r_k^*(N; z)r_h(N; z')\rangle = \delta_{k,h}\delta(z - z')\hbar\omega_0$$
$$\times n_{\text{sp}}(N, \omega_0 + k\Omega)\Gamma g(N, \omega_0 + k\Omega). \quad (26)$$

The terms $r_k(N; z')$, $k = 0, \pm 1, \pm 2 \ldots$ are therefore a set of independent-phase, spatially-uncorrelated noise terms, which can be modeled as differentials of independent Wiener processes. At this point we can recast Eq. (23) in the following compact form

$$\frac{d\vec{E}}{dz} = \left[\frac{1}{2}(1 - i\alpha)\Gamma(\mathbf{G} + \mathbf{H}) - \alpha_{\text{int}}\mathbf{I} + i\mathbf{b}\right]\vec{E} + \vec{r}, \quad (27)$$

where $\vec{E}$ and $\vec{r}$ are column vectors constructed by stacking the electric field coefficients E_k and the noise projections r_k one on top of another, respectively, with E_0 and r_0 occupying the central position, namely $\vec{E} = [\ldots E_2, E_1, E_0, E_{-1}, E_{-2} \ldots]^t$, and the same for $\vec{r}$ (the superscript t stands for "transposed"). The vector $\vec{E}$ and $\vec{r}$ are of course infinite-dimensional, and so are the square matrices $\mathbf{G}$, $\mathbf{H}$ and $\mathbf{b}$. Consistently with the definition of $\vec{E}$, we use positive and negative indices to identify the elements of these matrices, with the $(0, 0)$ element occupying the central position. In particular, $\mathbf{G}$ and $\mathbf{b}$ are diagonal matrices whose (k, k) elements are equal to $G_{k,k} = g(N_0, \omega_k)$ and $b_{k,k} = \beta(\omega_k) - \beta(\omega_0) - k\Omega d\beta(\omega_0)/d\omega_0$, respectively, whereas the (k, n) element of $\mathbf{H}$ is $H_{k,n} = \Delta N_{k-n}g_N(N_0, \omega_n)$. By $\mathbf{I}$ we denote the identity matrix (regardless of its dimensions).

We now proceed to the extraction of the carrier density coefficients ΔN_k by equating the terms proportional to $\exp(-ik\Omega t)$ at the two sides of Eq. (22), when the expression of ΔN in Eq. (15) is inserted in it. After some straightforward algebra, involving the use of Eq. (16), one obtains

$$(1 - ik\tau\Omega)\Delta N_k = -\sum_h \Delta N_h p_{k,h} + \mathcal{N}_k. \quad (28)$$

where

$$\begin{aligned}
\mathcal{N}_k = & -\tau(N_0)R(N_0)(1-\delta_{k,0}) \\
& \times \sum_n \left[\frac{(1-i\alpha)E_{n+k}E_n^*}{P_{\text{stim}}(N_0,\omega_{n+k})} + \frac{(1+i\alpha)E_{n+k}E_n^*}{P_{\text{stim}}(N_0,\omega_n)} \right]
\end{aligned} \tag{29}$$

$$p_{k,h} = \sum_n \left[\frac{(1-i\alpha)E_{n+k-h}E_n^*}{P_{\text{sat}}(N_0,\omega_{n+k-h})} + \frac{(1+i\alpha)E_{n+k-h}E_n^*}{P_{\text{sat}}(N_0,\omega_n)} \right]. \tag{30}$$

The quantity

$$P_{\text{sat}}(N_0,\omega) = \frac{\hbar\omega_0 S}{\tau(N_0)\Gamma g_N(N_0,\omega)}, \tag{31}$$

is the familiar saturation power, although its definition accounts for the frequency dependence of the gain coefficient explicitly, and

$$P_{\text{stim}}(N_0,\omega) = R(N_0)\frac{\hbar\omega_0 S}{\Gamma g(N_0,\omega)}. \tag{32}$$

is the power value above which carrier depletion is dominated by stimulated emission. We hence refer to P_{stim} as to *stimulated* power. Equation (28) can be conveniently recast in the following compact form

$$(\mathbf{I} - i\tau\Omega\mathbf{k} + \mathbf{p})\Delta\vec{N} = \vec{\mathcal{N}} \tag{33}$$

where the (k,h) element of the matrix $\mathbf{p}$ is equal to $p_{k,h}$, and $\mathbf{k}$ is a diagonal matrix with diagonal elements $\kappa_{k,k} = k$. The column vectors $\Delta\vec{N}$ and $\vec{\mathcal{N}}$ are constructed (like the field vector $\vec{E}$) by stacking the coefficients ΔN_k and $\mathcal{N}_k$ one on top of another, respectively, namely, $\Delta\vec{N} = [\ldots, \Delta N_1, \Delta N_0, \Delta N_{-1}, \ldots]^t$ and $\vec{\mathcal{N}} = [\ldots, \mathcal{N}_1, 0, \mathcal{N}_{-1}, \ldots]^t$. The coefficients N_0 and ΔN_k are hence obtained for a given electric field state by solving Eqs. (16) and (33). These are the most general coupled-mode equations accounting for any functional dependence of the recombination rate and material optical gain on carrier density, as well as for the frequency dependence of the gain and waveguide dispersion.

III. IMPLEMENTATION OF THE COUPLED-MODE EQUATION MODEL IN REALISTIC SOA STRUCTURES

As is customarily done in most studies of practical relevance, where the waveguide dispersion and the frequency dependence of the gain coefficient have been shown to play a minor role, in this section we neglect chromatic dispersion, as well as higher-order dispersion, and assume frequency-independent gain. With this simplification the matrices $\mathbf{G}$, $\mathbf{H}$, and $\mathbf{p}$ become frequency-independent and assume a very convenient form, as is shown in what follows. We also neglect the presence of spontaneous emission noise terms, whose implications on the SOA performance, chiefly on the SOA noise figure, will be the subject of future work.

The multi-wavelength propagation model introduced in the previous section involves an infinite number of coefficients E_k and ΔN_k, a situation that is obviously incompatible with its implementation in any numerical platform. However, as will be shown in the next section, high-order coefficients (namely E_k and ΔN_k coefficients with large values of $|k|$) provide

a negligible contribution to the solution of Eqs. (16), (27), and (33), and hence they can be omitted by truncating the vectors $\vec{E}$ and $\Delta\vec{N}$. The truncation of $\vec{E}$ and $\Delta\vec{N}$ requires of course that all matrices involved in Eqs. (27) and (33) be also truncated accordingly. In what follows we provide explicit expressions for those matrices and discuss the procedure that allows the efficient computation of $\vec{E}$ and $\Delta\vec{N}$.

The truncation procedure of the infinite set of equations (27) can be performed in a number of ways. One possible approach is assuming that $E_k(z) = 0$ for $|k| > M$. Here M is an integer number that can be determined self consistently by checking that the integration of the equations for $M \to M+1$ yields indistinguishable results. This assumption implies $\Delta N_k(z) = 0$ for $|k| > 2M$, owing to the absence of beat terms at frequency offsets larger than $2M\Omega$. A simpler yet equally accurate approach is to assume that the carrier density coefficients $\Delta N_k(z)$ are also zero at frequency offsets greater than $M\Omega$. Here we adopt the latter approach, within which Eqs. (14) and (15) specialize to

$$E(z,t) = \sum_{k=-M}^{M} E_k(z)e^{-ik\Omega t} \tag{34}$$

$$N(z,t) = N_0(z) + \sum_{k=-M}^{M} \Delta N_k(z)e^{-ik\Omega t}. \tag{35}$$

Accordingly, the field vector $\vec{E}$ and carrier density modulation vector $\Delta\vec{N}$, consist of $(2M + 1)$ components. Matrices $\mathbf{G}$ and $\mathbf{H}$ in Eq. (27) become $(2M + 1) \times (2M + 1)$ matrices. In particular, owing to the assumption of frequency-flat gain, one can readily verify the equalities $\mathbf{G} = g(N_0)\mathbf{I}$, and $\mathbf{H} = g_N(N_0)\mathbf{T}(\Delta\vec{N})$, where by $\mathbf{T}_{2M+1}(\Delta N_k)$ we denote a Hermitian-symmetric Toeplitz matrix [16]. Below we give the expression of $\mathbf{T}_{2M+1}(\Delta N_k)$ in the case $M = 2$ for illustration purposes,

$$\mathbf{T}_5(\Delta N_k) = \begin{bmatrix} \Delta N_0 & \Delta N_1 & \Delta N_2 & 0 & 0 \\ \Delta N_1^* & \Delta N_0 & \Delta N_1 & \Delta N_2 & 0 \\ \Delta N_2^* & \Delta N_1^* & \Delta N_0 & \Delta N_1 & \Delta N_2 \\ 0 & \Delta N_2^* & \Delta N_1^* & \Delta N_0 & \Delta N_1 \\ 0 & 0 & \Delta N_2^* & \Delta N_1^* & \Delta N_0 \end{bmatrix}. \tag{36}$$

The neglect of the waveguide dispersion yields $\mathbf{b} = 0$, and hence Eq. (27) simplifies to

$$\frac{d\vec{E}}{dz} = \left[\frac{(1-i\alpha)g(N_0) - \alpha_{\text{int}}}{2}\mathbf{I} + \mathbf{T}_{2M+1}(\Delta N_k) \right]\vec{E}, \tag{37}$$

where N_0 is the solution of

$$\frac{J}{ed} = R(N_0)\left[1 + \frac{|\vec{E}|^2}{\tau P_{\text{stim}}(N_0)} \right], \tag{38}$$

$$P_{\text{stim}}(N_0) = R(N_0)\frac{\hbar\omega_0 S}{\Gamma g(N_0)}. \tag{39}$$

The expression for the carrier density modulation vector $\Delta\vec{N}$

27

Description	Value	Units
Linear recombination coefficient A	0	s^{-1}
Bimolecular recombination coefficient B	0.3×10^{-10}	cm^3/s
Auger coefficient C	3.3×10^{-29}	cm^6/s
Optical confinement factor Γ	10%	
Linewidth enhancement factor α	5	
Optical wavelength λ_0	1561	nm
Group velocity v_g	$8.33 \cdot 10^9$	cm/s
Active region width w_a	2×10^{-4}	cm
Active region tickness d	65×10^{-7}	cm
Active region length L	0.1	cm
Gain coefficient g_0	1800	cm^{-1}
Transparency carrier density N_{tr}	2×10^{18}	cm^{-3}
SOA internal loss α_{int}	5	cm^{-1}
Injection current density J	3.4×10^3	A/cm^2
Frequency spacing $\Omega/2\pi$	8.6	GHz

simplifies to

$$\Delta \vec{N} = -\frac{\tau R(N_0)}{P_{\text{stim}}(N_0)} \left[\mathbf{I} - \tau \Omega \mathbf{k} + \frac{\mathbf{T}_{2M+1}(C_k)}{P_{\text{sat}}(N_0)} \right]^{-1} \vec{C}$$

(40)

$$P_{\text{sat}}(N_0) = \frac{\hbar \omega_0 S}{\tau(N_0) \Gamma g_N(N_0)}$$

(41)

where C_k is the discrete autocorrelation function of $\vec{E}$, namely

$$C_k = \sum_{n=-M}^{M} E_{n+k} E_n^*,$$

(42)

where we assume $E_n = 0$ for $|n| > M$. The expression of $\vec{C}$ in the case $M = 2$ is

$$\vec{C} = [C_2, C_1, C_0, C_1^*, C_2^*]^t,$$

(43)

and that of $\mathbf{T}_5(C_k)$ is

$$\mathbf{T}_5(C_k) = \begin{bmatrix} C_0 & C_1 & C_2 & C_3 & C_4 \\ C_1^* & C_0 & C_1 & C_2 & C_3 \\ C_2^* & C_1^* & C_0 & C_1 & C_2 \\ C_1^* & C_2^* & C_1^* & C_0 & C_1 \\ C_2^* & C_1^* & C_2^* & C_1^* & C_0 \end{bmatrix},$$

(44)

where we used $C_{-k} = C_k^*$, as can be readily verified by inspecting Eq. (42).

The numerical integration of the coupled-equations involves a three-step procedure for the transition from z to $z + \Delta z$, given the field vector $\vec{E}(z)$. These are:

1) Find the value of $N_0(z)$ by solving Eq. (38);
2) Extract the carrier density vector $\Delta \vec{N}(z)$ as in Eq. (40);
3) Evaluate the field vector $\vec{E}(z + \Delta z)$ by solving Eq. (37) from z to $z + \Delta z$ while using the values of N_0 and ΔN_k obtained in steps 1 and 2, according to

$$\vec{E}(z + \Delta z) = \exp \left\{ \frac{(1 - i\alpha)g[N_0(z)] - \alpha_{\text{int}}}{2} \Delta z \right\}$$
$$\exp \left\{ \mathbf{T}_{2M+1}[\Delta N_k(z)] \Delta z \right\} \vec{E}(z) \quad (45)$$

A. Model validation

In this section we test the accuracy of the proposed multi-wavelength propagation model against the results obtained by integrating the full model' space-time equations (3) and (13). To this end we consider a QW SOA, characterized by the following logarithmic functional dependence of the gain coefficient on carrier density [6]

$$g(N) = g_0 \log \left(\frac{N}{N_{\text{tr}}} \right),$$

(46)

where g_0 is a gain parameter and N_{tr} is the carrier density required for transparency.[4] The expansion of the gain function is in this case $g(N) \simeq g(N_0) + g_N(N_0)\Delta N$, with

$$g(N_0) = g_0 \log \left(\frac{N_0}{N_{\text{tr}}} \right), \quad g_N(N_0) = \frac{g_0}{N_0}.$$

(47)

The physical and operational parameters of the SOA are listed in Table I (we note that the SOA is operated with the injection current density $J = 8.5 J_{\text{tr}}$, where $J_{\text{tr}} = ed(AN_{\text{tr}} + BN_{\text{tr}}^2 + CN_{\text{tr}}^3)$ is the injection current density required for transparency). The SOA is injected with a three-wavelength optical signal characterized by the complex envelope

$$E_{\text{in}}(t) = \sqrt{W_1} \, e^{-i\Omega t} + \sqrt{W_0} + \sqrt{W_{-1}} \, e^{i\Omega t}$$

(48)

with $W_1 = W_{-1} = -2$dBm, and $W_0 = -7$dBm. For this set of parameters we solved the coupled-mode equations (37), (39), and (40) with the input field vector $\vec{E}_{\text{in}} = [\cdots 0, \sqrt{W_1}, \sqrt{W_0}, \sqrt{W_{-1}}, 0 \cdots]^t$. We used $M = 6$ and checked that larger values of M yield indistinguishable results. We then integrated the full model's equations (3) and (13) with the procedure described in [17], and extracted the coefficients $E_k(z)$ from the numerical solution $E_{\text{num}}(z,t)$ according to

$$E_k(z) \leftrightarrow \frac{\Omega}{2\pi} \int_{t_0}^{2\pi/\Omega} E_{\text{num}}(z,t) e^{ik\Omega t} \mathrm{d}t,$$

(49)

where by t_0 we denote any time at which the system achieved its stationary state. The results are shown in Fig. 1. In the top panel we plot by solid curves the intensities of the coefficients $E_k(z)$ versus the normalized propagation distance z/L for values of k ranging between $k = -4$ and $k = 4$. By circles we plot the results obtained with the full model. The excellent accuracy of the coupled-mode model is self-evident. Interestingly, the figure shows that the coupled-mode model is accurate in describing the formation of four-wave mixing components that eventually (at the SOA output) exceed some of the input components. The lower panel of the same figure shows the corresponding phases of the field coefficients E_k (more precisely the solid curves are the plot of $\text{Phase}[E_k(z)] + k\Omega z/v_g$, where the second term accounts for the fact that the coefficients $E_k(z)$ characterize the field envelope in the time reference delayed by z/v_g).

In Fig. 2 we illustrate the dependence of the coupled-mode model's results on the number of field coefficients that are considered. In the top panel we plot the output intensities

---

[4]Of course, the use of different functional forms of $g(N)$, for instance the more accurate three parameter expression $g(N) = g_0 \ln[(N + N_s)/(N_{\text{tr}} + N_s)]$ also reported in [6], is fully equivalent in terms of model complexity.
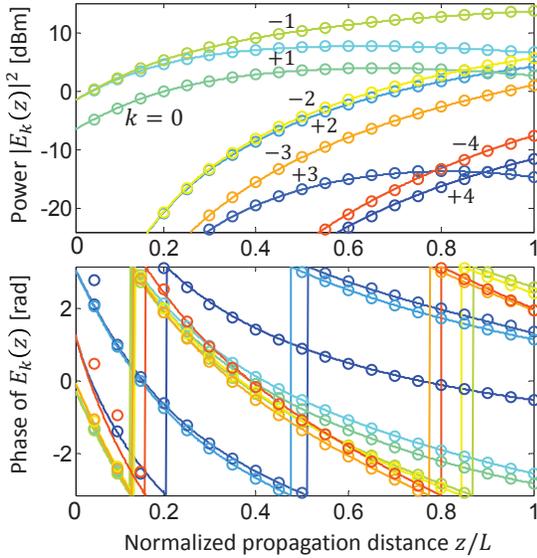
Fig. 1. Intensity (top panel) and phase (bottom panel) of the field components E_k versus normalized propagation distance z/L for the displayed values of k and for the SOA parameters' values in Table I. Solid curves refer to the coupled-mode model, while circles were obtained by solving the space-time equations of the full model.

Fig. 2. Intensities of field components E_k at the SOA output $|E_k(L)|^2$, as obtained by using the coupled-mode model, for increasing values of M. Each curve corresponds to a specific value of k and hence it originates at $|k| = M$. The top panel refers to the set of parameters listed in Table I and used in Fig. 1, whereas in the bottom panel the optical confinement factor was increased from 10% to 20%.

$|E_k(L)|^2$ evaluated by solving the coupled-mode equations for increasing values of M, with each curve corresponding to a different value of k. Since the accounting for the frequency component E_k dictates that $M \geqslant |k|$, the curve referring to E_k originates at $M = |k|$. The plot shows that in the numerical example considered here the results of the coupled-mode equations for the component E_k become accurate (that is, the corresponding curve in the figure becomes flat) for M exceeding $|k|$ by a one or two units. However, it should be pointed out that the convergence to the correct result is affected by the specific SOA parameters' value and may be slower. This is shown in the lower panel of the Fig. 2, where the same curves plotted in the top panel are re-calculated by increasing the SOA optical confinement factor from 10% to 20% and by leaving the other SOA parameters unchanged. In this example, it can be seen that using $M < 6$ may yield an error in the calculation of $|E_1(L)|^2$ up to a factor of 100.

IV. APPLICATION OF THE MODEL: DUAL-PUMPED SOA-BASED PHASE-SENSITIVE AMPLIFIER

In this section we apply the coupled-mode model to the study of the dual-pumped SOA-based PSA presented in [11], [12]. The goal of this exercise is two-folded. On the one hand we aim to show that the phase-sensitive gain value obtained with the coupled-mode model assuming realistic SOA parameters is consistent with the experimentally obtained value. On the other hand, we show explicitly that by restricting the coupled-mode model to the pump and signal components only, as is sometimes done [18], yields significantly incorrect results when a realistic dependence of the amplifier gain on carrier density is used.

The waveform at the input of a PSA of the kind considered

here can be expressed as

$$E_{\text{in}}(t) = e^{i\phi_1}\sqrt{W_1}e^{-i\Omega t} + e^{i\phi_0}\sqrt{W_0} + e^{i\phi_{-1}}\sqrt{W_{-1}}e^{i\Omega t} \tag{50}$$

where by W_1 and W_{-1} we denote the optical powers of the two pumps and by ϕ_1 and ϕ_{-1} their absolute phases. The field component at the central frequency represent the input signal component. By removing in all components the immaterial average phase of the two pumps $\phi_c = (\phi_1 + \phi_{-1})/2$, and denoting by $\phi_s = \phi_0 - \phi_c$ the input signal phase relative to ϕ_c, the input field envelope can be expressed as

$$E_{\text{in}}(t) = e^{i\phi_p}\sqrt{W_1}e^{-i\Omega t} + e^{i\phi_s}\sqrt{W_0} + e^{-i\phi_p}\sqrt{W_{-1}}e^{i\Omega t}, \tag{51}$$

where $\phi_p = (\phi_1 - \phi_{-1})/2$. We further note that the effect of ϕ_p is limited to introducing an immaterial time shift $t_p = \phi_p/\Omega$, and hence it can be safely set to $\phi_p = 0$. We therefore solve the space-time equations using the following input waveform,

$$E_{\text{in}}(t) = \sqrt{W_{P_1}}e^{-i\Omega t} + e^{i\phi_s}\sqrt{W_s} + \sqrt{W_{P_2}}e^{i\Omega t}, \tag{52}$$

and the coupled-mode equations with the input field vector

$$\vec{E}_{\text{in}} = [\cdots, 0\,\sqrt{W_{P_1}},\, e^{i\phi_s}\sqrt{W_s},\, \sqrt{W_{P_2}}, 0, \cdots]^t. \tag{53}$$

The key quantity that characterizes the performance of the PSA under scrutiny is the dependence of the signal gain on the phase ϕ_s. In Fig. (3) we plot the gain $G_s(\phi_s) = |E_s(L)|^2/W_s$ (in decibels) as a function of ϕ_s, where in the case of the full model the term $E_s(L)$ is extracted from the numerical solution $E_{\text{num}}(L,t)$ according to Eq. (49) with $z = L$. The SOA parameters used in the numerical example are those given in Table I. The input pump powers were set to $W_{P_1} = W_{P_2} = -2$dBm, and the input signal power to the much smaller value $W_s = -22$dBm. The solid curve is obtained by integrating the

29
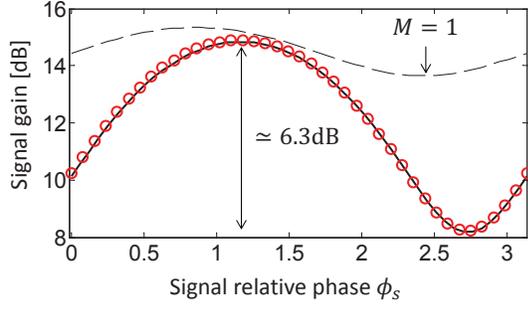
Fig. 3. Dual-pumped SOA-based PSA's gain versus the relative phase of the input signal ϕ_s introduced in Eq. (52). The SOA parameters used in the numerical computation are those given in Table I, the input pump powers were set to $W_{P_1} = W_{P_2} = -2$dBm, and the input signal power to $W_s = -22$dBm. The solid curve refers to the coupled-mode model with $M = 4$ (larger values of M yield indistinguishable results), while the circles were obtained by integrating the space-time equations of the full model. The dashed curve shows the results obtained with the coupled-mode model by propagating only the pump and signal components, namely by setting $M = 1$.

coupled-mode model with $M = 4$, whereas the circles refer to the space-time model. The excellent agreement between the coupled-mode model and the space-time model, like in the previous section, is self-evident. The thin dashed curve in Fig. 3 shows the result obtained with the coupled-mode model by including only the pump and signal field components, that is by using $M = 1$. The plot shows that the neglect of high-order four-wave mixing products yields higher gain values and a lower phase dependent gain.

Figure 4 depicts the schematic of the signal-degenerate dual pump PSA used in the experiment [11], [12]. The coherent incident light waves, which consist of two pumps and one signal, are here generated based on external modulation and then are coupled into a PSA chip. On the chip, the input light waves are split into three paths via a 1 by 3 multimode interference (MMI) coupler. Along the upper and lower paths, there are two tunable Sampled-Grating Distributed-Bragg-Reflector (SG-DBR) lasers [19], each of which is injection locked by opposite modulation side-band pumps. Therefore, each SG-DBR laser selectively amplifies the corresponding pump and suppresses the other one as well as the signal. Signal suppression due to injection locking is necessary to avoid on-chip signal-interference-induced signal power change which otherwise could be misinterpreted as the result of PSA. After further being amplified by a downstream SOA, the pump is filtered by an asymmetric Mach-Zehnder interferometer (AMZI) to remove the residual signal and the noise falling in the signal's spectrum, which avoids signal interference among three paths and enables the signal to be shot-noise limited.

Along the middle path, there is a phase tuner to phase shift the signal based on carrier plasma effects; therefore, the adjustable and stable phase relationship among the signal and two pumps can be achieved for observing the PSA-based signal power variation as a function of the signal's phase. Please note that, although there are two pumps along the middle path, their powers are much smaller than those along the other two paths so that the pump waves along the middle
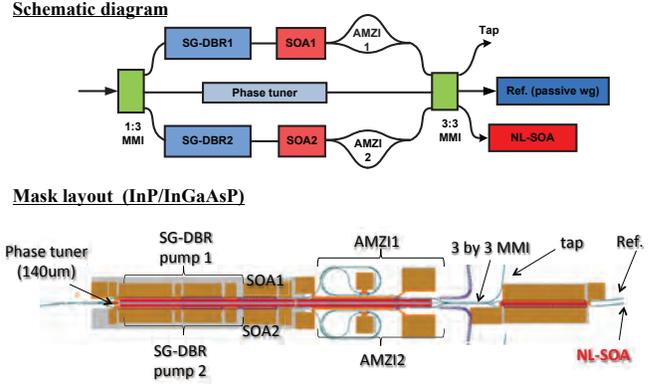
Fig. 4. Schematic of the signal-degenerate dual-pumped PSA and mask layout.

path and the pump wave interference are negligible. The light waves along three paths are combined together and split again by a 3-by-3 MMI coupler to a nonlinear-SOA (NL-SOA) where phase-sensitive amplification occurs, a long passive waveguide (WG) as a reference port, and a tap to monitor the input light waves to the NL-SOA.

In the experiment, the total input power to the NL-SOA was about -1dBm, which was high enough to saturate the NL-SOA because the NL-SOA started saturation at -9dBm input power. Once the SOA was saturated, the spontaneous emission noise and PIA were suppressed. The injection current to the NL-SOA was set to be 90 mA.

To specifically demonstrate and evaluate the PSA, the measured signal power at the output of the SOA with respect to the square root of the phase tuner current was measured, which is shown in Fig. 5. The abscissa variable is set to be the square root of the phase tuner current because the signal power after PSA varies with the signal phase, which is known to vary linearly with the square root of the phase tuner current. For comparison, the signal power without injection locking and the relative phase change of the signal were measured, which are shown in Fig. 5 as well. The relative phase of the signal was obtained by using a vector network analyzer to compare the phase of the beat note between the signal and one sideband and the phase of the RF signal applied to the external intensity modulator. The beat note was generated by heterodyning the signal and only one pump wave at the output of the tap port at a photodetector. The other pump wave was suppressed by turning off the corresponding SG-DBR laser.

As can be seen from 5, when injection locking was inactive and two lasers were in free-running modes, there was no PSA due to random phase drifting among the pumps and the signal waves. Once the injection locking was enabled, however, there was no obvious PSA or phase change of the signal until after the current was larger than 1 mA. Such a delay in phase shift commonly occurs in tunable SG-DBR lasers and could be caused by an N+ sheet charge that exists at the regrowth interface due to surface contamination. As the current was further increased, these traps are filled and phase-dependent signal gain appeared. Overall, one square root of the current gives one π phase shift to the signal and one period oscillation
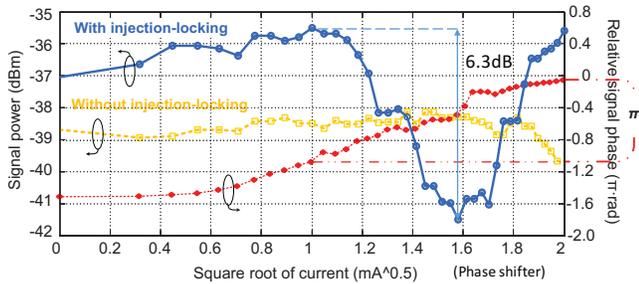
Fig. 5. Measured relationship among the signal power, the signal phase and the square root of the current applied to the phase tuner (see refs. [12], [12]).

to the signal. Clearly, such a signal power oscillation over one π instead of 2π phase indicates that the signal power change was caused by the PSA instead of the signal interference. The measured signal power curve shows that approximate 6.3 dB extinction of phase-sensitive on-chip gain was achieved. This value is in full agreement with the results of the coupled-mode model shown in Fig. 3. The linear gain that the model predicts for the simulated device is about 60dB, which is also consistent with the measured value of about 50dB [12], where the 10dB difference can be attributed to gain compression induced by ASE and to thermal effects within the waveguide. The values of g_0 and of the coefficients A, B and C has been chosen as the typical parameters for the InP/InGaAsP MQW active region of the SOA used in the experiment [6]. These values have been shown to reproduce the measured static gain-current characteristic of the NL-SOA under test.

V. CONCLUSIONS

To conclude, we derived a couple-mode model for multi-wave mixing in SOAs characterized by arbitrary functional dependencies of the recombination rate and material gain on carrier density. The model takes into account the frequency dependence of the material gain, as well as all orders of the waveguide dispersion, and accommodates input fields consisting of arbitrary combinations of multiple frequency components. We showed that the conventional approach assuming a limited number of generated four-wave mixing components gives inaccurate results when two waveforms of similar intensities are injected into the SOA. In this case, our model gives highly accurate results if a sufficient number of generated components are taken into account, as we showed by direct comparison with full time-domain simulations. We applied the coupled-mode model to studying the operation of a recently demonstrated dual-pumped PSA based on an integrated QW SOA [11], and showed that the outcome of the model is consistent with the experimental results.

City Planning through Information and Communication Technologies (INCIPICT).

REFERENCES

[1] M. J. Connelly, "Wide-Band Steady-State Numerical Model and Parameter Extraction of a Tensile-Strained Bulk Semiconductor Optical Amplifier," *IEEE J. Quantum Electron.*, vol.43, pp. 47–56, 2007.

[2] A. R. Totović, J. V. Crnjanski, M. M. Krstić, and D. M. Gvozdić, "Numerical study of the small-signal modulation bandwidth of reflective and traveling-wave SOAs," DOI 10.1109/JLT.2015.2412252, J. Lightwave Technol.

[3] G. P. Agrawal, "Population pulsations and nondegenerate four-wave mixing in semiconductor lasers and amplifiers," *J. Opt. Soc. Amer. B*, vol. 5, pp. 147–159, Jan. 1988.

[4] A. Mecozzi, "Analytical theory of four-wave mixing in semiconductor amplifiers," *Opt. Lett.*, vol. 19, pp. 892–894, June 15, 1994.

[5] A. Mecozzi and J. Mørk, "Saturation induced by picosecond pulses in semiconductor optical amplifiers," *J. Opt. Soc. Amer. B*, vol. 14, pp. 761–770, Apr. 1997.

[6] L. A. Coldren, S. W. Corzine, and M. L. Mašanović, "Diode Lasers and Photonic Integrated Circuits," 2-nd ed., Chapters 2 and 4, Wiley series in microwave and optical engineering, Hoboken, New Jersey, 2012.

[7] P. P. Baveja, D. N. Maywar, and G. P. Agrawal, "Interband Four-Wave Mixing in Semiconductor Optical Amplifiers With ASE-Enhanced Gain Recovery," *IEEE J. Sel. Topics Quantum Electron.*, vol. 18, pp. 899–908, Mar./Apr. 2012.

[8] M. A. Summerfield and R. S. Tucker, "Frequency-Domain Model of Multiwave Mixing in Bulk Semiconductor Optical Amplifiers," *IEEE J. Sel. Topics Quantum Electron.*, vol. 5, pp. 839–850, May/June 1999.

[9] P. Frascella, S. Sygletos, F. C. Garcia Gunning, R. Weerasuriya, L. Grner-Nielsen, R. Phelan, J. O'Gorman, and A. D. Ellis, "DPSK Signal Regeneration With a Dual-Pump Nondegenerate Phase-Sensitive Amplifier," *IEEE Photon. Technol. Lett.*, vol. 23, pp. 516–518, April 2011.

[10] A. D. Ellis and S. Sygletos, "Phase Sensitive Signal Processing using Semiconductor Optical Amplifiers," in *Optical Fiber Communication Conference/National Fiber Optic Engineers Conference 2013*, OSA Technical Digest (online) (Optical Society of America, 2013), paper OW4C.1.

[11] W. Li, M. Lu, L. Johansson, M. L. Mašanović, D. Dadic, S. Arafin, and L. Coldren, "First Demonstration of an Integrated Photonic Phase-Sensitive Amplifier," in CLEO: 2015, OSA Technical Digest (online) (Optical Society of America, 2015), paper SW4N.5.

[12] L.A. Coldren, W. Li, A. Mecozzi, M. Lu, S. Arafin, M. Vasilyev, D. Dadic, and L. Johansson, "Single-chip dual-pumped SOA-based phase-sensitive amplifier at 1550nm," in Summer Topicals Meeting Series (SUM) 2015, pp.88–89, 13-15 July 2015.

[13] Jyh-Tsung Hsieh, Pei-Miin Gong, San-Liang Lee, and Jingshown Wu, "Improved Dynamic Characteristics on Four-Wave Mixing Wavelength Conversion in Light-Holding SOAs," *IEEE J. Sel. Topics Quantum Electron.*, vol. 10, pp. 1187–1196, Sept./Oct. 2004.

[14] A. Mecozzi and J. Mørk, "Saturation Effects in Nondegenerate Four-Wave Mixing Between Short Optical Pulses in Semiconductor Laser Amplifiers," *IEEE J. Sel. Topics Quantum Electron.*, vol. 3, pp. 1190–1207, Oct. 1997.

[15] L. A. Coldren, S. W. Corzine, and M. L. Mašanović, "Diode Lasers and Photonic Integrated Circuits," 2-nd ed., Chapter 5, page 257, Wiley series in microwave and optical engineering, Hoboken, New Jersey, 2012.

[16] A. Böttcher and S. M. Grudsky, *Toeplitz Matrices, Asymptotic Linear Algebra, and Functional Analysis,* Birkhäuser, Basel (2012), ISBN 978-3-0348-8395-5.

[17] J. W. D. Chi, L. Chao, and M. K. Rao, "Time-Domain Large-Signal Investigation on Nonlinear Interactions Between An Optical Pulse and Semiconductor Waveguides," *IEEE J. Quantum Electron.*, vol. 37, pp. 1329–1336, 2001.

[18] W. Yang, T. Cao, Y. Yu, L. Shi, X. Zhang, and D. Huang, "Theoretical Analysis and Experimental Investigation of Degenerate Phase Sensitive Amplification in a Semiconductor Optical Amplifier," *J. Lightwave Technol.*, early access, doi: 10.1109/JLT.2015.2461572, available at http://ieeexplore.ieee.org/stamp/stamp.jsp?tp=&arnumber=7169493.

[19] L. A. Coldren, G. A. Fish, Y. Akulova, J. S. Barton, L. Johansson, and C.W. Coldren, "Tunable semiconductor Lasers: A Tutorial," *J. Lightwave Technol.* vol. 22, pp. 193–202, Jan. 2004.

First Monolithically Integrated Dual-Pumped Phase-Sensitive Amplifier Chip Based on a Saturated Semiconductor Optical Amplifier

Wangzhe Li,*Member, IEEE,* Mingzhi Lu, Antonio Mecozzi,*Fellow, IEEE*, Michael Vasilyev,*Senior Member*,*IEEE*, Shamsul Arafin, *Member, IEEE*, Danilo Dadic,Leif A. Johansson,*Member, IEEE*, and Larry A. Coldren, *Fellow, IEEE*

(*Invited Paper*)

Abstract—**For the first time, a monolithically integrated photonic phase-sensitive amplification chip is fabricated and demonstrated based on an InP/InGaAsP platform. Different semiconductor optical amplifiers have been fabricated as well for characterization. On the chip, two tunable laser pumps that are coherently injection-locked, respectively, from two first-order sidebands of an externally modulated tone are generated to enable signal-degenerate dual-pumped phase-sensitive amplification in a saturated semiconductor optical amplifier. Experiments on different chips are conducted to successfully demonstrate phase-sensitive amplification with approximately 6.3 dB and 7.8 dB extinction of phase-sensitive on-chip gain. Theoretical simulations are performed and agree well with experimental results. The additive noise properties of the phase-sensitive amplification chip are also investigated.**

Index Terms—**Phase sensitive amplifier, semiconductor optical amplifier, photonic integrated circuit, four-wave mixing**

I. INTRODUCTION

OPTICAL phase-sensitive amplifiers (PSAs) have been attracting increasing attention [1,2]due to unique advantages that enable them to break the 3-dB quantum limit of the noise figure (NF)[3], as well as achieve the phase regeneration to reduce phase and time jitters in optical transmission links [4-6]. Unlike a conventional phase-insensitive amplifier (PIA) such as an erbium-doped

fiber amplifier (EDFA), featuring an inherent minimum NF of 3-dB [7], a PSA is capable of amplifying only one of the two quadrature phase components in a light wave signal and attenuating the other. This unique feature makes it possible in theory to realize noise free amplification, leading to a NF of 0 dB, which can find numerous applications where noise levels are critical, such as optical telecommunication, remote sensing, optical spectroscopy, LIDAR and inter-satellite communication. Various PSAs have been demonstrated by using parametric down-conversion in $\chi^{(2)}$-based nonlinear materials[8, 9], such as periodically poled LiNbO$_3$ (PPLN) waveguides and nonlinear optical loop mirrors (NOLMs) [10], or using four-wave mixing (FWM) in $\chi^{(3)}$-based nonlinear media like optical fibers [2] and unsaturated semiconductor optical amplifiers (SOAs) [11]. New CMOS-compatible platforms are also emerging [12].

Among all demonstrated PSAs so far, their implementations are based on free-space bulk-crystal system or bench-top fiber systems, which makes it difficult to use them in practical scenarios. One of the challenges in realizing a practical PSA is that at input port of the PSA the phase relationship between the pump(s) and the signal must be synchronized and stabilized. Some solutions to synchronization of the pump and signal phases have been developed via pump injection locking [13] and optical phase-locked loop [14], which usually increase the complexity of the system and make it more unsuitable for use in a real application. In addition, other issues in terms of size, weight, power consumption and coupling losses also restrict the bench-top PSA's commercial allure. In order to solve this issue, photonic integration is a promising solution and can great benefit the implementation of PSAs for practical applications. Other than some obvious advantages like small footprint, light weight, reduced coupling losses and batch fabrication economies, integrated photonic chips can inherently guarantee a stable phase relationship among signal and pumps, requiring no phase-locking mechanisms, which significantly eases the implementation and practical application of PSAs.

In this paper, based on the implementation of a PSA through a dual-pump degenerate FWM process, a chip-scale PSA using a saturated SOA as a nonlinear element and different SOAs for

characterization have been fabricated and for the first time an integrated photonic PSA chip has been experimentally demonstrated. The chip and SOAs fabrication is based on an InP/InGaAsP centered quantum well (CQW) platform. On the chip, two tunable laser pumps that are coherently injection-locked from sidebands of an external modulated light wave are obtained to realize signal-degenerate dual-pumped PSA in a highly saturated SOA. A 6.3 dB and a 7.8 dB extinction ratio of gain based on different PSA chips are realized, which both agree well with simulation results. The reduction in signal-to noise ratio is also estimated based on the measured optical spectrum of the light waves before and after the PSA.

II. PROPOSED CHIP-SCALE DUAL-PUMP PSA

Figure 1 shows the schematic of the degenerate dual pump PSA. The coherent incident light waves, which consist of two pumps and one signal, are here generated based on external modulation and then are coupled into a PSA chip. On the chip, the input light waves are split into three paths via a 1 by 3 multimode interference (MMI) coupler. Along the upper and lower paths, there are two tunable Sampled-Grating Distributed-Bragg-Reflector (SG-DBR) lasers [15], each of which is injection locked by opposite modulation side-band pumps. Please note that during external modulation the signal which is carrier would be intentionally suppressed by properly biasing the modulator so that the pumps have enough power to injection lock the two SG-DBR lasers. After being injection-locked, each SG-DBR laser which selectively amplifies the corresponding pump and suppresses the other one as well as the signal behaves as a pump laser. The signal suppression in each pump laser the due to injection locking is important because such a suppression is helpful for avoiding on-chip signal-interference-induced signal power change at the input port of the PSA, which otherwise could be misinterpreted as the result of PSA. After further being amplified by a downstream SOA, the pump is filtered by an asymmetric Mach-Zehnder interferometer (AMZI) to remove the residual signal and the noise falling in the signal's spectrum, which avoids signal interference among three paths and enables the signal to be shot-noise limited.

Along the middle path, there is a phase tuner to phase shift the signal based on carrier plasma effects; therefore, the adjustable and stable phase relationship among the signal and two pumps can be achieved for observing the PSA-based signal power variation as a function of the signal's phase. Please note that, although there are two pumps along the middle path, their powers are much smaller than those along the other two paths so that the interference of the pump waves along three paths are negligible. The light waves along three paths are combined together and split again by a 3-by-3 MMI coupler to a nonlinear-SOA (NL-SOA), a long passive waveguide (WG) as a reference port, and a tap to monitor the input light waves to the NL-SOA. The PSA occurs in the NL-SOA, and the process includes two main steps. The first step is generating new signal photons. Two pumps and a signal with a stable phase relationship are sent to a nonlinear media, in which FWM

among the light waves is able to generate new signal photos with a phase which is the sum of two pumps' phases minus the original signal phase. In the second step, interference of the generated signal with original signal modulates the amplitude of the combined electrical field of the signal. Therefore, the constructive interference amplifies the amplitude of the signal's electrical field; while the destructive interference attenuates the signal. In another word, the PSA only maximally amplifies the signal when the original signal phase is 0 or π relative to the sum of two pumps' phases (in-phase components), and maximally attenuates the signal when its phase is $\pi/2$ or $3\pi/2$ (quadrature components) to the sum of two pumps' phases. Thus, the PSA gain experiences one cycle when the phase of the incident signal goes over one π, which is different from the transmission curve of a conventional Mach–Zehnder interferometer (MZI). Such a π-periodicity of the PSA gain is important and can be used to verify the implementation of the PSA. Therefore, in our demonstration of the chip-scale PSA, the relationship between the input signal phase and the signal power after the PSA can be recoded to verify the achievement of the PSA.
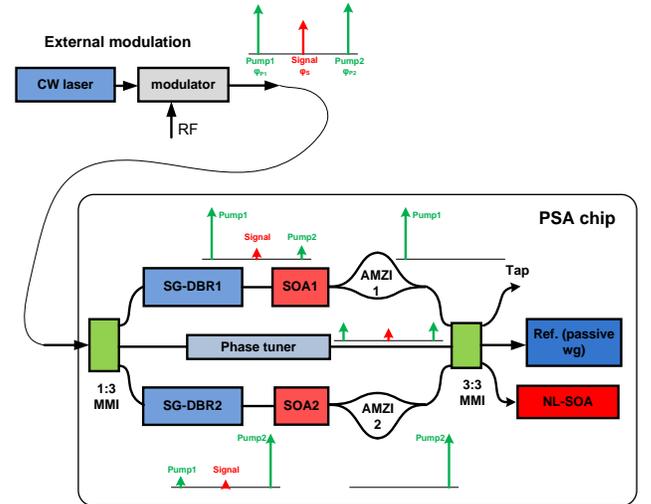
Fig. 1.Proposed schematic of demonstrating a chip scale dual-pump PSA.

One potential concern is that the SOA can be used as a PIA, and its PIA gain may interfere with the nonlinear parametric process and undermine the PSA. To overcome or minimize this issue, the incident power to the NL-SOA is high enough to saturate the NL-SOA, which is capable of suppressing the amplified spontaneous emission noise. Therefore, the saturated NL-SOA can restrict PIA and optimize the FWM [16, 17]. By recording the light wave spectrum and the signal power at the output of the NL-SOA using an optical spectrum analyzer (OSA) when changing the current applied to the phase tuner to tune the signal phase, we can evaluate the PSA performance and characterize its gain profile.

III. SOA AND PSA CHIP FABRICATION

In order to fabricate SOAs for initial characterization and monolithically integrate the single-chip dual-pumped PSA based on saturated SOA, we chose an InP/InGaAsP centered

quantum well (CQW) platform with 10 quantum wells (QWs) [18] because such a platform is capable of maximizing the mode overlap with the QWs in an SOA, enhancing the nonlinearity and maximizing the FWM.

The fabrication started with a base epi, which includes quantum well layers, waveguide layers and N-cladding layer. Active and passive areas were defined using quantum well-intermixing (QWI) technology [19]. The passive waveguide with intermixed quantum wells still confine carriers well, which is ideal for low-loss phase tuners. Then, by using electron beam lithography and methane/hydrogen/argon (MHA)-based RIE etching, the gratings of the SG-DBR laser were defined. Following the grating definition, a blanket p-cladding and p-contact layer regrowth was carried out using metalorganic chemical vapor deposition (MOCVD). After the regrowth, waveguides were defined and etched. In order to have better heat dissipation and compactness at the same time, surface ridge waveguides were used for the straight SG-DBR lasers, while more-narrow deeply-etched waveguides were used for other components on the chip, which leads to better flexibility for waveguide routing and better SOA nonlinear efficiency due to a higher confinement factor. $Cl_2/H_2/Ar$ ICP-RIE dry etching as well as InP wet etching was used to defined the features. Following the waveguide etching, P-contact vias were opened and Pt/Ti/Pt/Au was deposited as the P contact metal. To further decrease the passive waveguide loss and provide electrical isolation, we implanted protons in the p-cladding layer of the passive waveguides. The wafer was then thinned down to about 130 μm for ease of cleaving. Backside Ti/Pt/Au metallization provided common cathode connections to the n-type substrate. After cleaving and anti-reflection coating of the waveguide facets, the discrete SOAs and the PSA chips were ready for characterization. The SOAs and the chip-scale PSA were fabricated on the same wafer so that the specifications of the SOAs would be identical to those of the SOAs in the PSA chip. The length and width of the PSA chip are about 1 mm and 7 mm.

(a)

(b)
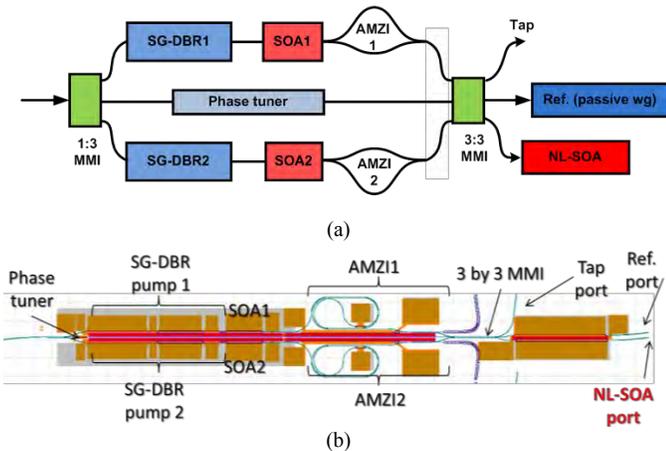
Fig. 2.(a)Schematic diagram of the PSA chip; (b)mask layout of the PSA-chip for fabrication

IV. SOA CHARACTERIZATION

Figure 3 shows all the different SOAs we fabricated. The

longest SOAs are used to evaluate the dispersion. The high-speed SOAs which are the shortest are used to measure SOA's carrier lifetime; while the 1-mm SOAs are used to characterize their gain profile.
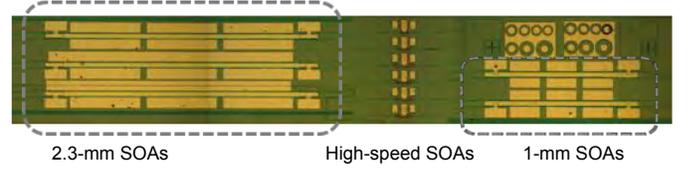
Fig. 3.Photo of the fabricated SOAs with different lengths. (left) 2.3-mm SOAs consisting of three cascaded SOAs with a length of 766 μm; (middle) high-speed SOAs with a length of 50, 100 and 150 μm; (right) 1-mm SOAs consisting of three identical SOAs with a length of 333μm.

A. Carrier Lifetime Measurement

High-speed short SOAs were used to measure the carrier lifetime. The setup is shown in Fig. 4, which mainly includes an external cavity laser (ECL), an erbium-doped fiber amplifier (EDFA), a variable optical attenuator (VOA), a bandpass filter (BPF), a high-speed SOA, a photodetector (PD) and an electrical spectrum analyzer (ESA). A wavelength from the ECL was sent to the SOA through the EDFA, the VOA and the BPF which were used to control the input light wave power. To measure the SOA's carrier lifetime, we first measured its frequency response. To do so, an RF signal and a bias voltage were applied to the SOA via a bias-tee to modulate the light wave that was passing through the SOA. The SOA's output was converted by the PD to re-generate the RF frequency which was recorded and measured by the ESA.
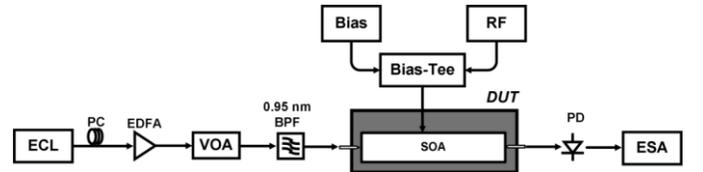
Fig. 4. SOA lifetime measurement setup

The length of the SOA under test is 50 μm, biased with a current density of 6.67 kA/cm^2. We measured SOA's frequency response given different input power, and then based on its 3-dB bandwidth, the lifetime could be calculated. We plotted the relationship between the carrier lifetime and the input power to the SOA, as shown in Fig. 5. As it can be seen, the carrier lifetime goes down to 180 μm as the input power increases to about 21 mW.
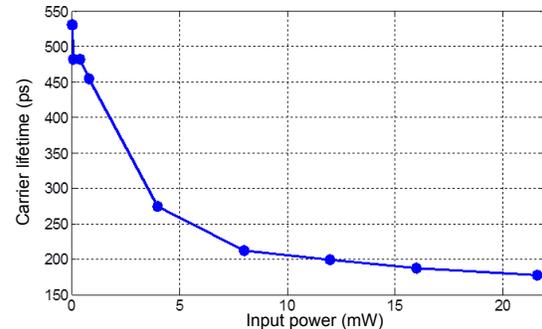
Fig. 5.Measured SOA carrier lifetime given different incident light wave power.

B. Small-Signal Gain Measurement

We took advantage of a 1-mm SOA consisting of three cascaded 333-µm SOAs to characterize its gain profile. The setup is shown in Fig. 6. Since the 1-mm SOA has three cascaded 333-µm SOAs, the first 333-µm SOA was negatively biased as a PD to measure the input power; then it was forward-biased as an amplifier to amplify the input light wave. The second 333-µm SOA was reverse-biased to detect the amplified light wave power at the output of the first 333-µm SOA.
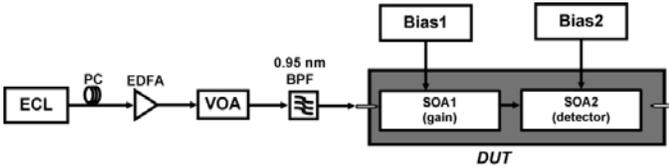
Fig. 6. SOA gain measurement setup
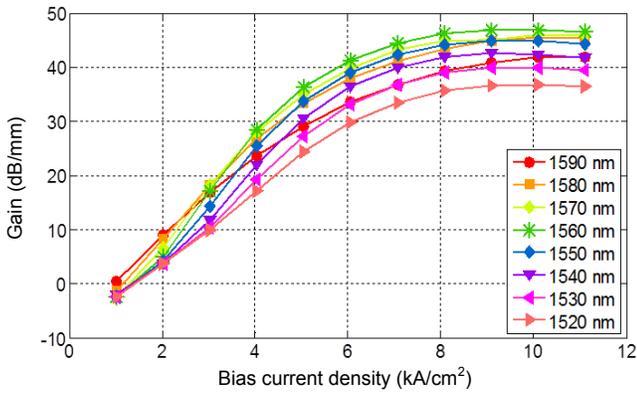
Fig. 7. Measured linear gain of a 1-mm SOA;

Comparing the measured input power and the power after amplification, we can obtain the gain for a 333-µm SOA. Changing the forward bias current and the input wavelength, and tripling the calculated gain, we can collect gain profiles of the 1-mm SOA, which are shown in Fig. 7. Fig. 7 shows the relationships between small-signal gain of the SOA and current density given different input wavelengths. We can see that the small-signal gain goes up as we increase the current density and becomes saturated after the current density is higher than 8 kA/cm^2. The transparent current density, given different wavelengths, is varied in the range between 1 kA/cm^2 and 1.5 kA/cm^2. Fig. 8 shows the relationship between the maximum small-signal gain and the incident wavelength when the current density is fixed. As we can see from Fig. 8, the peak small-signal gain was measured to be about 47.5 dB/mm at a wavelength of 1560 nm and a current density of 9 kA/cm^2. For the PSA experiment, we will choose a proper incident wavelength to optimize the gain of the SOAs for the operation of the PSA chip.

Because the PSA-chip is based on a saturated SOA, we need to find out the input power level to saturate the SOA. Since the length of the NL-SOA on the PSA chip is 1 mm, then we treated the 1-mm cascaded SOA as a single SOA, and we applied a current density of about 3 kA/cm^2 and measured its output power as we increased the input power. The result is plotted in

Fig. 9, showing that the 1-mm SOA would be saturated when the input power reaches about -9 dBm. Based on this input power level, we chose an incident power of 0 dB or higher to the NL-SOA on the PSA chip to ensure that the NL-SOA was deeply saturated.
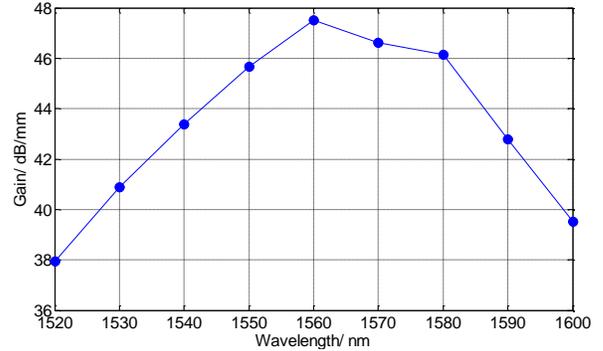
Fig. 8. Measured wavelength-dependent small-signal gain profile
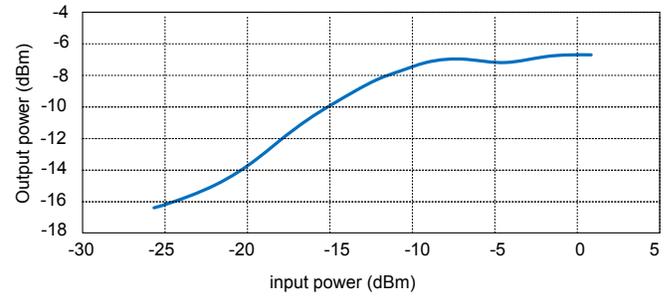
Fig. 9. Measured output power of the SOA with respect to the input power

C. Dispersion Measurement

In the implementation of the PSA based on a long single mode fiber or a high nonlinearity fiber, the fiber dispersion can play an important role in the PSA effect, reducing the PSA gain or gain bandwidth. Similarly, for operating the PSA chip, we have to find out the dispersion characteristics of a saturated SOA. A method to measure the dispersion has been proposed.
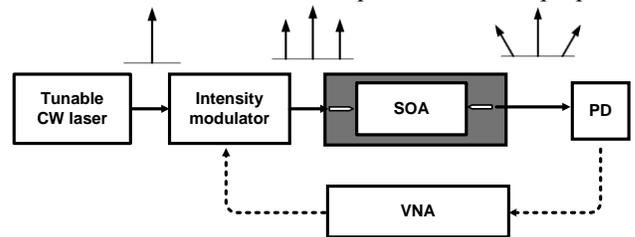
Fig. 10. SOA dispersion measurement setup

The setup shown in Fig. 10 consists of a tunable laser source, an intensity modulator (IM), a PD and a vector network analyzer (VNA). The light wave from the laser was external modulated through the IM by an RF signal applied to the IM. The RF signal was generated from the VNA. Due to the small-signal modulation, the light wave would have two more sidebands; and after passing through the SOA, nonlinear phase changes were applied to the sidebands and the original carrier due to the dispersion of the SOA. The sidebands and the carrier were sent to the PD to re-generate the RF signal which was recorded by the VNA. Then the nonlinear phase changes

35

introduced by the dispersion could be recovered by the comparing the RF phase changes. When we swept the input wavelength and recorded the corresponding nonlinear phase changes or the RF phase differences, we could calculate the dispersion of the SOA.
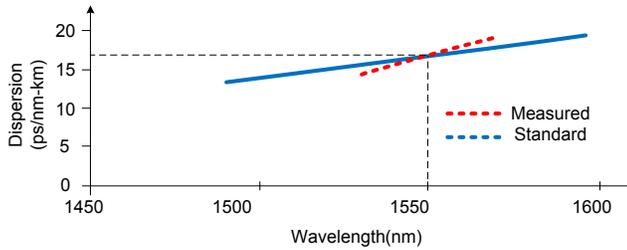
Fig. 11.Comparison of the measured dispersion of a 2-meter SMF and its standard dispersion value.

Before measuring the dispersion of the SOA, we need to evaluate this setup and prove it is functional. Therefore, we use the setup to measure the dispersion of a 2-meter signal mode fiber (SMF) and compared the result with the standard dispersion result of an ITU G.653 single mode fiber. The input wavelength was shifted from 1545 nm to 1575 nm. As we can see from Fig. 11, at 1550 nm, the measured result agrees well with the standard dispersion value; The dispersion slot is different, which could be caused by the facts that the standard SMF dispersion is based on a few km meter fiber (averaging thousands of different 2-meter SMFs) and the input wavelength was not stable and drifting during the experiment.
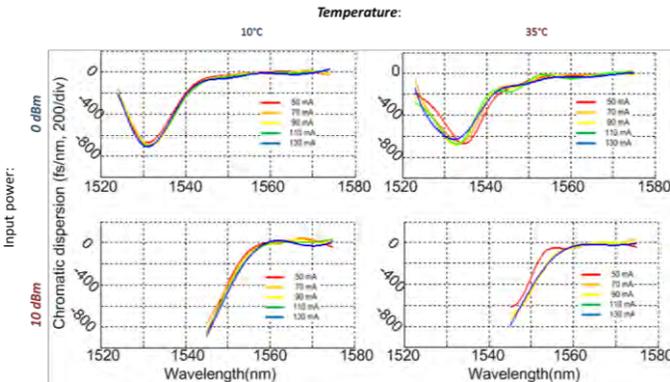
Fig. 12 Measured SOA dispersion curves given different temperatures and input powers.

After proving that the setup in Fig. 10 is functional, we measured the dispersion of a 2.3-mm SOA given different temperature and input power. The input power was set to be 0 dBm and 10 dBm, which are high enough to saturate the SOA. Please note that before each measurement, we removed the SOA first and measured the background dispersion including the modulator and the 16-meter fiber in the setup.

The measured dispersion is shown in Fig. 12, as we can see, dispersion curves are not flat. When temperature was fixed at 0 degree Celsius, given a 0-dBm input power, the dispersion is flat and close to 0 fs/nm when the wavelength falls in a range between 1550 nm to 1570 nm. At a shorter wavelength range

between 1525 nm to 1545 nm, there is a dispersion notch, and the saturated SOA shows a relatively large dispersion of -700 fs/nm, or -304 fs/nm/mm at a wavelength of 1530 nm. When the input power was increased to 10 dBm to further saturate the SOA, the measurement can only covers a wavelength range from 1545 nm to 1575 nm because of the limited gain bandwidth of the EDFA we used in the experiment; however, thanks to the appearance of the right edge of the notch, we can still tell that the dispersion curves are red-shifted. Then we increased the temperature to 35 degree Celsius, we repeated the measurement and found out that the dispersion characteristics stayed the same.

The measurement still has a few issues. The wavelength instability caused dispersion ripples on the curves; large background dispersion introduced by the 16-meter long fiber in the setup made it difficult to accurately measure the small amount of dispersion.

For the future PSA experiment and simulation, we chose the incident wavelength around 1560 nm and treated the SOA as dispersion-free element.

V. PSA CHIP CHARACTERIZATION

(a)

(b)
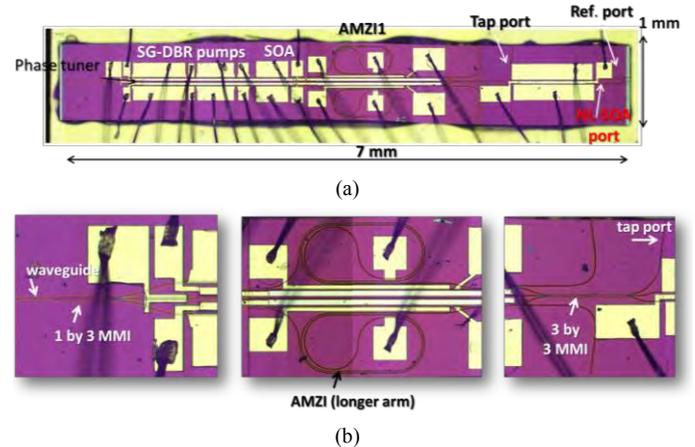
Fig. 13.(a) Photo of the signal-degenerate dual-pumped PSA chip after wire-bonding; (b) close-up views of some sections of the chip.

Fig. 13 shows a microscope picture of the fabricated PSA chip after being wire-bonded and a close-up view of some sections of the chip. We can clearly see the metal contacts which are the large golden squares, the thin waveguide at the input port of the 1 by 3 MMI, the long and curled waveguide as one arm of the AMZI, and the 3 by 3 MMI before the input of the NL-SOA and tap waveguide.

Before conducting the PSA experiment, we need to characterize the chip to choose the best chips. Specifically, we evaluated the performance of the SG-DBR lasers, the injection locking of the two SG-DBR lasers and the spurious signal interference among three paths.

A. SG-DBR Lasers

First of all, the two SG-DBR lasers were pumped and light-current-voltage (LIV) curves were measured. A typical measured LIV curve is shown in Fig. 14. The green curve is the measured laser output power as we increased the pump current.

The kink on the curve represents a mode-hopping which was caused by the internal temperate and refractive index change as we changed the current. As we can see, the SG-DBR laser has a threshold of about 30 mA at a temperature of 20 degree Celsius, and a maximum output power of about 18 dBm at a bias current of 120 mA. However, when both SG-DBR lasers were turned on, the maximum output of each one was only about 12 dBm or less due to heating effect.
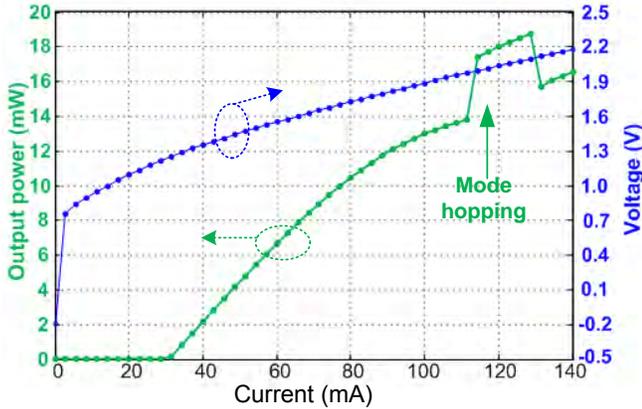
Fig. 14. Measured LIV curve of a SG-DBR laser.
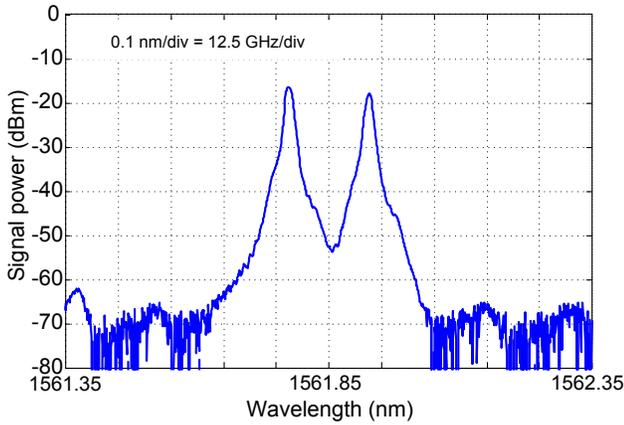
Fig. 15. Measured optical spectrum of the output of two free-running SG-DBR lasers.

The outputs of two SG-DBR lasers were measured as well using an optical spectrum analyzer (OSA, with a resolution of 0.01 nm) and shown in Fig. 15. The two wavelengths are spacing around 0.15 nm, which is equivalently 18.7 GHz. We can easily tune the wavelengths by changing the current applied to the corresponding phase section in each SG-DBG laser. The averaged tuning rate is about 1.18 GHz/mA. However, due to heating effect, tuning one wavelength always changed the other one in the experiment.

B. Injection Locking of Two SG-DBR Lasers

Because injection locking two SG-DBR lasers is important to make sure that the two pumps and the signal sent to the NL-SOA to have the stable phase relationship, we have to evaluate the injection locking performance of each laser.

We simply used an external laser to send the light wave to the chip and turned on only one SG-DBR laser. Then at the tap

port, we used an OSA to monitor two wavelengths and started to align them with each other. Once they were close enough, we coupled the output of the tap to an external PD to convert the light waves to an electrical beat note which was analyzed by an ESA and we observed an unstable peak due to the random phase relationship between two wavelengths. When the spacing between two wavelengths became closer and closer, we observed that the central frequency of the beat decreased. Once the two wavelengths were close enough, the beat signal disappeared and only a flat noise floor appeared on the ESA which indicated that the SG-DBR laser was injection locked and its wavelength was as same as the external one. By shifting the wavelength of the sideband through changing the frequency of the modulation RF signal, and the incident sideband power, we measured the injection locking range with respect to different injection ratio. The injection ratio is the power ratio of the incident sideband power to the laser output. Then we turned off the laser, turned on the other and repeated the same measurement. The results are plotted in Fig. 16. As we can see that the maximum locking ranges are about 4.5 GHz and 3.8 GHz when the injection ratio is maximized in the experiment. However, for the PSA experiment, both SG-DBR lasers must be injection-locked, the total input power from external modulation was distributed on two sidebands (the signal power can be ignored), which reduced the injection ratio by 3 dB. Therefore, only 3 GHz and 2.2 GHz injection locking ranges can be achieved. Considering the laser wavelength shifting due to cross heating effect when we changed the phase tuner current, the real locking range for each laser would be smaller.
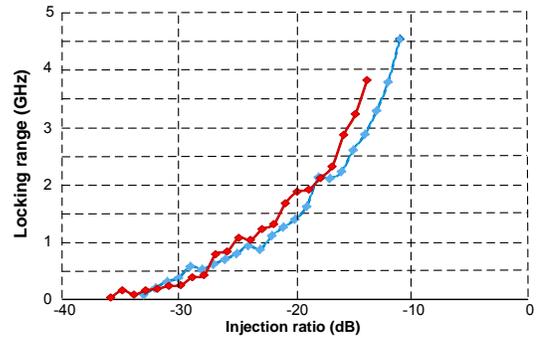
Fig. 16. Measured injection locking ranges of two SG-DBR lasers given different injection ratios.
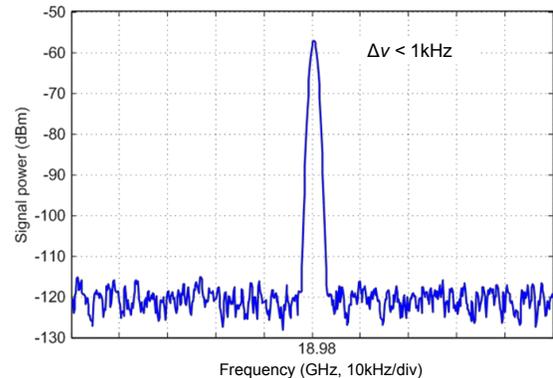
Fig. 17. Measured electrical spectrum of the beat by heterodyning the wavelengths from two injection-locked SG-DBR lasers.

37

Once two SG-DBR lasers were both injection- locked by the two pumps from external modulation, the beat note of two wavelengths at a PD becomes a very stable and narrow line and can be monitored by the ESA, as shown in Fig. 17. The resolution bandwidth of the ESA was about 100 Hz. The 3-dB bandwidth of the beat is less than 1 kHz, which means that once two SG-DBR lasers are injection locked, their relative frequency spacing is fixed and determined by the two pumps and their relative linewidth is also less than 1 kHz. Thus, once we obverse a stable peak with a frequency of twice the RF modulation frequency at the ESA, we can claim that the two SG-DBR lasers are injection-locked. During the PSA experiment we conducted, we always used the ESA to monitor the beat note of two SG-DBR lasers through the tap port to make ensure the injection locking was enabled.

C. Spurious Signal Interference

As we mentioned before, another advantage of injection locking is the suppression of the signal, which ensures that signal passes through the upper and middle paths, causing signal interference and leading to possible misinterpreted PSA effect. Therefore, after two SG-DBR lasers were injection-locked and before we started to evaluate the PSA by recording the signal power at the output of the NL-SOA, we have to first rule out the possibility of the signal interference among three paths to avoid improper interpretation of the PSA when shifting the signal phase by change the phase tuner current. Thus, at the output of the tap port, the signal power with respect to time and phase tuner current were measured and compared, as shown in Fig. 18. The blue solid curve is the measured signal power as we increased phase tuner current; while the dotted red curve is the measured signal power over time. By comparing two curves here, only similar random power fluctuations of about ± 0.5 dB were observed in two cases and no obvious interference among three paths was observed.

In addition, the power of the SG-DBR pump waves along the upper and the lower paths were about 15 dB higher than those along the middle path, therefore, the pump interference which could cause PSA gain drift can be ignored as well, and the signal power change at the output of the NL-SOA would be only caused by the PSA.
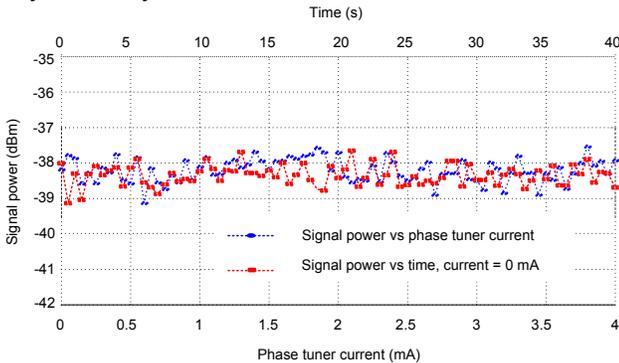
Fig. 18.Measured signal power at the output of the tap with and without phase tuner current changing.

D. Phase Tuner Characterization and Phase Shift Measurement

Tuning the phase of the signal is important for the PSA experiment. And knowing the exact phase shift when we tune the current applied to the phase tuner is more important because we need to take advantage of π-periodicity of the PSA gain curve to verify the PSA. To obtain relative phase change of the signal, we used the setup shown in Fig. 19.
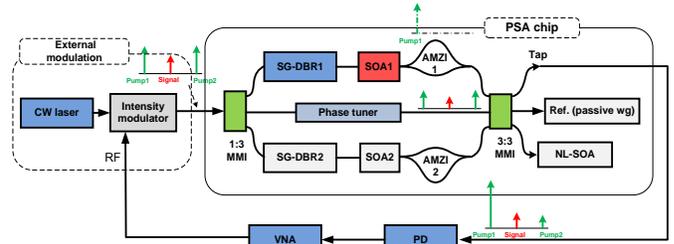
Fig. 19.Relative signal phase measurement setup.

The RF signal for the external modulation was from the VNA. One SG-DBR laser was turned off so that only one SG-DBR laser was injection locked and only one sideband was selectively amplified. Please note that the power of the amplified sideband was much larger than those of sidebands along the middle path so that the later were ignored. The signal and the amplified sideband at the output of the tap were sent to the PD to re-generate the RF signal whose phase change would be identical to that of the optical signal. Therefore, by using the VNA to measure the phase change of the received the RF signal when changing the phase tuner current, we were able to equivalently get the relative phase change of the optical signal. The result is shown in Fig. 20. The abscissa variable is set to be the square root of the phase tuner current because the signal phase in theory varies linearly with the square root of the phase tuner current. As we can see, there was no obvious phase change of the signal until after the current was larger than 1 mA. Such a delay in phase shift commonly occurs in tunable SG-DBR lasers and could be caused by an N+ sheet charge that exists at the regrowth interface due to surface contamination. As the current was further increased, these traps are filled and phase shift appeared. Overall, 1 mA$^{0.5}$ gives π phase shift of the signal.
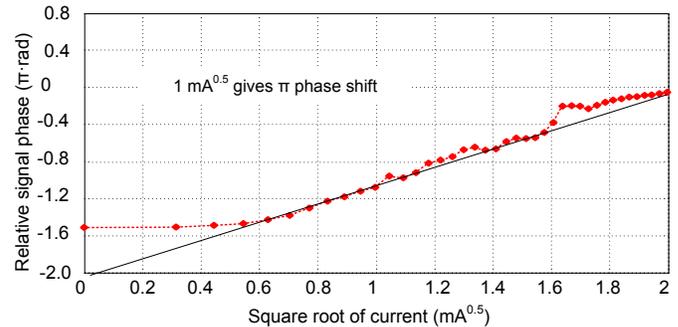
Fig. 20.Measured relative signal phase change.

To help evaluate the signal phase measurement, we also formed an on-chip MZI by deactivating the lower path. Without

38

external modulation, we sent one wavelength to the chip and injection locking one SG-DBR laser and measured the output power at the tap when we were changing the phase tuner current. The on-chip MZI is depicted in Fig. 21. It is well-known that the output power of the MZI varies sinusoidally with the phase difference of the light waves along two arms, and features a 2π-periodicity. Therefore, we can estimate the current-induced phase shift of the signal by observing the MZI output as we change the phase tuner current.
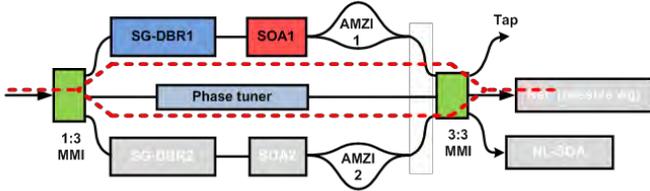
Fig. 21. On-chip MZI setup

The measured MZI output is shown in Fig. 22. As we can see, the output power barely changes when the current is less than 1 mA due to the phase delay. As the current increase, the signal power experiences one cycle. It can be clearly seen that approximately 1.1 $\text{mA}^{0.5}$ gives one π phase shift, which agrees well with the result obtained based on previous method (1 $\text{mA}^{0.5}$ gives π phase shift).
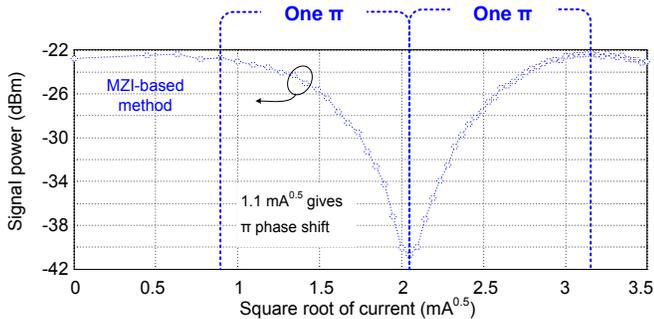
Fig. 22. Measured MZI output when changing the phase tuner current

VI. PSA EXPERIMENTAL RESULTS AND DISCUSSION

Once the basic chip characterizations were completed and the best chips were chosen, we started to configure the chip and the external modulation setup to start the PSA experiment. For external modulation, two pumps spacing about 18 GHz and one signal were generated by using an external tunable laser and an IM as in Fig. 1. The IM was properly biased to suppress the signal power, which made the sidebands' power dominant and facilitated the injection locking. The incident light waves were coupled into the PSA chip via a tapered fiber with a total coupling loss of about 6 dB. The pump power coupled into the SG-DBR laser was about -3 dBm and the output power of each laser is about 11 dBm, giving an injection ratio of about -14 dB and an injection locking ranges of 3 GHz and 2.2 GHz for two lasers, respectively. The current applied to the gain section of each SG-DBR laser fell in a range between 80 mA and 100 mA. The current to each SOA following corresponding laser lied in a range between 70 mA and 90 mA. By finely tuning the free running wavelengths of two SG-DBR lasers, the wavelength of

the external laser and the RF modulation frequency, two SG-DBR lasers could be injection locked by the two pumps. During the measurements, the wavelength of the incident signal was tuned to lie in a range between 1560 nm and 1562 nm, and the frequency of the RF signal was set to be about 9 GHz. Then the pumps and the signal were sent to the NL-SOA with a current of about 90 mA. The total input power to the NL-SOA was about -1 dBm, which was high enough to saturate the NL-SOA because the NL-SOA started saturation at -9 dBm. Once the SOA was saturated, the spontaneous emission noise and PIA were suppressed. The output of the NL-SOA was sent to the optical spectrum analyzer for recording the power of the signal as its phase was changed for PSA demonstration. The input saturation power was -9dBm. (The PIA gain is much smaller with input powers approaching the input saturation power.)

(a)

(b)
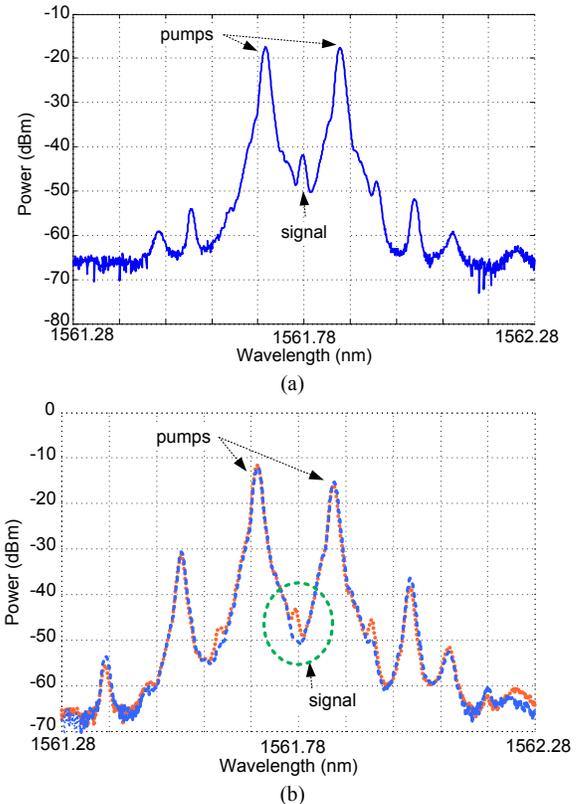
Fig. 23. Measured optical spectrum of the light wave at (a) the input and (b) the output of the NL-SOA.

The optical spectra at the input and the output of the NL-SOA were measured to record the signal power change caused by the PSA. The optical spectrum of the input light waves was equivalently obtained by monitoring the output of the tap port by using the optical spectrum analyzer. The measured optical spectra are shown in Fig. 23. Fig. 23 (a) is the optical spectrum of the input light waves. As we can see, there are two dominant pumps and one suppressed signal in the middle. Other small peaks are high-order sidebands from external modulation. Fig. 23(b) is the optical spectrum of the light wave after the PSA when the signal phase was changed by tuning the phase tuner current. Comparing with Fig. 23(a), we can clearly see the FWM and the idler waves outside the two pumps. In addition, we can see that the signal was amplified or attenuated as the

phase tuner current was adjusted. Such a current- or phase-dependent signal power change could be caused by the PSA.

To specifically demonstrate and evaluate the PSA, the measured signal power at the output of the SOA with respect to the square root of the phase tuner current was measured, which is shown in Fig. 24. Again, the abscissa variable is set to be the square root of the phase tuner current because the signal power after PSA varies with the signal phase, which is known to vary linearly with the square root of the phase tuner current. For comparison, the measured signal power without injection locking and the measured relative phase change are shown in Fig. 24 as well. As can be seen from Fig. 24, when injection locking was inactive and two lasers were in free-running modes, there was no PSA due to random phase drifting among the pumps and the signal waves. Once the injection locking was enabled, however, there was no obvious PSA or phase change of the signal until after the current was larger than 1 mA, which is caused by the phase delay we mentioned before. As the current was further increased, these traps are filled and phase-dependent signal gain appeared. Overall, 1 mA$^{0.5}$ gives π phase shift of the signal and one period oscillation of the signal. Clearly, such a signal power oscillation over one π instead of 2π phase indicates that the signal power change was caused by the PSA instead of the signal interference. The measured signal power curve shows that approximate 6.3 dB extinction of phase-sensitive on-chip gain was achieved.
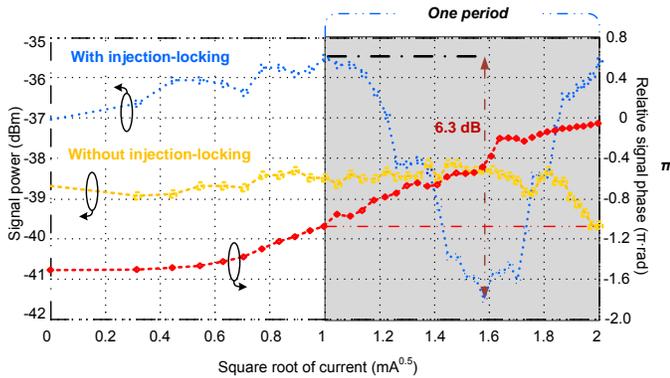
Fig. 24. Measured relationship among the signal power, the signal phase and the square root of the current applied to the phase tuner.
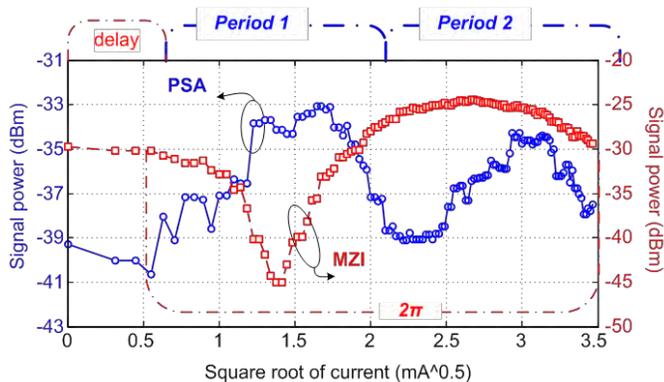
Fig. 25. Measured signal power at the output of the NL-SOA when the chip is configured as a PSA chip and the signal power at the output of the tap when the chip is configured as an MZI.

To demonstrate multiple periods of a PSA gain curve, we chose another PSA chip and repeated the same procedures but increased the phase tuner current. The results are shown in Fig. 25. The blue curve is the measured signal power change at the output of the NL-SOA caused by the PSA; while the red curve is the measured signal power at the output of the on-chip MZI. The blue curve shows a PSA gain curve of two periods, and the red curve indicates that approximately, 1.5 mA$^{0.5}$ gives one π phase shift. Amplitude reduction of the second period was probably caused by the power reduction of the input pumps as the phase tuner current was increased.
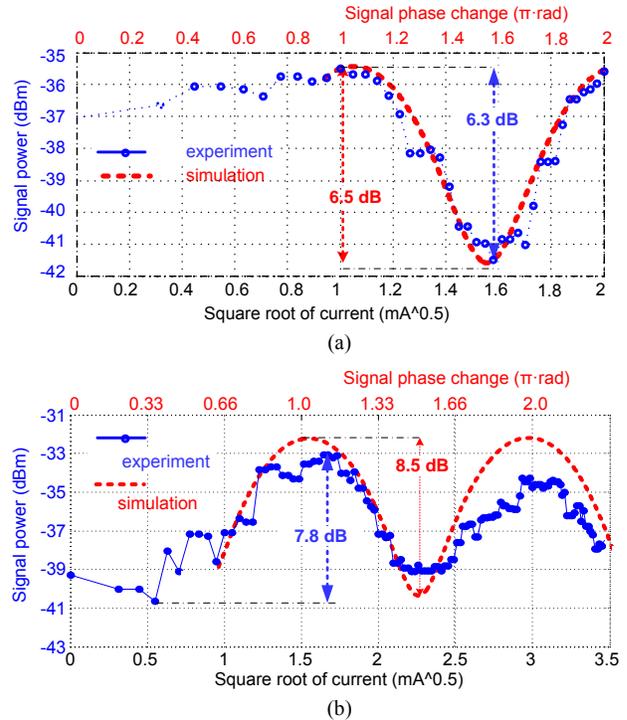
Fig. 26. Comparisons of the measured PSA gain curve and the theoretical simulation. (a) one-period PSA gain curve with 6.3 dB experimental and 6.5 dB theoretical results; (b) two-period PSA gain curve with 7.8 dB experimental and 8.5 dB theoretical results.

A theoretical simulation of the PSA gain based on coupled differential equations [17] and the model provided by Prof. Mecozzi is presented in Fig. 26(a), showing a 6.5 dB extinction ratio of the phase-sensitive gain, which agrees well with the experimental result over this current and phase-shift range. Simulation results for the second chip were obtained as well and presented in Fig. 26(b), showing a two-period PSA gain curve. Again, good agreement was observed.

The added noise of the PSA is another important aspect. Thus, the input and the output SNR of the PSA was estimated from the measured optical spectrum of light waves at the input and the output port of the NL-SOA. Please note that the input optical spectrum was equivalently measured at the output of the tap port. The signal level was the power at the signal wavelength. The noise level could not be easily measured at exactly the same wavelength, so it was measured at eight different wavelengths that were 0.5 nm away from the signal wavelength where the background spectrum was relatively flat, as shown in Fig. 27.
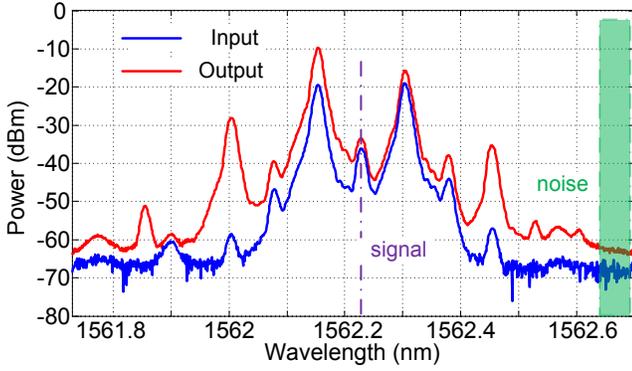
Fig. 27.The measured input and the output optical spectra of the NL-SOA.

At each wavelength, the measured SNR was obtained through 10 times iteration, as shown in Fig. 28(a), and the difference was calculated and shown in Fig. 28(b). The smallest difference in SNR was 1.5 dB and overall averaged decrease in SNR was about 2.5 dB.
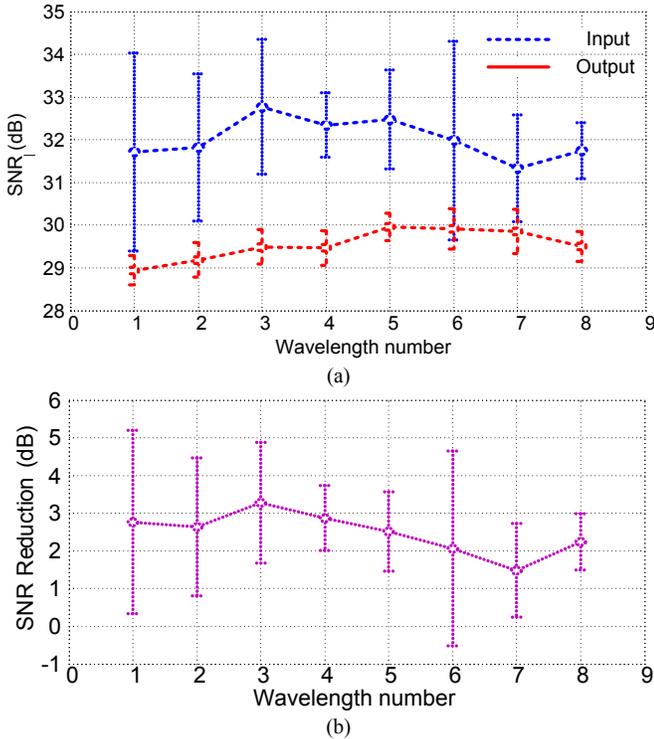
Fig. 28.(a) Measured SNR of the input and the output light waves of the NL-SOA; (b) calculated SNR reduction.

VII. CONCLUSION

Based on an InP/InGaAsP, platform we have fabricated and characterized different SOAs, and based on a highly saturated SOA, we have successfully fabricated and demonstrated the first monolithic dual-pumped PSA chip. The amplified spontaneous emission noise of the SOA was suppressed significantly due to the high saturation which restricts PIA, while high nonlinearity of the SOA benefited the PSA.

On the chip, two tunable laser pumps coherently injection-locked from sidebands of an external modulated tone were generated to enable signal-degenerate dual-pumped phase-sensitive amplification in a highly saturated semiconductor optical amplifier. Phase-sensitive amplification was experimentally achieved with approximately 6.3 dB and 7.8 dB extinction of phase-sensitive on-chip gain using two different chips. Theoretical simulations based on coupled differential equations were performed and agreed well with experimental results. The Signal-to-Noise Ratio degradation of the phase-sensitive amplification chip was also estimated, and averaged 1.5 – 3.1dB.

However, compared with high nonlinear fiber, the PSA gain is still small. The investigation of the chip-scale PSA is not comprehensive due to low current density to the NL-SOA and low incident pump power to the NL-SOA. Increasing the current density to the NL-SOA to increase the PSA gain more likely causes more heating problems, which either leads to unstable injection locking or reducing the laser pump power or possible pump interference. In addition, limited pump power to the NL-SOA restricts the saturation level of the NL-SOA, which makes it difficult to evaluate the PSA effect given a deeply saturated SOA. The PSA chip layout can be improved to allow more incident pump powers to the NL-SOA, such as using directional couplers in the PSA chip.

REFERENCES

[1] R. Slavík, F. Parmigiani, J. Kakande, C. Lundström, M. Sjödin, P. A. Andrekson, R. Weerasuriya, S. Sygletos, A. D. Ellis, L. Grüner-Nielsen, D. Jakobsen, S. Herstrøm, R. Phelan, J. O'Gorman, A. Bogris, D. Syvridis, S. Dasgupta, P. Petropoulos, and D. J. Richardson, "All-optical phase and amplitude regenerator for next-generation telecommunications systems," Nat. Photonics, vol. 4, no.10, pp. 690–695,2010.

[2] Z. Tong, C. Lundström, P. A. Andrekson, C. J. McKinstrie, M. Karlsson, D. J. Blessing, E. Tipsuwannakul, B. J. Puttnam, H. Toda, and L. Grüner-Nielsen, "Towards ultrasensitive optical links enabled by low-noise phase-sensitive amplifiers," Nat. Photonics, vol. 5, no. 7, pp. 430–436, 2011.

[3] C. M. Caves, "Quantum limits on noise in linear amplifiers," Phys. Rev. D., vol. 26, no. 8, pp. 1817-1839, 1982.

[4] Y. Mu and C. M. Savage, "Parametric amplifiers in phase-noise-limited optical communications," J. Opt.Soc. Am. B, vol. 9, no. 1, pp. 65-70, 1992.

[5] H. P. Yuen, "Reduction of quantum fluctuation and suppression of the Gordon-Hauseffect with phase-sensitive linear-amplifiers," Opt. Lett., vol. 17, no. 1, pp. 73-75, 1992.

[6] J. N. Kutz, W. L. Kath, R.-D. Li, and P. Kumar, "Long-distance propagation in nonlinear optical fibers byusing periodically spaced parametric amplifiers," Opt. Lett., vol. 18, no. 10, pp. 802-804, 1993.

[7] P. C. Becker, N. A. Olsson, and J. R. Simpson, Erbium doped fiber amplifiers: fundamentals and technology, Academic Press, San Diego, Calif., 1999.

[8] K. J. Lee, F. Parmigiani, S. Liu, J. Kakande, P. Petropoulos, K. Gallo, and D. J. Richardson, "Phase sensitive amplification based on quadratic cascading in a periodically poled lithium niobate waveguide," Opt. Express, vol. 17, no. 22, pp.20393–20400, 2009.

[9] T. Umeki, M. Asobe, and H. Takenouchi, "In-line phase sensitive amplifier based on PPLN waveguides," Opt. Express, vol. 21, no. 10, pp. 12077–12084, 2013.

[10] M. E. Marhic, C. H. Hsia, and J.-M. Jeong,"Optical amplification in a nonlinear fibre interferometer," Electron. Lett., vol. 27, no. 3, pp. 210-211, 1991.

[11] A. D. Ellis and S. Sygletos, "Phase sensitive signal processing using semiconductor optical amplifiers,"in OFC2013, paper OW4C.1

[12] D.J. Moss, R. Morandotti, A. L. Gaeta, and M. Lipson, "New CMOS-compatible platforms based on silicon nitride and Hydex for non-linear optics,' Nature Photonics, vol. 7, pp 597-607, Aug., 2013.

[13] A. Takada and W. Imajuku, "In-line optical phase-sensitive amplifier employing pump laser injection-locked to input signal light," Electron. Lett., vol. 34, no. 3, pp. 274-276,1998.

[14] W. Imajuku and A. Takada, "In-line optical phase-sensitive amplifier with pump light source controlled by optical phase-lock loop," J. Lightwave Technol., vol. 17, no. 4, pp. 637-646,1999.

[15] L. A. Coldren, G. A. Fish, Y. Akulova, J. S. Barton, L. Johansson, and C.W. Coldren, "Tunable semiconductor Lasers: A Tutorial," J. Lightwave Technol., vol. 22, no. 1, pp. 193–202,2004.

[16] A. D'Ottavi, F. Girardin, L. Graziani, F. Martelli, P. Spano, A. Mecozzi, S. Scotti, R. Dall'Ara, J. Eckner, and G. Guekos, "Four-wave mixing in semiconductor optical amplifiers: A practical tool for wavelength conversion," IEEE J. Sel. Topics Quantum Electron., vol. 3, no. 2, pp. 522-528, 1997.

[17] A. Mecozzi, "Analytical theory of four-wave mixing in semiconductor amplifiers," Opt. Lett., vol. 19, no. 12, pp. 892–894, 1994.

[18] J. Raring, M.Sysak, A. Pedretti, M. Dummer, E. Skogen, J. Barton, S. Denbaars, and L. Coldren, "Advanced integration schemes for high-functionality/high-performance photonic integrated circuits," in Proc. IEEE SPIE, San Jose, CA, Paper 6126-19, 2006.

[19] E. Skogen, J. Barton, S. Denbaars, and L. Coldren, "A quantum-well-intermixing process for wavelength-agile photonic integrated circuits," IEEE J. Sel. Top. Quantum Electron., vol. 8, no. 4, pp. 863–869, 2002.

Wangzhe Li received his PhD from the University of Ottawa, Canada, in 2013 working on the photonic generation of microwave and millimeter wave signals, and then joined the University of California, Santa Barbara, CA, as a postdoctoral scholar where he has been working on integrated optical phase-sensitive amplifiers.
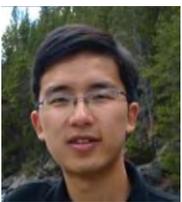
Mingzhi Lu received his B.S. degree in electrical engineering from Southeast University, Nanjing, China in 2008, and received his M.S. and Ph.D. in Electrical and Computer Engineering from the University of California, Santa Barbara, California in 2010 and 2013. After obtaining his Ph.D., he worked at UC Santa Barbara as a postdoctoral researcher between 2013 and 2014. He is currently working at Infinera Corp. as a senior PIC development engineer. His Ph.D. and postdoctoral research is mainly focused on III-V photonic integration technology, and integrated coherent optical systems, such as integrated optical phase-locked loops, coherent LIDAR, optical synthesizer and phase-sensitive amplifiers. He is currently focusing on the next-generation larger-scale photonic integrated circuits for future communication applications.

Antonio Mecozzi is a Professor and the Director of the Department of Physical and Chemical Sciences of the University of L'Aquila, Italy, Previously, he worked for 15 years in the Optical Communication Division of Fondazione Ugo Bordoni in Rome. He was a visiting scientist of the EECS Department and the Research Laboratory of Electronics of MIT from 1991 to 1992. His areas of interest include studies on soliton transmission, laser mode-locking, nonlinear propagation in fiber, polarization mode dispersion, physics and applications of semiconductor optical amplifiers, optical amplification and noise. He holds numerous patents and over 160 publications in refereed scientific journals. Prof. Mecozzi is a Fellow of the Optical Society of America and of the IEEE.

Michael Vasilyev received the M.S. degree in Physics from Moscow Institute of Physics and Technology, Russia, in 1993, and the Ph.D. degree in Electrical Engineering from Northwestern University, Evanston, IL, in 1999 for studies of quantum properties of parametric amplifiers and solitons in optical fibers. Before joining the University of Texas at Arlington (UTA) in 2003, where he is currently a Professor of Electrical Engineering, he worked at Corning Inc. in Somerset, NJ as a Senior Research Scientist, investigating noise and nonlinearities in optical fibers as well as in Raman and erbium-doped amplifiers. Prof. M. Vasilyev's interests concentrate in experimental and theoretical nonlinear and quantum optics and nanophotonics, with applications to classical and quantum information processing, ultra-sensitive measurements, and remote sensing. He has 54 journal and over 130 conference papers, as well as 10 U.S. patents, and was a recipient of 2008 DARPA Young Faculty Award. Dr. Vasilyev has served as a chair or member of technical committees for many conferences, including IEEE Summer Topicals, CLEO, OFC, Photonics West, FiO, etc., and is an associate editor for the IEEE/OSA J. of Lightwave Technology. He is a Fellow of the OSA and a Senior Member of the IEEE Photonics and Communication Societies.

Shamsul Arafin is currently working as an Assistant Project Scientist in the University of California at Santa Barbara (USCB), USA under the supervision of Prof. Larry A. Coldren. Prior to joining UCSB, he worked as a Postdoctoral Research Scholar in Device Research Laboratory at the University of California at Los Angeles, USA. He received the B.Sc. degree in Electrical and Electronics Engineering from Bangladesh University of Engineering and Technology (BUET), Bangladesh in 2005 and the M.Sc. degree in Communication Technology from Universität Ulm, Germany, in 2008. He received his Ph.D. degree from Technische Universität München, Walter Schottky Institut Germany in 2011. In 2012, he worked at the nanophotonics group of Electrical and Computer Engineering Department at McGill University as a post-doc fellow.

Danilo Dadic received his B.S. in Physics from the University of California, Los Angeles, CA (UCLA) in 2014. He is currently working towards his M.S./PhD at the University of California, Santa Barbara, CA (UCSB) in the Electrical and Computer Engineering Department. His research focus is on the design, fabrication, and characterization of photonic integrated circuits closely integrated with electronic integrated circuits.

Leif A. Johansson (M'04) received a Ph.D. degree in engineering from University College London, London, U.K., in 2002. He has worked as a Research Scientist with the University of California, Santa Barbara since that time, and he is also a founder of Freedom Photonics where he is currently employed. His current research interests include design and characterization of integrated photonic devices for analog and digital applications and analog photonic systems and subsystems.

Larry A. Coldren (S'67–M'72–SM'77–F'82) received the Ph.D. degree in Electrical Engineering from Stanford University, Stanford, CA, in 1972. After 13 years in the research area at Bell Laboratories, he joined University of California, Santa Barbara in 1984. He is the Fred Kavli Professor of Optoelectronics and Sensors and holds appointments in the Departments of Materials and Electrical and Computer Engineering. From 2009 – 2011 he served as Dean of the College of Engineering. In 1990, he cofounded Optical Concepts, later acquired as Gore Photonics, to develop novel VCSEL technology, and, in 1998, he cofounded Agility Communications, later acquired by JDSU, to develop widely-tunable integrated transmitters.
At UCSB, he has worked on multiple-section widely-tunable lasers and efficient vertical-cavity surface-emitting lasers (VCSELs). More recently, his group has developed high-performance InP-based photonic integrated circuits (PICs) as well as high-speed VCSELs.
He has authored or coauthored over a thousand journal and conference papers, He also has co-authored eight book chapters, a widely used textbook, and has been issued 65 patents. He is a recipient of the 2004 John Tyndall, 2009 Aron Kressel, 2014 David Sarnoff, and 2015 IPRM Awards, and he is a Life Fellow of the IEEE, a Fellow of the OSA and IEE, and a member of the National Academy of Engineering.

I. Photonic Integrated Circuits

D. Signal Processing with Active Micro-rings
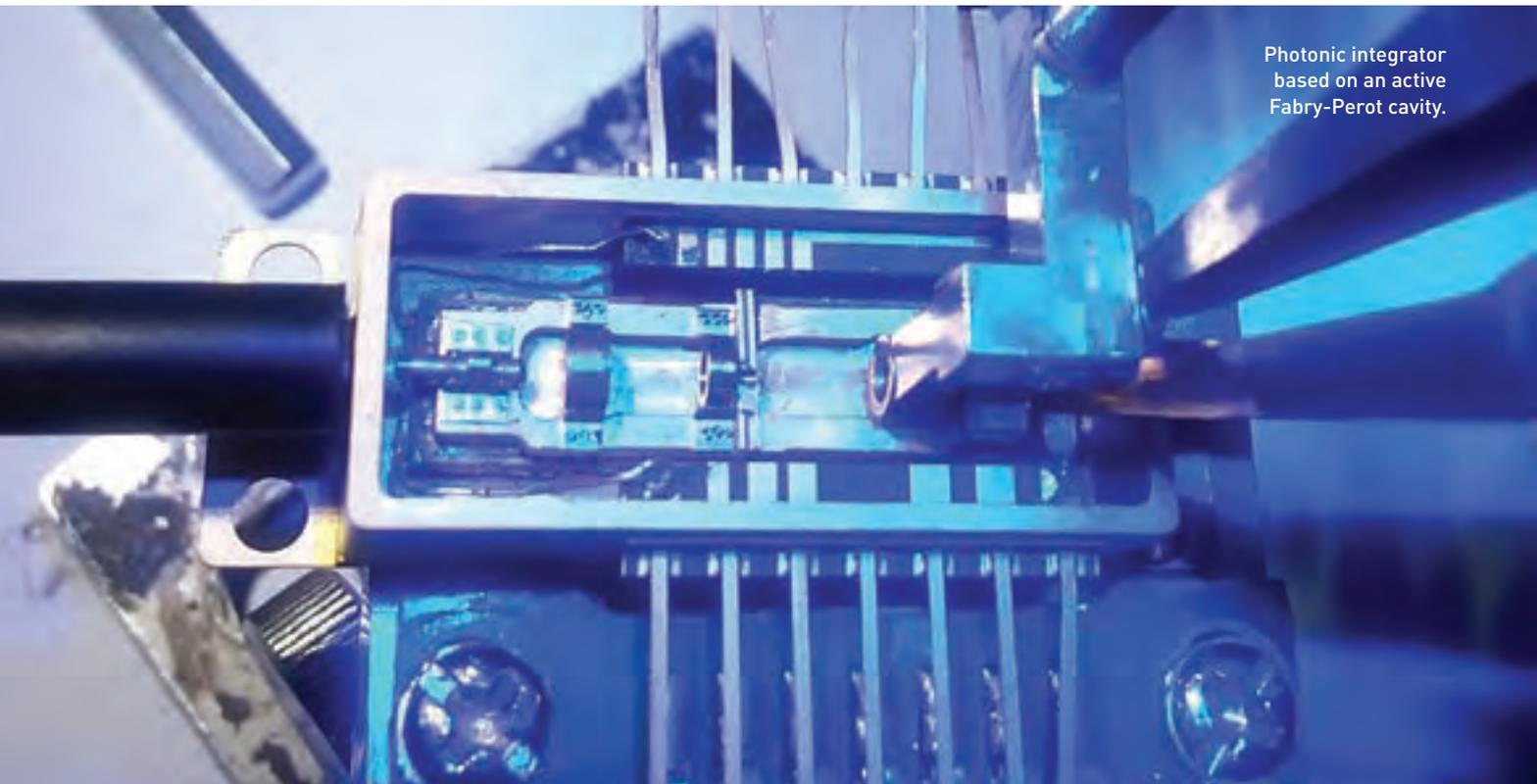
Photonic integrator
based on an active
Fabry–Perot cavity.

Ming Li, IS-CAS

OPTICAL ENGINEERING

Advances in **All-Optical Circuits**

Ming Li, Weilin Liu, Ningbo Huang, Robert S. Guzzon, Ninghua Zhu, Jose Azaña, Larry A. Coldren and Jianping Yao

New photonic temporal integrators could push past some of the processing-speed limitations of electronic approaches.

All-optical signal processing attracts much attention because of its potential to overcome the bandwidth and speed bottlenecks of electronic circuits. Many all-optical signal processing techniques already show up in a wide range of applications, like ultrafast telecommunications, optical computing, microwave photonics and biophotonics. These techniques offer processing bandwidths up to several THz—significantly faster than their electronic counterparts.

To build an all-optical signal-processing and computing platform, we need to replace electronic circuit components with photonic counterparts,

CIRCUIT PERFORMANCE COMPARISON

DIFFERENTIATOR BANDWIDTH

Electronic: **<1 GHz**

Photonic: **>25 THz**

INTEGRATOR BANDWIDTH

Electronic: **<1 GHz**

Photonic: **>200 GHz**

and thereby emulate processes and structures in the electronic domain using photonic technologies. Recently, all-optical temporal differentiators and integrators, and real-time Fourier and Hilbert transformers have been tested in the lab using fiber and integrated optics platforms, with bandwidths two to four orders higher than those of electronic equivalents.

We have recently demonstrated two kinds of all-optical temporal integrators. Each design is capable of calculating the time integral of an arbitrary optical temporal waveform and has the potential to reach processing speeds well beyond the capabilities of electronic

integrators. An all-optical temporal integrator could be used to realize arbitrary waveform generation, all-optical memory units and programmable differential-equation solvers, among other applications.

Active Fabry–Perot cavity integrator

One of our proposed all-optical temporal integrators is based on numerical modeling of an active Fabry-Perot (FP) cavity. The gain medium in the FP cavity is a semiconductor optical amplifier (SOA) with a high gain coefficient. The length of its integration time window is widely tunable and could be extended to be infinitely long by properly setting the injection current. This feature is important because it could greatly extend memory time when used for creating random access memory (RAM).

SOAs can be easily integrated with other semiconductor devices, such as lasers, modulators and photodetectors in photonic integrated circuits; this is another critical feature for achieving integrated all-optical signal-processing circuits with complex functionality.

Based on the use of an FP cavity with nearly feasible parameters, such as net modal gain and gain recovery speed, we successfully demonstrated a photonic temporal integrator with an integration time window of 160 ns and an operational bandwidth of 180 GHz. We calculated the time-bandwidth product of the simulated photonic temporal integrator to be 28,800—about two orders of magnitude higher than any previously reported result that we know of.

Active ring cavity integrator

Our second proposed all-optical temporal integrator includes a ring structure coupled with two bypass waveguides in an InP-InGaAsP material system consisting of SOAs and current-injection phase modulators (PMs).

During experimental testing, we modulated an input signal from an electronic arbitrary waveform generator onto a tunable laser. When we tuned the carrier wavelength to match the operation wavelength of the all-optical integrator, the output integrated waveform was converted into an electrical signal in a photodetector, which was then measured in a high-speed sampling oscilloscope. Within the ring, two SOAs were incorporated to compensate for the insertion loss.

We reported an experimental integration time window as long as 6,331 ps, an order of magnitude longer than any other photonic integrator we could find. In addition, there is a current injection PM in the ring for wavelength

FABRY-PEROT CAVITY
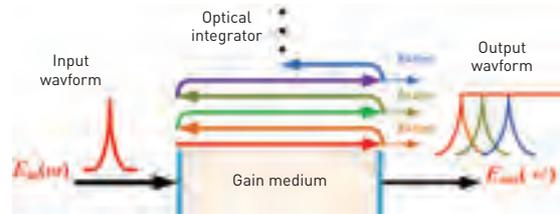
ACTIVE RING CAVITY
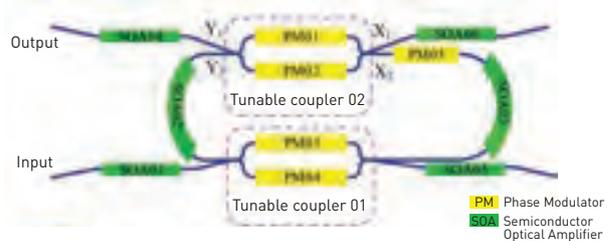
tuning. We believe our demonstration is the first report of an all-optical temporal integrator with an ultra-long integration time window and an ultra-wide tunable operation wavelength.

Next steps

Despite promising experimental results, our two integrators suffer from relatively low processing speeds—they still exceed electronic integrator performance, but perform well below the full theoretical potential of an all-optical solution. This limitation is due to the relatively long cavity of our designs. We are working on improving our designs for future demonstrations.

Nevertheless, our proposed integrators provide noteworthy integration time windows and represent an important step toward realizing efficient all-optical signal-processing circuits capable of overcoming the limitation in integration time window, bandwidth and power consumption imposed by electronics. OPN

M. Li (ml@semi.ac.cn) is with the Inst. of Semiconductors, Chinese Acad. of Sci. (IS-CAS); Univ. of Ottawa, Canada; and the Institut National de la Recherche Scientifique - Énergie, Matériaux et Télécommunications (INRS-EMT), Canada. W. Liu and J. Yao are with the Univ. of Ottawa. N. Huang and N. Zhu are with CAS. R.S. Guzzon and L.A. Coldren are with the Univ. of California, Santa Barbara, USA. J. Azaña is with INRS-EMT.

To Learn More …

▶ M. Ferrera et al. Nat. Commun. **1**(29) (2010).

▶ M. Li et al. Opt. Express **20**, 28273 (2012).

▶ N.B. Huang et al. Opt. Express **22**, 3105 (2014).

▶ W. Liu et al. IEEE/OSA J. Lightw. Technol. **32**, 3654 (2014).

II. VCSELs and Cavity QED

A. VCSEL Interconnects

On-Chip VCSEL Interconnects Enabled by 3-D Interposer-Based Integration and Polarization Modulation

Larry A. Coldren[1] and Ajit V. Barve[2]

[1]*Department of Electrical and Computer Engineering, University of California, Santa Barbara, CA 93117, USA*
[2]*now at JDSU Corporation, San Jose, CA 95134, USA*
coldren@ece.ucsb.edu

Invited Paper

Abstract: Optical interconnects are required for a continued scaling of a version of Moore's Law. VCSELs remain the most efficient sources to integrate, and these can be compatibly integrated with emerging 3-D integration technology using active interposers. Polarization-modulation can double the bisection bandwidth available together with coarse WDM and other modulation techniques.

OCIS codes: (140.0140) Lasers and laser optics; (250.0250) Optoelectronics

1. Introduction

Within the past decade there has been a tremendous amount of progress on Si-photonics as well as Si-system-in-a-package technology[1,2]. Perhaps we now see some convergence between these two. Not too long ago, a main selling point for Si-photonics was being able to put all of the photonics and electronics on a single chip. Today, the emergence of 2.5-D as well as 3-D integration—the concept of placing numerous chiplets on a common interposer as shown in Fig.1—is beginning to change this perspective[1-3]. In fact, even before this, the simple issue of incompatibility of the photonics with the electronics, either in size, in manufacture, in performance, or in operation, has led to a similar desire to have separate chips, stacked on top of or beside of each other, very closely together. This change in perspective has also re-opened the issue of having different materials platforms for the different chiplets.
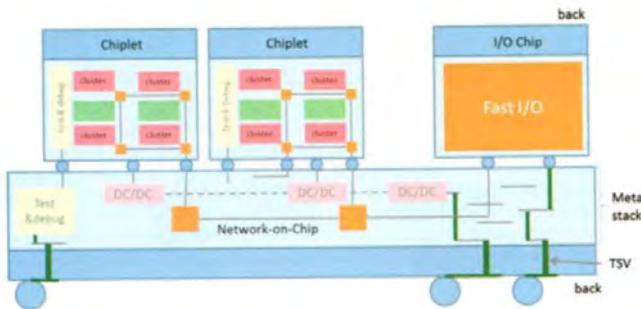
Figure 1: Schematic view of the interposer concept. [1]

In this paper, we will review the performance of state-of-the-art laser sources as candidates for integration with interposers and conclude that VCSELs are still the leading practical choice. We specifically will not consider schemes for coupling light from external sources, or sources that do not emit sufficient well-directed powers. VCSELs can operate over temperature ranges exceeding 60 °C and maximum temperatures over 120 °C with useful output powers. Over such temperature ranges, ~ 30 course WDM channels are possible with data rates ~40 Gb/s using simple direct modulation of the laser drive currents with some of the lowest total power dissipations, including the bias and modulation drive powers. For such WDM over this temperature range, multiple VCSEL chiplets would be involved with wavelengths extending from 850nm to the 1060nm range. This enables relatively simple muxing and demuxing at both ends of the optical links.

Secondly, we will discuss in more detail our more recent results with polarization modulation [4]. Prior work has demonstrated [5-7] that it is possible to control the polarization by means of asymmetric current injection (ACI) in the active region of the VCSEL. Since this technique relies on current induced anisotropies in the VCSEL, the polarization can be controlled at ultrahigh speeds. Most prior work obtained with ACI has been limited ~50kHz [8] due to the dominant thermal polarization switching. However, in our recent report electrically controlled polarization modulation speeds of over 4Gb/s were shown, and those VCSELs had ultralow threshold currents (~150-300μA) as well as very good differential quantum efficiencies. This is still the fastest reported direct modulation of the polarization of

a VCSEL. With this technique we now demonstrate that the data rate obtained with other modulation techniques can be doubled by modulating different data on each polarization and simple polarization filtering at the receiver.

2. Polarization VCSEL Results

The VCSELs used for polarization-modulation experiment consisted of MBE grown, strained InGaAs/GaAs quantum well devices, optimized for lasing at 980nm, with a bottom emitting architecture. A dual intracavity structure is used to maximize the effect of asymmetric current injection. A schematic of the device architecture is shown in Fig. 2. Two sets of P and N contacts are fabricated, such that the current P1N1 flows perpendicular to P2N2, to maximize the current asymmetry. Orientation of these contacts are along <110> and <1$\bar{1}$0> crystalline planes, to maximize the anisotropy.
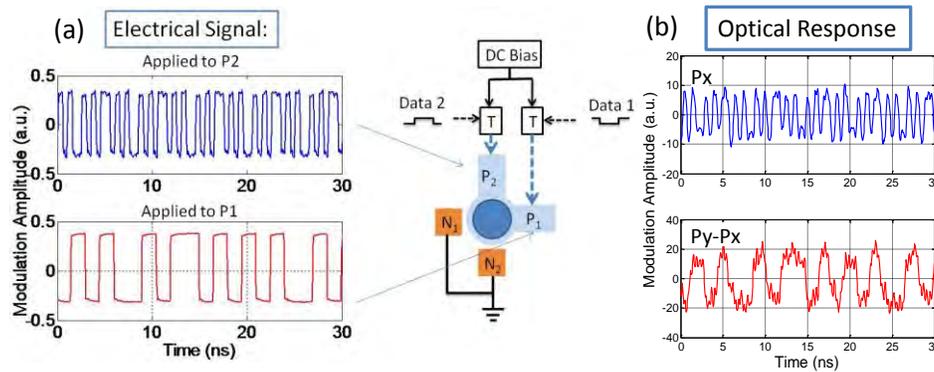
Fig. 2: (a) Biasing scheme for the two contacts of a VCSEL: P1N1 is modulated with Data 1, and P2N2 is modulated with Data 2, (b) Optical response at the output of the VCSEL: X polarization only (top) and the difference between Y and X polarization (bottom)

The LI curve on a typical chip had a threshold current of 0.3 mA and an output power of 0.6 mW at 2 mA with 4 spontaneous flips in polarization in between—the polarization was opposite for application of the current to the opposite set of terminals. The polarization contrast ratios exceeded 14dB by changing the directionality of the current flow. The experimental setup to exploit this to modulate the polarization of the VCSEL is shown in Fig. 2(a). Both P contacts of this multimode VCSEL are biased at a common DC current via bias-T. One set of data is applied across P1-N, while a second data-stream is applied to P2-N. The output of the VCSEL is passed through a polarizer, focused on to a multimode fiber and detected with a high speed detector. Fig. 2(b) shows the polarization resolved time domain response obtained on an oscilloscope. For this particular case, the signal on P1-N1 (data 1) modulates both X and Y polarizations, while the signal on P2-N2 (data 2) modulates only the X polarization. Therefore, by simply subtracting the output of X-polarization (P_x) from that of Y-polarization (P_y), the two data-streams are completely recovered. Thus, we demonstrate for the first time, that a VCSEL can support simultaneous, independent modulation on two different linear polarized modes—effectively doubling the maximum possible data-rate from the VCSEL. It is expected that the polarization switching speed can be further improved with this technique, by reducing the parasitic capacitance.

 References
[1] S. Cheramy, et al, *Chip Scale Review*, **18** (3) May/June, 2014.
[2] M. Heck , et al, *IEEE JSTQE*, **19** (4) 6100117, July/August 2013.
[3] www.luxtera.com
[4] A. Barve, A. Mehta, A. Husain, L. Coldren, *Optical Interconnects Conf.*, TuC5, Coronado Bay, CA, May, 2014.
[5] L. M. Augustin, et al, *IEEE Photon. Technol. Lett.,* **16** (3), 708 (2004)
[6] Y. Zheng et al, *IEEE Photon. Technol. Lett.,* **23** (5), 305 (2011)
[7] Y. Sato et al, *IEEE Photon. Technol. Lett*., **20** (17), 1446 (2008)
[8] M.P. Tan et al, *IEEE Photon. Technol. Lett*., **24** (9), 745 (2012)

II. VCSELs and Cavity QED

B. Cavity Quantum Electrodynamics

Polarization degenerate solid-state cavity quantum electrodynamics

Morten P. Bakker,[1] Ajit V. Barve,[2] Thomas Ruytenberg,[1] Wolfgang Löffler,[1] Larry A. Coldren,[2] Dirk Bouwmeester,[1,3] and Martin P. van Exter[1]

[1]*Huygens-Kamerlingh Onnes Laboratory, Leiden University, P.O. Box 9504, 2300 RA Leiden, Netherlands*
[2]*Departments of Electrical and Computer Engineering, University of California, Santa Barbara, California 93106, USA*
[3]*Department of Physics, University of California, Santa Barbara, California 93106, USA*

A polarization degenerate microcavity containing charge-controlled quantum dots (QDs) enables equal coupling of all polarization degrees of freedom of light to the cavity QED system, which we explore through resonant laser spectroscopy. We first measure interference of the two fine-split neutral QD transitions and find very good agreement of this V-type three-level system with a coherent polarization-dependent cavity QED model. We also study a charged QD that suffers from decoherence and find also in this case that availability of the full-polarization degrees of freedom is crucial to reveal the dynamics of the QD transitions. Our results pave the way for postselection-free quantum devices based on electron-spin–photon polarization entanglement.

I. INTRODUCTION

Quantum dots (QDs) embedded inside microcavities are of interest for hybrid optical-solid-state quantum information schemes [1,2] and long-distance quantum networks [3,4]. A key ingredient is the realization of entanglement between a QD spin and a single photon. Several experiments have demonstrated this by utilizing spontaneous emission [5–7], but these methods require postselection and are therefore not suitable for deterministic approaches. The need for postselection can be eliminated by using the spin-dependent reflection or transmission of a photon by a quantum dot in a cavity QED system. Several protocols have been proposed that either require polarization degenerate microcavities in order to couple with circular polarized light [8,9] or would be aided in order to match more easily with linear polarized transitions [10]. Further key system requirements are charge-controlled QDs and access to the Purcell or strong-coupling regime, which has been realized in photonic crystal cavities [11] and micropillars [12]. Micropillars have the additional benefit of mode matching to external fields and polarization control of the cavity modes [13–18].

In this paper we report on a system exhibiting all these features, a charge-controlled quantum dot coupled to a polarization degenerate micropillar cavity. The microcavity consist of two distributed Bragg reflectors, a $3/4\lambda$-thick aperture region for transverse mode confinement and a λ-thick cavity layer, containing InAs self-assembled QDs embedded inside a PIN-diode structure [13,19]. By systematically varying the size and shape of the oxide aperture, we were able to select, on average, one polarization degenerate cavity (polarization splitting <3 GHz) out of a (6×7) array [20]. This technique could be combined with a technique to actively tune the polarization properties by applying laser-induced surface defects [21] to enhance the sample yield. We tune the QD transition through the cavity resonance by the quantum confined Stark effect, induced by an applied bias voltage across the active region [22,23]. In principle this can be combined with other QD tuning techniques, such as strain tuning [24–26], which would further increase the sample yield. Further details
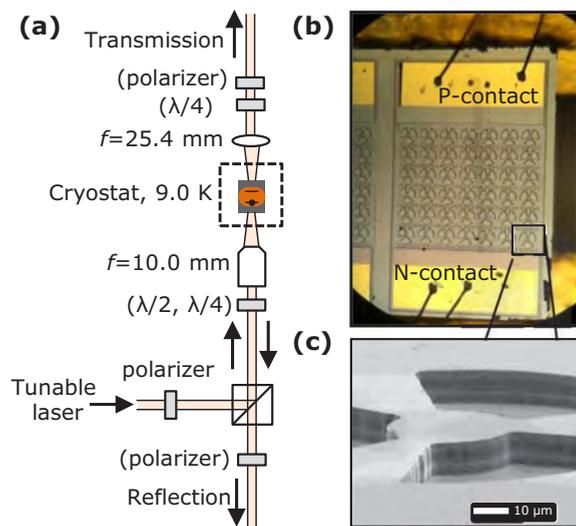
FIG. 1. (Color online) (a) Schematic of the setup. Light is coupled into a microcavity mode, and the reflection and transmission spectra are recorded using single-photon avalanche photodiodes. The elements with names between brackets can be introduced for polarization analysis with either linear or circularly polarized light. $\lambda/2$ ($\lambda/4$): half-wave (quarter-wave) plate. (b) Optical microscope image of a sample. (c) Electron micrograph of the cavity region.

on the sample structure and characterization can be found in the Appendix A. The setup and optical and electron microscope images of the sample are shown in Fig. 1.

This system enables polarization-resolved studies, which, as we will demonstrate, provide insight into the excitonic coherence of the system. First, we study the coherent interaction of charge-neutral quantum-dot transitions with resonant laser light and give a theoretical description. Then, we investigate a singly charged QD and study its more complex dynamics, which we can describe with a second decoherent model in which all spin-photon entanglement is lost.

II. NEUTRAL QUANTUM DOT

The lowest-energy levels of a neutral QD are depicted in Fig. 2(e). Due to the QD anisotropy, the electron-hole exchange interaction leads to a fine-structure splitting of the excited states (~3 GHz for the QD under study), and the neutral ground state is coupled to two excited states by two linear orthogonally polarized transitions. In the resonant reflection measurements in Fig. 2(a), the QD-cavity anticrossing, as a hallmark of strong to intermediate QD-cavity coupling, is clearly visible. Low laser power ($P_{\text{laser}} = 1$ pW) is used in order to avoid saturation of the QD transition, charging [27], and dynamical nuclear spin polarization effects [28]. Figures 2(b) and 2(c) show reflection and transmission spectra for a voltage $V = 0.725$ V, where QD1 is tuned into resonance with the cavity. The spectra are recorded for three linear polarizations that couple with the low-frequency QD transition ($\theta_{\text{in}} = 0°$), the high-frequency QD transition ($\theta_{\text{in}} = 90°$), or both QD transitions ($\theta_{\text{in}} = 45°$).

For 0° and 90° polarization we observe that the quantum dot is able to restore high cavity reflectivity with near-unity fidelity, but this effect appears to be reduced for 45°. Additionally, we show spectra when a crossed polarizer is used in the transmission path in Fig. 2(d). We see that for 0° and 90° the light matches the natural polarization axes of the QD and that this polarization is maintained, resulting in a very low signal. For 45° incoming polarization the transmission is significant, however. In the following, we develop a theoretical model to gain insight into the dynamics.

The transmission amplitude through a cavity with a coupled two-level system is given by [17,29,30]

$$t = \eta_{\text{out}} \frac{1}{1 - i\Delta + \frac{2C}{1 - i\Delta'}}, \quad (1)$$

where $\Delta = 2(\omega - \omega_c)/\kappa$ is the relative detuning between the laser (ω) and cavity (ω_c) angular frequencies, $\Delta' = (\omega - \omega_{\text{QD}})/\gamma_\perp$ is the relative detuning between the laser and QD transition (ω_{QD}), and η_{out} is the output coupling efficiency. The device cooperativity is $C = g^2/\kappa\gamma_\perp$, where κ is the total intensity damping of the cavity, $\gamma_\perp$ is the QD dephasing rate, and g is the QD-mode coupling strength. We obtain close to perfect mode matching, and therefore the total transmittivity through the cavity is given by $T = |t|^2$, and the total reflectivity is given by $R = |1 - t|^2$. A more detailed description of Eq. (1) is provided in Appendix B.

An important figure of merit of the QD-cavity system is the cooperativity parameter C. By fitting our model to the experimental data in Fig. 2 for $\theta_{\text{in}} = 0°$ and $\theta_{\text{in}} = 90°$, we find $C = 2.5 \pm 0.5$, a value similar to that previously reported [17]. We also obtain $\gamma_\perp = 2.0 \pm 0.5$ ns^{-1}, which corresponds to a total dephasing time $\tau = 500$ ps and total cavity damping rate $\kappa = 77$ ns^{-1}, which corresponds to a quality factor of $Q \sim 2.6 \times 10^4$ (see Appendix B). Since $\gamma_\perp < 2g = 39$ ns$^{-1} < \kappa$, this places the system in the intermediate-coupling regime.

The line shapes corresponding to an empty cavity can be calculated from the fitted curves and are shown by the gray curves in Figs. 2(b) and 2(c). The very small dependence of the
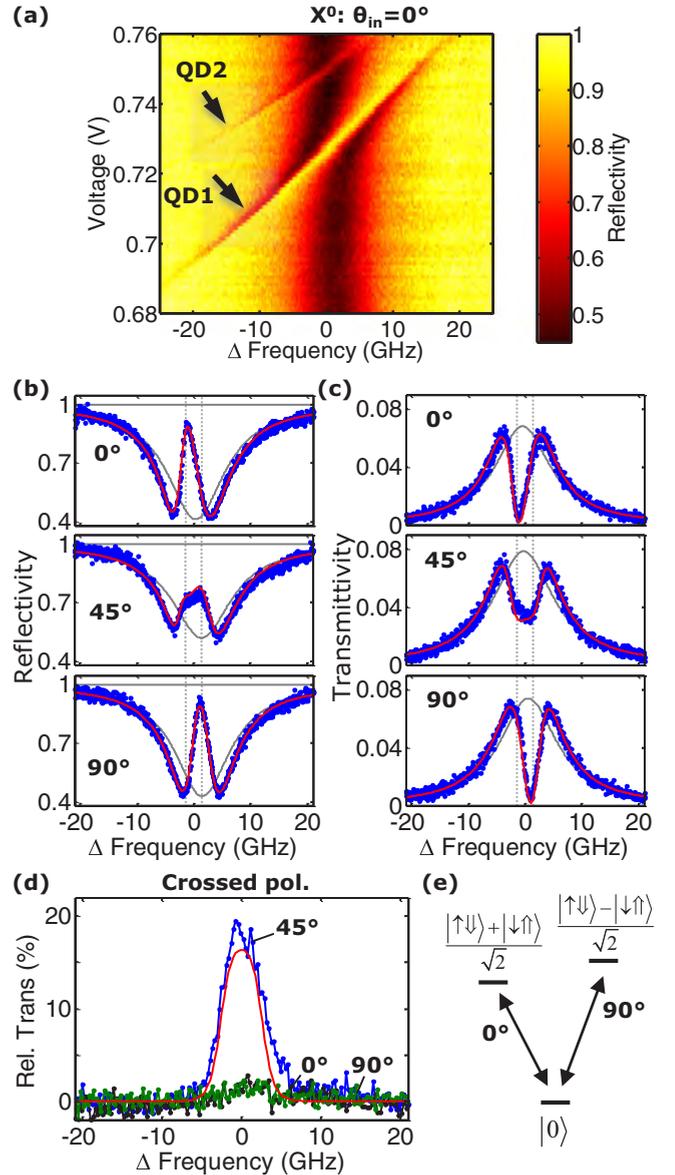
FIG. 2. (Color online) (a) Reflectivity measurement of two neutral QDs as a function of the scanning laser frequency and applied voltage. The incoming polarization $\theta_{\text{in}} = 0°$, $P_{\text{laser}} = 1$ pW, and $\lambda \approx 940$ nm. (b) Reflectivity and (c) transmittivity spectra of QD1 recorded at $V = 0.725$ V for various incoming linear polarizations. Blue points: experimental data. Red line: fitted curve using Eqs. (1) and (2). Gray curve: empty cavity, calculated from the fits. Vertical dashed lines: frequencies corresponding to the two fine-split transitions. (d) Transmittivity spectra when a crossed polarizer is used with respect to the incoming polarization, relative to the maximum transmittivity of an uncoupled cavity. The red line is calculated using Eqs. (1) and (2) and the parameters obtained from the fits in (b) and (c). (e) Energy-level diagram of the ground-state and lowest-energy excited states of a neutral QD.

cavity resonance frequency on the polarization angle confirms the high degree of polarization isotropy of this device.

To account for the fine-structure splitting of the neutral QD transitions in the polarization-degenerate cavity, we write the
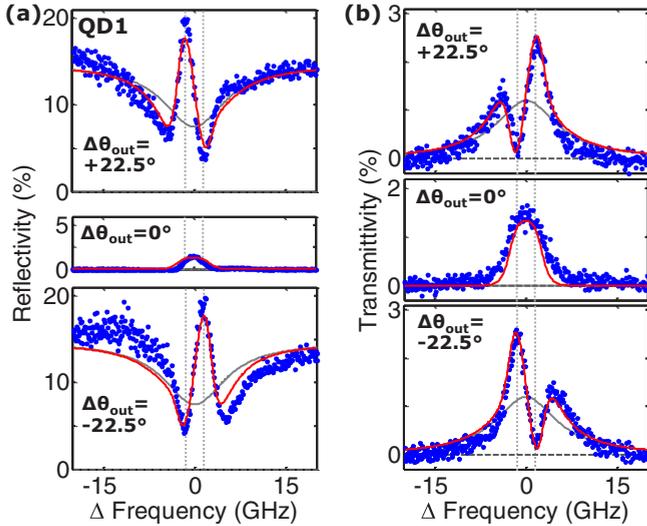
FIG. 3. (Color online) Resonant (a) reflection and (b) transmission spectroscopy with a neutral QD (QD1 in Fig. 2) for $\theta_{\text{in}} = 45°$ and for various $\theta_{\text{out}} = \theta_{\text{in}} + 90° + \Delta\theta_{\text{out}}$. Blue dots: experimental data. Red lines: predicted curves using Eqs. (1) and (2) and the parameters obtained from the fits in Figs. 2(b) and 2(c). Gray lines: predicted curves corresponding to an empty cavity. Vertical dashed lines mark the two transitions split by the fine-structure interaction.

transmission of the system in terms of a Jones matrix,

$$\mathbf{t}(\omega) = \begin{pmatrix} t_x(\omega) & 0 \\ 0 & t_y(\omega) \end{pmatrix}.$$

The measured transmittivity therefore depends on the input and output polarization as

$$t_{\theta_{\text{out}},\theta_{\text{in}}}(\omega) = \mathbf{e}_{\text{out}}^{\dagger}\mathbf{t}(\omega)\mathbf{e}_{\text{in}}, \qquad (2)$$

where $\mathbf{e}_i = (\cos(\theta_i), \sin(\theta_i))$ defines the linear input/output ($i = $ in/out) polarization with angle θ_i. This model assumes that when the two transitions are excited simultaneously ($\theta_{\text{in}} = 45°$), coherence in the system is fully maintained, leading to quantum interference between the transmission amplitudes t_x and t_y. In an incoherent system we would obtain a classical mixture of the excited states, making such interference impossible. The reflectivity is calculated in a similar way by using $r_{x/y} = 1 - t_{x/y}(\omega)$ in the Jones matrix.

To further explore the validity of Eq. (2) and to demonstrate the full power of polarization degenerate cavity QED, we show in Figs. 3(a) and 3(b) reflection and transmission spectra for $\theta_{\text{in}} = 45°$, while $\theta_{\text{out}} = \theta_{\text{in}} + 90° + \Delta\theta_{\text{out}}$ is varied. For $\Delta\theta_{\text{out}} = 0°$, the crossed-polarizer condition, the transmission and reflection spectra consist of two partially overlapping Lorentzian lines split by ~ 3 GHz. The phase difference between these two resonances becomes apparent for the $\Delta\theta_{\text{out}} = +22.5°$ ($-22.5°$) spectra, which can be seen as the *coherent sum* of the $\Delta\theta_{\text{out}} = 0°$ and the $\Delta\theta_{\text{out}} = +45°$ ($-45°$) spectra, where the latter contains only the high-frequency (low-frequency) transition. All the red curves in Figs. 2 and 3 are produced with the same parameters for C, κ, and $\gamma_{\perp}$ and fit the experimental data very well. The results demonstrate how in a polarization degenerate cavity the fine-split excited states of a neutral QD can be simultaneously addressed in a coherent

way. Furthermore, these interference measurements hold great promise as a clever combination of $\mathbf{e}_{\text{in}}$ and $\mathbf{e}_{\text{out}}$ can be used to tune the constructive or destructive interference between t_x and t_y. This forms a generic technique to increase the ratio between uncoupled and coupled cavity systems and thereby the fidelity of entanglement operations.

III. SINGLY CHARGED QUANTUM DOT

Now we turn to a different QD in the same polarization degenerate cavity but operated in a voltage regime around 0.9 V, where it is singly negatively charged. This system is of particular importance in quantum information as the optical transitions are polarization degenerate [see Fig. 4(a)] due to cancellation of electron-hole exchange interaction and enables coherent control of the resident electron spin if a small in-plane magnetic field is applied. We first focus on Figs. 4(b) and 4(c), which show transmission spectra when circularly (σ^+) or linearly polarized light is coupled into the cavity and transmitted light of the same (i.e., parallel) polarization is recorded. We define the contrast as $(|t_c|^2 - T)/|t_c|^2$, with the measured transmittivity T with a QD and the calculated transmittivity $|t_c|^2$ without a QD. While for the neutral QD case we found contrasts of $>91\%$ in Fig. 2(c), we now observe a strongly reduced contrast of the QD resonance, which is $\sim 19\%$ when circularly polarized light is used and $\sim 26\%$ for linear polarization.

We use a slightly larger laser power ($P_{\text{laser}} = 10$ pW) compared to the neutral QD as we find that the charging effects are now significantly smaller due to less absorption of the resonant laser at this voltage. Furthermore, this intensity corresponds to a mean intracavity photon number $\langle\bar{n}\rangle = |t|^2 P_{\text{laser}}/(\kappa_m\hbar\omega) < 0.001$ and is therefore sufficiently small to prevent QD saturation effects from occurring.

In addition, we compared the cross-polarized transmitted intensity for circular and linear polarized light. For circular (σ^+ and σ^-) polarization, shown in Fig. 4(d), we observe negligible transmission, indicating that circular polarization remains unchanged. Surprisingly, for two linear orthogonal (lin1 and lin2) polarizations displayed in Fig. 4(e), we observe that about 10% of the light is transmitted relative to $|t_c|^2$, despite the low cooperativity (see below).

We will first try to explain our observations with a coherent model, which we adapt to the four-level system of a charged QD shown in Fig. 4(a): The ground state consists of the two spin eigenstates, oriented in the out-of-plane direction, which couple with two corresponding trion lowest-energy excited states by degenerate circularly polarized optical transitions carrying spin $\sigma^{\pm} = \pm 1$. We write $t_1^{\pm} \equiv t_1$ for the corresponding transmission amplitudes of $\sigma^{\pm}$ polarized light coupling with a corresponding transition and $t_c^{\pm} \equiv t_c$ for the case of an empty cavity. Since we do not control the electron-spin state it can be in any random state $|\phi_{\text{spin}}\rangle = \alpha|\uparrow\rangle + \beta|\downarrow\rangle$. With the incoming photon state $|\phi_{\text{in}}\rangle = \gamma|+\rangle + \delta|-\rangle$, we obtain for the input quantum state $|\Psi_{\text{in}}\rangle = |\phi_{\text{in}}\rangle \otimes |\phi_{\text{spin}}\rangle$. The spin-selective interaction with the cavity-QD system entangles the photon with the electron spin via

$$|\Psi_{\text{out}}\rangle = t_1\gamma\alpha|+\uparrow\rangle + t_c\gamma\beta|+\downarrow\rangle + t_c\delta\alpha|-\uparrow\rangle + t_1\delta\beta|-\downarrow\rangle.$$
$$(3)$$

49
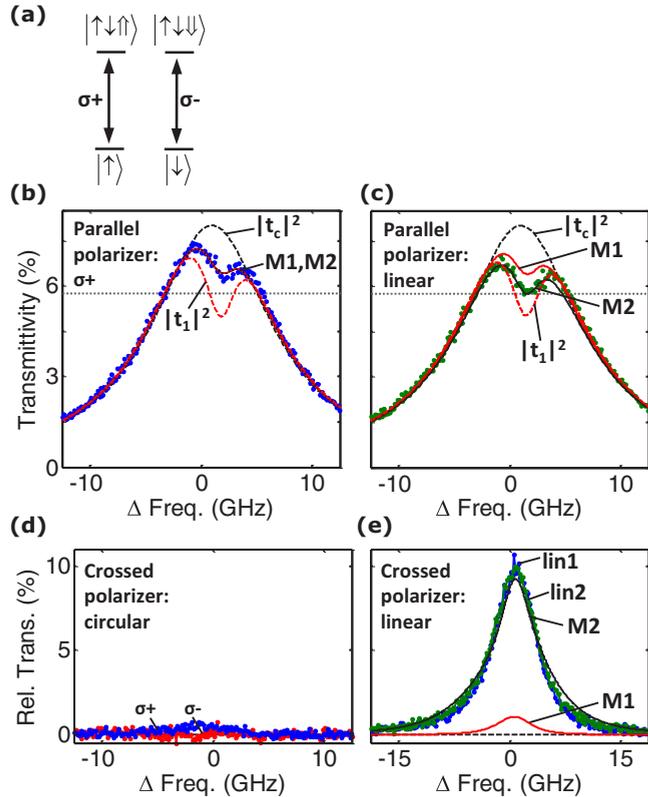
FIG. 4. (Color online) (a) Energy-level diagram of a singly charged QD. Transmission spectra for $P_{\text{laser}} = 10$ pW are shown for circular and linear polarization, analyzed with a (b) and (c) parallel or (d) and (e) crossed polarizer. The red-black dashed line in (b) is a fit of Eq. (4) (coherent model, M1) to the data, which yields the same result as Eq. (5) (decoherent model, M2). The red (black) solid lines in (c) and (e) predict the experimental data using Eq. (4) [Eq. (5)]. Black (red) dashed curves: empty (coupled) cavity calculations.

We then project this output state onto the detected polarization $|\phi_{\text{out}}\rangle = \gamma'|+\rangle + \delta'|-\rangle$ and take the trace over the electron spin to obtain the projected transmission:

$$T = |t_1 \gamma \gamma' + t_c \delta \delta'|^2 |\alpha|^2 + |t_c \gamma \gamma' + t_1 \delta \delta'|^2 |\beta|^2. \quad (4)$$

Since we do not control the spin state, we use $|\alpha|^2 = |\beta|^2 = 0.5$ for the balanced case. Note that this model (M1) is coherent in the sense that it still contains interference between the t_1 and t_c terms.

The red solid line in Fig. 4(c) shows how model M1 fits our data for the optimum cavity-QD coupling and QD dephasing parameters $C = 0.13$ and $\gamma_\perp = 9.5$ ns^{-1}. The dephasing rate cannot be explained by the decay rate of the excited state since lifetime measurements showed this to be about 1.2 ns. Instead, we attribute this much faster dephasing rate to an efficient cotunneling process across the 20-nm electron tunnel barrier, which is expected to be more pronounced for the flatter conduction band here compared to the neutral QD case presented before. This fast dephasing also reduces the cooperativity, which, however, might also be reduced due to low spatial overlap between the QD and the cavity mode. We expect that utilizing a thicker 35-nm tunnel barrier will

decrease the cotunneling process and enable high-fidelity spin-state preparation [31].

Next, we consider the linear-polarization data shown in Figs. 4(c) and 4(e), where the model prediction is shown by red lines. Equation (4) predicts that purely circular polarized light should pass the cavity unmodified and can therefore be fully blocked by a crossed polarizer ($\gamma \gamma' = \delta \delta' = 0$), which is, indeed, what we observe experimentally in Fig. 4(d). Significant discrepancies between the data and our model are, however, observed in Fig. 4(c) and in Fig. 4(e) in particular, where the cross-polarized transmission signal for linear polarizations lin1 and lin2 is much larger than expected. This cannot be caused by an energy splitting or phase difference between the two transitions because these splittings would have been visible in the data. Furthermore, the observed cross-polarized transmission is so large that it would require $C > 0.8$ in Eq. (4) to explain the cross-polarized transmission in Fig. 4(e), while we found $C = 0.13$ for the fit in Fig. 4(b).

This result therefore indicates that additional dephasing processes take place that project linear polarized light on the preferred circular basis of the QD transitions. The preference for this basis is known from Refs. [31–33] and is experimentally demonstrated by the fact that circularly polarized light remains circularly polarized after the interaction with the QD–cavity system. If the absorption and reemission of linear light were a fully coherent process, the linear polarization would largely remain, which is clearly not the case in Fig. 4(e).

To model the results, we now introduce a tentative model (M2) that describes the spin-exciton system as if it were fully decoherent, meaning that any light interacting with the QD is instantaneously projected on the QD transition polarization basis. This corresponds to immediate decoherence of the entangled state described by Eq. (3) and elimination of interference between the t_1 and t_c terms in Eq. (4). Since only a fraction of the light that enters the cavity becomes entangled with the QD spin state, we first need to calculate the fraction of the light that did not interact. We estimate this fraction T_0 by multiplying the cavity transmission with the QD response function: $T_0 = |t_c|^2 |\frac{1}{1+\frac{2C}{1-i\Delta'}}|^2$. The intensities of the circularly polarized components of the transmitted light that interacted with parallel and opposite electron spins are now given by $T_1' = |t_1|^2 - T_0$ and $T_c' = |t_c|^2 - T_0$, respectively.

The total transmitted intensity corresponds now to the incoherent sum of five transmission channels:

$$T = T_0 |\langle \phi_{\text{out}} | \phi_{\text{in}} \rangle|^2 + T_1' |\gamma \alpha \langle \phi_{\text{out}} |+\rangle|^2 + T_c' |\delta \alpha \langle \phi_{\text{out}} |-\rangle|^2$$
$$+ T_c' |\gamma \beta \langle \phi_{\text{out}} |+\rangle|^2 + T_1' |\delta \beta \langle \phi_{\text{out}} |-\rangle|^2. \quad (5)$$

The transmissions predicted by the incoherent model [M2, Eq. (5)] and coherent model [M1, Eq. (4)] are equivalent in the case of circular incoming polarization [Figs. 4(b) and 4(d)]. They differentiate, however, in the case of the linear-polarization data in Figs. 4(c) and 4(e). The solid black curves predicted by the incoherent model (M2), based on the parameters deduced from Fig. 4(b), agree very well, while coherent model (M1) does not.

While the polarization degenerate microcavities enables systematic polarization analysis and the identification of a high degree of decoherence in the charged QD system, the

exact origin of decoherence is not known to us. We think it is related to the cotunneling process, and future sample designs with thicker tunnel barriers will resolve this issue.

IV. CONCLUSION

In conclusion, we have demonstrated a polarization degenerate solid-state cavity QED system with charge control, which allows full use of all polarization degrees of freedom. Here, simple polarimetric reflection and transmission measurements enable the study of the coherence properties of the coupled QD-cavity system for neutral and charged quantum dots. This is an important advance for fundamental studies of spin dynamics and optical interactions in solid-state cavity QED systems and an important step towards quantum information applications with single-electron and hole spin qubits and postselection-free spin-photon polarization interaction.

APPENDIX A: SAMPLE STRUCTURE AND CHARACTERIZATION

The sample under study has been grown by molecular beam epitaxy on a GaAs[100] substrate. Two distributed Bragg reflectors (DBR) surround an aperture region and a λ-thick cavity region containing in the center InAs self-assembled quantum dots (QDs). The top DBR mirror consists of 26 pairs of $\lambda/4$ layers of GaAs and $Al_{0.90}Ga_{0.10}As$, while the bottom mirror consists of 13 pairs of layers of GaAs and AlAs and 16 pairs of GaAs and $Al_{0.90}Ga_{0.10}As$ layers. In this way the reflectivities of the top and bottom mirrors are matched to enable transmission and reflection measurements and optimize the incoupling efficiency. The oxidation aperture consists of a 10-nm AlAs layer embedded between 95-nm $Al_{0.83}Ga_{0.17}As$ and 66-nm $Al_{0.75}Ga_{0.25}As$ layers, providing a linearly tapered oxidation upon wet oxidation. The QDs are separated by a 20-nm GaAs tunnel barrier to n-doped GaAs (Si dopant, concentration 2.0×10^{18} cm^{-3}) and by a 107-nm GaAs layer to p-doped GaAs (C doping, concentration 1.0×10^{18} cm^{-3}).

By analyzing the confined optical modes and the wavelength splitting between the fundamental and first-order optical modes, an estimation can be made for the maximum Purcell factor and the numerical aperture (NA) of the fundamental mode. A high Purcell factor is necessary to observe QD couplings close to the strong-coupling regime, while a modest NA enables perfect mode matching to external fields.

To characterize the optical properties of the confined modes, the sample is excited using an 852-nm laser diode and photoluminescence is recorded using a spectrometer as a function of position. Hermite-Gaussian modes are clearly identified in Fig. 5. Following methods described in [34], we

(a) $\lambda_{00} = 940.48$ nm **(b)** $\Delta\lambda_{01} = 1.40$ nm **(c)** $\Delta\lambda_{10} = 2.87$ nm
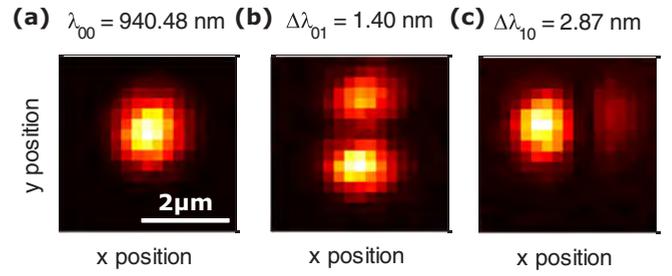
FIG. 5. (Color online) Spatial PL scans of the Hermite-Gaussian modes, where (a) is the fundamental mode Ψ_{00} and (b) and (c) are the first-order Ψ_{10}/Ψ_{01} modes. Light: more PL counts. The labels denote the wavelength λ_{00} of the fundamental mode or the wavelength splitting $\Delta\lambda_{10/01} = \lambda_{00} - \lambda_{10/01}$.

calculate the mode volume V using

$$V = L_{\text{cav}} \frac{\lambda_{00}^3}{8\pi n_0^2 \sqrt{\Delta\lambda_{01}\Delta\lambda_{10}}}, \tag{A1}$$

where $L_{\text{eff}} \approx 5\lambda_{00}/n \approx 1.4$ μm is the effective cavity length, $\lambda_{00} = 940.48$ nm is the wavelength of the fundamental mode in vacuum, $n \approx 3.25$ is the average refractive index, and $\Delta\lambda_{01/10}$ are the mode splittings between the $\Psi_{01/10}$ modes and the Ψ_{00} mode. Filling in the experimentally obtained values for the mode splitting, we obtain $V = 2.2$ μm^3. The expected maximum Purcell factor P is given by

$$P = \frac{3}{4\pi^2} \left(\frac{\lambda_{00}}{n_0}\right)^3 \frac{Q}{V}, \tag{A2}$$

where $Q = 2.6 \times 10^4$ is the quality factor measured during the resonant spectroscopy scans. Using the above-mentioned values, we find $P = 22$. The intensity of the fundamental mode, perpendicular to the propagation direction $\hat{z}$, has the form $I \propto \exp[-2(\frac{x^2}{w_x^2} + \frac{y^2}{w_y^2})]$, where $w_{x/y} = \frac{1}{n_0\pi}\sqrt{\frac{\lambda_{00}^3}{2\Delta\lambda_{10/01}}}$ is the mode waist. The numerical aperture of the Gaussian beam originating from the fundamental mode is given by NA$_{x/y} = \sin(\frac{\lambda_{00}}{\pi W_{x/y}})$, which gives NA$_x = 0.18$ and NA$_y = 0.25$. The NA of the objective used is 0.4, enabling perfect mode matching.

APPENDIX B: COMPLETE DESCRIPTION OF THE TRANSMISSION AMPLITUDE

The transmission amplitude through a cavity with a coupled QD is given by [17,29,30]

$$t = \eta_{\text{out}} \frac{1}{1 - i\Delta + \frac{2C}{1-i\Delta'}}, \tag{B1}$$

where the parameters are defined in the main text. We will here quantify the role of losses and its effect on the outcoupling efficiency $\eta_{\text{out}} = \frac{2\kappa_m}{\kappa}$, defined as the probability that a photon in the mode will leave the cavity through the top or bottom mirror. Here, κ_m is the damping rate of each Bragg mirror, κ_s is the scattering and absorption rate inside the cavity, and $\kappa = 2\kappa_m + \kappa_s$ is the total cavity intensity damping rate. Furthermore $\kappa_m = T_{\text{mirror}}/t_{\text{round}}$, where T_{mirror} is the transmittivity of a single mirror and $t_{\text{round}} = 2nL_{\text{cav}}/c$ is the cavity round-trip time. n is the average refractive index,

$L_{cav} \approx 5\lambda/n$ is the effective cavity length, c is the speed of light, and $\lambda \approx 940$ nm is the wavelength in vacuum.

The mirror damping rate $\kappa_m \approx 11$ ns^{-1} is calculated from the sample design parameters. Three observations consistently yield $\kappa_s \approx 55$ ns^{-1}: (i) the measured quality factor $Q \approx 2.6 \times 10^4$ is lower than $Q = 9.1 \times 10^4$ as determined by the mirror transmittivity $T_{mirror} = 3.4 \times 10^{-4}$ and cavity length and corresponds to $\kappa = 77$ ns^{-1}, (ii) the minimum reflectivity of the empty cavity $\frac{R_{min}}{R_{max}} = |1 - \eta_{out}|^2 \approx 0.5$, and (iii) the maximum transmission $T_{max} = |\eta_{out}|^2 \approx 0.08$ (not taking into account a ~30% reflectivity at the GaAs to air interface at the back of the sample). We attribute this scattering rate κ_s to

(spectrally broad) absorption losses in the doped layers and scattering by the oxide aperture. Reducing κ_s, for example, by using a lower doping concentration, is a major concern in future sample designs.

Finally, we will comment on the case of nonperfect mode matching. The total transmission T through the cavity is then given by $T = \eta_{in}\eta_T|t|^2$, where η_{in} is the incoupling efficiency and η_T is the collection efficiency at the transmission port. The total reflection is given by $R = \eta_R|1 - \eta_{in}t|^2$, where η_R is the collection efficiency at the reflection port. In the case of perfect mode matching $\eta_{in} = \eta_R = \eta_T = 1$.

---

[1] E. Waks and C. Monroe, Phys. Rev. A **80**, 062330 (2009).

[2] J. I. Cirac, A. K. Ekert, S. F. Huelga, and C. Macchiavello, Phys. Rev. A **59**, 4249 (1999).

[3] W. Yao, R.-B. Liu, and L. J. Sham, Phys. Rev. Lett. **95**, 030504 (2005).

[4] H. J. Kimble, Nature (London) **453**, 1023 (2008).

[5] K. De Greve, L. Yu, P. L. McMahon, J. S. Pelc, C. M. Natarajan, N. Y. Kim, E. Abe, S. Maier, C. Schneider, M. Kamp, S. Hofling, R. H. Hadfield, A. Forchel, M. M. Fejer, and Y. Yamamoto, Nature (London) **491**, 421 (2012).

[6] W. B. Gao, P. Fallahi, E. Togan, J. Miguel-Sanchez, and A. Imamoglu, Nature (London) **491**, 426 (2012).

[7] J. R. Schaibley, A. P. Burgers, G. A. McCracken, L.-M. Duan, P. R. Berman, D. G. Steel, A. S. Bracker, D. Gammon, and L. J. Sham, Phys. Rev. Lett. **110**, 167401 (2013).

[8] C. Y. Hu, W. J. Munro, J. L. O'Brien, and J. G. Rarity, Phys. Rev. B **80**, 205326 (2009).

[9] C. Bonato, F. Haupt, S. S. R. Oemrawsingh, J. Gudat, D. Ding, M. P. van Exter, and D. Bouwmeester, Phys. Rev. Lett. **104**, 160503 (2010).

[10] S. Sun and E. Waks, Phys. Rev. A **90**, 042322 (2014).

[11] S. G. Carter, T. M. Sweeney, M. Kim, C. S. Kim, D. Solenov, S. E. Economou, T. L. Reinecke, L. Yang, A. S. Bracker, and D. Gammon, Nat. Photonics **7**, 329 (2013).

[12] M. T. Rakher, N. G. Stoltz, L. A. Coldren, P. M. Petroff, and D. Bouwmeester, Phys. Rev. Lett. **102**, 097403 (2009).

[13] N. G. Stoltz, M. Rakher, S. Strauf, A. Badolato, D. D. Lofgreen, P. M. Petroff, L. A. Coldren, and D. Bouwmeester, Appl. Phys. Lett. **87**, 031105 (2005).

[14] S. Strauf, N. G. Stoltz, M. T. Rakher, L. A. Coldren, P. M. Petroff, and D. Bouwmeester, Nat. Photonics **1**, 704 (2007).

[15] A. Dousse, J. Suffczynski, A. Beveratos, O. Krebs, A. Lemaitre, I. Sagnes, J. Bloch, P. Voisin, and P. Senellart, Nature (London) **466**, 217 (2010).

[16] S. Reitzenstein and A. Forchel, J. Phys. D **43**, 033001 (2010).

[17] V. Loo, C. Arnold, O. Gazzano, A. Lemaître, I. Sagnes, O. Krebs, P. Voisin, P. Senellart, and L. Lanco, Phys. Rev. Lett. **109**, 166806 (2012).

[18] A. K. Nowak, S. L. Portalupi, V. Giesz, O. Gazzano, C. Dal Savio, P.-F. Braun, K. Karrai, C. Arnold, L. Lanco, I. Sagnes, A. Lemaître, and P. Senellart, Nat. Commun. **5**, 3240 (2014).

[19] P. M. Petroff, A. Lorke, and A. Imamoglu, Phys. Today **54**(5), 46 (2001).

[20] M. P. Bakker, A. V. Barve, A. Zhan, L. A. Coldren, M. P. van Exter, and D. Bouwmeester, Appl. Phys. Lett. **104**, 151109 (2014).

[21] C. Bonato, D. Ding, J. Gudat, S. Thon, H. Kim, P. M. Petroff, M. P. van Exter, and D. Bouwmeester, Appl. Phys. Lett. **95**, 251104 (2009).

[22] P. W. Fry *et al.*, Phys. Rev. Lett. **84**, 733 (2000).

[23] R. J. Warburton, C. Schaflein, D. Haft, F. Bickel, A. Lorke, K. Karrai, J. M. Garcia, W. Schoenfeld, and P. M. Petroff, Nature (London) **405**, 926 (2000).

[24] S. Seidl, M. Kroner, A. Hgele, K. Karrai, R. J. Warburton, A. Badolato, and P. M. Petroff, Appl. Phys. Lett. **88**, 203113 (2006).

[25] S. Sun, H. Kim, G. S. Solomon, and E. Waks, Appl. Phys. Lett. **103**, 151102 (2013).

[26] J. Gudat, C. Bonato, E. van Nieuwenburg, S. Thon, H. Kim, P. M. Petroff, M. P. van Exter, and D. Bouwmeester, Appl. Phys. Lett. **98**, 121111 (2011).

[27] J. Houel, A. V. Kuhlmann, L. Greuter, F. Xue, M. Poggio, B. D. Gerardot, P. A. Dalgarno, A. Badolato, P. M. Petroff, A. Ludwig, D. Reuter, A. D. Wieck, and R. J. Warburton, Phys. Rev. Lett. **108**, 107401 (2012).

[28] B. Urbaszek, X. Marie, T. Amand, O. Krebs, P. Voisin, P. Maletinsky, A. Högele, and A. Imamoglu, Rev. Mod. Phys. **85**, 79 (2013).

[29] A. Auffèves-Garnier, C. Simon, J.-M. Gérard, and J.-P. Poizat, Phys. Rev. A **75**, 053823 (2007).

[30] E. Waks and J. Vuckovic, Phys. Rev. Lett. **96**, 153601 (2006).

[31] M. Atatüre, J. Dreiser, A. Badolato, A. Högele, K. Karrai, and A. Imamoglu, Science **312**, 551 (2006).

[32] A. Högele, M. Kroner, S. Seidl, K. Karrai, M. Atatüre, J. Dreiser, A. Imamoğlu, R. J. Warburton, A. Badolato, B. D. Gerardot, and P. M. Petroff, Appl. Phys. Lett. **86**, 221905 (2005).

[33] R. J. Warburton, Nat. Mater. **12**, 483 (2013).

[34] C. Bonato, J. Gudat, K. de Vries, S. M. Thon, H. Kim, P. M. Petroff, M. P. van Exter, and D. Bouwmeester, Opt. Lett. **37**, 4678 (2012).

52

Optics Letters

Homodyne detection of coherence and phase shift of a quantum dot in a cavity

Morten P. Bakker,[1,*] Henk Snijders,[1] Wolfgang Löffler,[1] Ajit V. Barve,[2] Larry A. Coldren,[2] Dirk Bouwmeester,[1,2] and Martin P. van Exter[1]

[1]*Huygens-Kamerlingh Onnes Laboratory, Leiden University, P.O. Box 9504, 2300 RA Leiden, The Netherlands*
[2]*University of California Santa Barbara, Santa Barbara, California 93106, USA*
Corresponding author: mbakker@physics.leidenuniv.nl

A homodyne measurement technique is demonstrated that enables direct observation of the coherence and phase of light that passed through a coupled quantum dot (QD)-microcavity system, which in turn enables clear identification of coherent and incoherent QD transitions. As an example, we study the effect of power-induced decoherence, where the QD transition saturates and incoherent emission from the excited state dominates at higher power. Further, we show that the same technique allows measurement of the quantum phase shift induced by a single QD in the cavity, which is strongly enhanced by cavity quantum electrodynamics effects. © 2015 Optical Society of America

Quantum dots (QDs) are artificial atoms in the solid state with potential applications for quantum information [1]. Embedding QDs in high-Q microcavities holds promise to implement deterministic logic gates [2], entangle independent photons [3], and couple distant QDs to form a quantum network [4]. Additionally, cavity-enhanced light–matter interactions enable a powerful spectroscopic tool for QD characterization. In the following, we present a straightforward technique to analyze both the coherence as well as the quantum phase shift of light transmitted through a QD-cavity system.

Several techniques have been demonstrated to determine the coherence of the emission of a coherently driven two-level transition in an atomic or molecular system, i.e., resonance fluorescence (RF). These techniques include analyzing the interference between RF and the incident laser itself as a function of polarization, analyzing the time correlation function $g^{(2)}(t)$ using a Hanbury Brown–Twiss setup, measuring with an interferometer the mutual phase coherence between the coherently

scattered light and a local oscillator, or analyzing the frequency spectrum using a high-finesse scanning Fabry–Perot interferometer [5–8]. Additionally, the phase shift of transmitted light through a cavity with a strongly coupled atom can be determined using a heterodyne setup [9].

Recently, such techniques have been extended to also study QDs in solid-state systems [10–13] and to measure the quantum phase shift induced by a coupled QD-cavity system by analyzing the reflection intensity as a function of output polarization [14], or by interfering light reflected from the QD-cavity system with light reflected from another piece of the sample [15]. In this Letter, we present a homodyne detection technique that enables simultaneous measurement of both coherence and induced phase shift. The technique is relatively straightforward as it requires only one scanning laser and it is mostly fiber-based. It provides complete coherence and phase information as a function of scanning laser detuning.

The setup for the homodyne interference technique is schematically displayed in Fig. 1(a). Light from a scanning laser is first split into two paths with a fiber beam splitter (FBS). One path (with intensity $I_1 \propto |E_1|^2$) is transmitted through the QD-cavity system, while the other path ($I_2 \propto |E_2|^2$) is used as the local oscillator. The two signals are combined using a FBS and the interference signal ($I \propto |E_1 + E_2|^2$) is recorded. The sample under study is an oxide-apertured micropillar with embedded InAs self-assembled QDs, a system that combines QD charge and energy control, access to the intermediate coupling regime, and polarization degenerate cavity modes [16–21]. Access to the full polarization degree of freedom enables us to use free-space polarizing optics (Pol1 and Pol2) to set the input and output polarizations. These are either set to be parallel, or the output is set at orthogonal crossed polarization; we use a combination of a quarter-wave plate and a polarizer to compensate for the small amount of birefringence present in the sample. To match the local oscillator polarization (Pol3) to the output polarization (Pol2), we use a coiled fiber polarization controller. In our setup there is no need for active stabilization and a single scan is recorded in typically a couple of seconds.
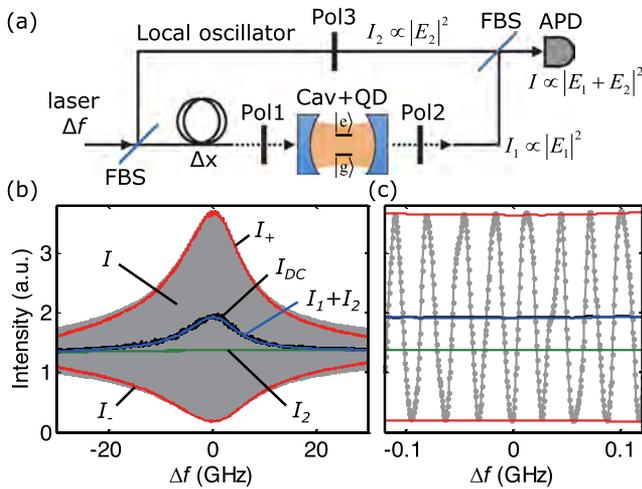
Fig. 1. Demonstration of the homodyne interference technique. (a) Schematic of the setup. Coherent light from a scanning laser is split using a fiber beam splitter (FBS), transmitted through the QD-cavity system, recombined with the local oscillator on a FBS and recorded with a avalanche photodiode (APD). Pol, polarization controlling optics. Pol3 is always set to match Pol2. (b) Signal for an empty cavity as function of scanning laser frequency detuning. Gray: interference signal I when combing the local oscillator and the cavity signal. Black: DC component. Green: I_2 reference signal. Blue: predicted DC signal from the sum $I_1 + I_2$. Red: predicted envelope of the interference signal for full interference (see text for details). (c) Zoom-in around zero detuning.

The signal after transmission through the sample is given by $E_1(t) = E_1 \exp(i\omega t + i2\pi\frac{\Delta x}{c}\Delta f + i\phi(\Delta f, t))$, where ω is the angular frequency, Δf is the laser frequency detuning, $\Delta x \approx 10$ m is the optical path length difference between the two interferometer arms, c is the speed of light, $\phi(\Delta f, t)$ is the phase shift induced by the QD-cavity system, and E_1 is the transmission amplitude of the cavity. When this signal is combined with the local oscillator $E_2(t) = E_2 e^{i\omega t}$, the resulting interference intensity I is given by

$$I = I_1 + I_2 + 2\sqrt{I_1 I_2} \cos\left(2\pi\frac{\Delta x}{c}\Delta f + \phi(\Delta f, t)\right). \quad (1)$$

When the transmitted light is coherent, i.e., $\phi(\Delta f, t) = \phi(\Delta f)$ does not vary in time, I contains interference oscillations that are bounded by $I_\pm = I_1 + I_2 \pm 2\sqrt{I_1 I_2}$. In the case of incoherent light, which can be interpreted as a rapidly varying phase $\phi(\Delta f, t)$, no interference is present and $I = I_1 + I_2$.

In Figs. 1(b) and 1(c) we show the case for an empty cavity, where the transmitted light naturally remains fully coherent. Also the polarization is not modified, and we set Pol2 parallel to Pol1 and use a large intensity ~10 μW that is recorded with a fast photodiode instead of an avalanche photodiode. First, we record the reference signal I_2 (green curve) and the transmitted intensity I_1 (not shown) separately; this enables us to predict the DC signal $I_1 + I_2$ (blue curve) and the interference envelope $I_\pm = I_1 + I_2 \pm 2\sqrt{I_1 I_2}$ (two red curves). The gray curve shows the measured interference signal I. By low-pass filtering we obtain the DC signal I_{DC} (black curve) that agrees

well with $I_1 + I_2$. The envelope of I agrees nicely with the independently measured calculated envelopes (red curves), which is especially clear in the zoom-in around the cavity resonance in Fig. 1(c). It is worth pointing out that, even though $I_1/I_2 \simeq 0.3$, the ratio of the maxima and minima of the interference fringes is much larger: $I_+/I_- \simeq 12$. This demonstrates the beauty of interference and the strength of the technique to measure the coherence of the transmitted light.

We now investigate the coherence properties of light scattered by a charge neutral QD. The lowest excited states of a neutral QD are split in energy, due to electron–hole interaction arising from QD anisotropy, and couple through orthogonally linear polarized transitions with the ground state in a V-type system, as is shown in the inset in Fig. 2(a). We prepare the input polarization at 45° with respect to the polarizations of both transitions such that scattered light, with a polarization of 0° or 90°, passes through the crossed polarizer set to –45°; while the cavity background transmission, of which the polarization is unchanged, is filtered out.

Figure 2(a) shows the light scattered by the two transitions for various intensities. First I_1 and I_2 are recorded separately and $I_1 + I_2$ (blue lines) and the envelope I_+ and I_- (two red lines) are calculated. The interference signal I is shown in gray and the low-pass filtered signal I_{DC} is shown by the black line, which follows the blue line. The interference signal I was Fourier-filtered with a bandpass filter centered at the oscillation frequency to remove some noise. Figure 2(b) shows a zoom-in of the 500 pW scan around the low-frequency transition. A clear oscillation signal is visible, with a coherent fraction, defined as the ratio $F = (I_{\max} - I_{\min})/(I_+ - I_-)$, where $I_{\max}$ and $I_{\min}$ are the upper and lower bounds of the interference envelope, of about 0.6. This indicates that the scattered light is only partially coherent.

To investigate this further, we show in Fig. 2(c) the calculated coherent fraction as a function of the laser detuning for various intensities. For a low power of 30 pW it can be seen that the scattered light coherence is about 0.7, but this decreases for increasing intensities. An additional structure of dips in the curve of the coherent fraction becomes visible. This shows that the coherence decreases more rapidly at the QD resonances (marked by the blue vertical lines), compared to the detuned case (the green vertical line marks the center between the two transitions) due to the less efficient off-resonant driving. We note that for increasing power the QD line shapes become distorted and the fine splitting between transitions becomes smaller, due to a dynamical charging effect as is explained in [22].

To analyze this power-dependency, we plot in Figure 2(d) the coherent fraction at the resonance and off the resonance of a QD transition as a function of the laser power. The fraction F of the scattered light that remains coherent follows the relationship [23]

$$F = \frac{\gamma_\parallel/\gamma_\perp}{1 + (P/P_o)/(1 + \Delta'^2)}, \quad (2)$$

where $\gamma_\parallel$ and $\gamma_\perp$ denote the population relaxation rate and the homogeneous dephasing rate, respectively, P is the laser power, P_0 is the saturation power, and Δ' is the detuning with respect to the QD linewidth. The scattered light is almost fully
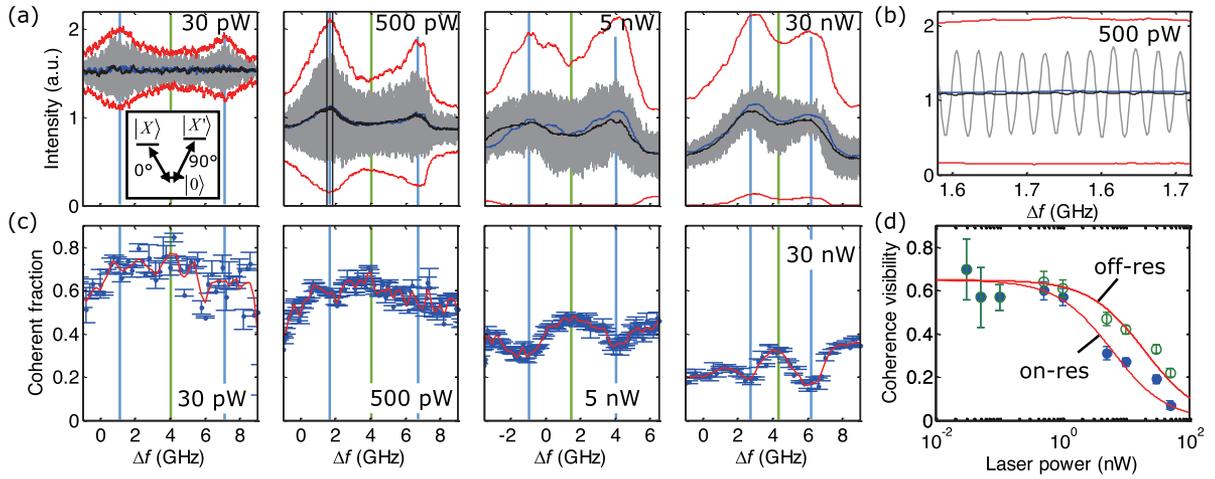
Fig. 2. Coherence of the scattered light by a QD as function of laser cavity detuning and injected power. (a) Scans for various laser powers. The input polarization was set to 45° and transmission was recorded through a crossed polarizer such that only the two fine-split QD transitions, see inset for a schematic, and not the cavity are visible. The five curves show: I (gray), I_{DC} (black), $I_1 + I_2$ (blue), I_+ and I_- (red 2×). (b) Zoom-in of the 500 pW scan in (a). (c) Coherent fraction determined as the ratio $F = (I_{max} - I_{min})/(I_+ - I_-)$. (d) Coherent fraction as function of laser power determined on the resonance of a QD transition [blue vertical lines in (a),(c)] and off resonance (green vertical lines). Red lines are predicted curves using Eq. ([2]).

coherent if the used power is small and $\gamma_\parallel \approx \gamma_\perp$, i.e., the pure dephasing is small. For increasing power the coherent fraction decreases as the QD excited-state population builds up and incoherent emission increases. For frequencies detuned from the QD resonance the effective driving rate becomes smaller and the effect gets reduced. We show theoretical curves for $\gamma_\parallel/\gamma_\perp = 0.65$, $P_0 = 6$ nW, and $\Delta' = 0$ and $\Delta' = 1.5$ for the on-resonance and off-resonance cases, which match the data well and demonstrate the nonlinear QD saturation dynamics. The mean intracavity photon number $\langle \bar{n} \rangle$ is given by $\langle \bar{n} \rangle = P_{out}/\kappa_m \hbar \omega$, where $\kappa_m \approx 11$ ns^{-1} is the mirror loss rate, and the maximum output intensity $P_{out} = |t|^2 P$ is a function of the maximum transmittivity $|t|^2 \approx 0.09$ and incident power P. A saturation power of $P_0 = 6$ nW corresponds to a mean intracavity photon number $\langle \bar{n} \rangle \approx 0.2$, and sounds reasonable compared to other work with efficient coupling to a single emitter [8]. The direct observation that $\gamma_\parallel/\gamma_\perp = 0.65$ indicates that the QD line shape is not only lifetime limited and that additional pure dephasing, such as spectral fluctuations or coupling to phonons, plays a role.

We now turn in Fig. [3] to a negatively charged QD that suffers from decoherence. We use a linear input polarization such that only the light scattered by the circularly polarized QD transitions passes through the crossed output polarizer. In Fig. [3(a)] we show $I_1 + I_2$ (blue line) and the predicted envelope I_+ and I_- (red lines). The interference signal I (gray line) now hardly shows oscillations. The calculated coherent fraction, shown by the blue curve in Fig. [3(b)], is less than 5%. This implies that $\gamma_\parallel/\gamma_\perp \ll 1$ and that the QD suffers from fast decoherence. The green curve in Fig. [3(b)] displays the transmitted intensity I_1; showing the red detuned QD, and part of the cavity line shape due to the dispersive effect of the QD coupled to it.

The strong incoherent behavior was previously also investigated through high-resolution spectral and polarization

resolved studies in [21]. Here among others a larger homogeneous dephasing rate $\gamma_\perp$ and smaller cooperativity C were observed for the charged QDs compared to the charge neutral ones. The findings are attributed to a fast cotunneling process of electrons across the very small (20 nm) tunnel barrier that separates the QD from a n-doped contact region. Our technique therefore serves as a powerful QD characterization technique which will help to characterize future sample improvements, such as utilizing a thicker tunnel barrier.

Finally, we show that from the obtained data we can also derive the quantum phase shift induced by a single QD transition coupled to a cavity, which forms a hallmark in cavity quantum electrodynamics (QED) experiments [9,14,15,24]. This phase shift $\phi(\Delta f)$, see Eq. ([1]), can easily be extracted from the interference signal by analyzing the oscillation in a rotating frame, which we realize in practice by multiplying
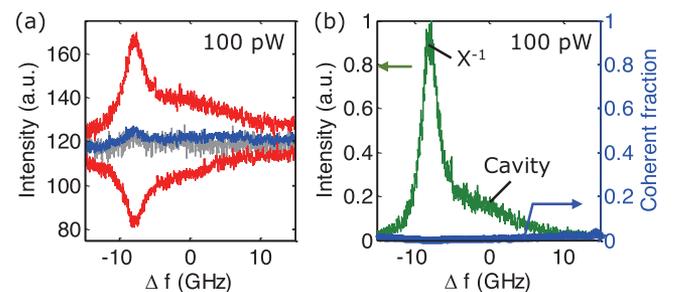
Fig. 3. Incoherent scattered light from a singly charged QD (X^{1-}) that suffers from fast decoherence. A linear input and a crossed output polarization is used such that only light scattered by the circularly polarized QD transitions is detected. (a) Shows the interference signal I (gray), $I_1 + I_2$ (blue), and I_+ and I_- (red lines). (b) Cross-polarized transmitted intensity I_1 of the QD-cavity system (green) and the determined coherence visibility (blue), showing that the scattered light is nearly fully incoherent ($F < 0.05$).
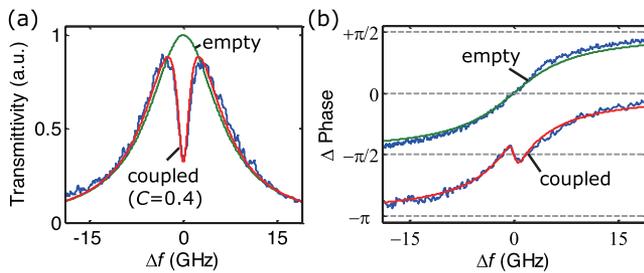
Fig. 4.   Phase shift induced by a QD-cavity system. (a) shows the transmitted intensity I_1 of a coupled QD-cavity system recorded at $P_{\text{laser}} = 10$ pW. (b) shows the phase shift for an empty cavity for $P_{\text{laser}} = 10$ μW (upper curve) and a coupled system for $P_{\text{laser}} = 10$ pW (lower curve). The lower curve is displaced for clarity. Red lines in (a) and (b) are predicted curves for QD cooperativity $C = 0.4$ [21,25–27], QD dephasing rate $\gamma_\perp = 4$ ns^{-1}, and cavity total loss rate $\kappa = 80$ ns^{-1}. Green curves in (a) and (b) are predicted lines for an empty cavity.

the signal with a complex exponent $\exp(i2\pi \frac{\Delta x}{c} \Delta f)$ and applying a DC filter. We switch back to a neutral QD and set the input polarization to match one of the fine-split transitions and now record the transmission with a parallel polarization. In Fig. 4(a) we display the transmitted intensity I_1, showing the QD feature appearing as a dip in the otherwise Lorentzian cavity line shape. Figure 4(b) shows the phase shift induced by an empty cavity and by a coupled QD-cavity system. The red and green curves are calculated based on a cavity QED model with no additional fit parameters [21,26,27], and agree nicely with the data.

In conclusion, we have presented a technique that enables determination of the coherence and the phase of light that is transmitted through a coupled QD-cavity system. The method is simple as it is mostly fiber-based and requires only one scanning laser and standard photodiode detectors. Good signal-to-noise ratio is readily obtained by making the interferometer path difference long using fiber optics; this leads to a high fringe frequency, which relaxes stability requirements strongly. Other methods require movable elements [13], Fabry–Perot interferometers [11–13], single-photon detection [11,12], or multibeam setups [28]. However, our technique relies on polarization-degenerate cavities enabling cross-polarized detection to access exclusively the light scattered by the QD. This technique is important for QD characterization and for fundamental tests of cavity QED.

REFERENCES

1. R. J. Warburton, Nat. Mater. **12**, 483 (2013).
2. C. Bonato, F. Haupt, S. S. R. Oemrawsingh, J. Gudat, D. Ding, M. P. van Exter, and D. Bouwmeester, Phys. Rev. Lett. **104**, 160503 (2010).
3. C. Y. Hu, W. J. Munro, and J. G. Rarity, Phys. Rev. B **78**, 125318 (2008).
4. H. J. Kimble, Nature **453**, 1023 (2008).
5. H. J. Kimble, M. Dagenais, and L. Mandel, Phys. Rev. Lett. **39**, 691 (1977).
6. T. Basché, W. E. Moerner, M. Orrit, and H. Talon, Phys. Rev. Lett. **69**, 1516 (1992).
7. T. Plakhotnik and V. Palm, Phys. Rev. Lett. **87**, 183602 (2001).
8. G. Wrigge, I. Gerhardt, J. Hwang, G. Zumofen, and V. Sandoghdar, Nat. Phys. **4**, 60 (2008).
9. Q. A. Turchette, C. J. Hood, W. Lange, H. Mabuchi, and H. J. Kimble, Phys. Rev. Lett. **75**, 4710 (1995).
10. A. Muller, E. B. Flagg, P. Bianucci, X. Y. Wang, D. G. Deppe, W. Ma, J. Zhang, G. J. Salamo, M. Xiao, and C. K. Shih, Phys. Rev. Lett. **99**, 187402 (2007).
11. A. Nick Vamivakas, Y. Zhao, C.-Y. Lu, and M. Atature, Nat. Phys. **5**, 198 (2009).
12. E. B. Flagg, A. Muller, J. W. Robertson, S. Founta, D. G. Deppe, M. Xiao, W. Ma, G. J. Salamo, and C. K. Shih, Nat. Phys. **5**, 203 (2009).
13. K. Konthasinghe, J. Walker, M. Peiris, C. K. Shih, Y. Yu, M. F. Li, J. F. He, L. J. Wang, H. Q. Ni, Z. C. Niu, and A. Muller, Phys. Rev. B **85**, 235315 (2012).
14. I. Fushman, D. Englund, A. Faraon, N. Stoltz, P. Petroff, and J. Vučković, Science **320**, 769 (2008).
15. A. B. Young, R. Oulton, C. Y. Hu, A. C. T. Thijssen, C. Schneider, S. Reitzenstein, M. Kamp, S. Höfling, L. Worschech, A. Forchel, and J. G. Rarity, Phys. Rev. A **84**, 011803 (2011).
16. N. G. Stoltz, M. Rakher, S. Strauf, A. Badolato, D. D. Lofgreen, P. M. Petroff, L. A. Coldren, and D. Bouwmeester, Appl. Phys. Lett. **87**, 031105 (2005).
17. S. Strauf, N. G. Stoltz, M. T. Rakher, L. A. Coldren, P. M. Petroff, and D. Bouwmeester, Nat. Photonics **1**, 704 (2007).
18. M. T. Rakher, N. G. Stoltz, L. A. Coldren, P. M. Petroff, and D. Bouwmeester, Phys. Rev. Lett. **102**, 097403 (2009).
19. C. Bonato, D. Ding, J. Gudat, S. Thon, H. Kim, P. M. Petroff, M. P. van Exter, and D. Bouwmeester, Appl. Phys. Lett. **95**, 251104 (2009).
20. M. P. Bakker, A. V. Barve, A. Zhan, L. A. Coldren, M. P. van Exter, and D. Bouwmeester, Appl. Phys. Lett. **104**, 151109 (2014).
21. M. P. Bakker, A. V. Barve, T. Ruytenberg, W. Löffler, L. A. Coldren, D. Bouwmeester, and M. P. van Exter, Phys. Rev. B **91**, 115319 (2015).
22. M. P. Bakker, T. Ruytenberg, W. Löffler, A. V. Barve, L. Coldren, M. P. van Exter, and D. Bouwmeester, "Quantum dot nonlinearity through cavity-enhanced feedback with a charge memory," arXiv:1503.08142 (2015).
23. R. Loudon, *The Quantum Theory of Light (Oxford Science Publications)*, 3rd ed. (Oxford University, 2000).
24. C. Sames, H. Chibani, C. Hamsen, A. Altin, P. T. Wilk, and G. Rempe, Phys. Rev. Lett. **112**, 043601 (2014).
25. V. Loo, C. Arnold, O. Gazzano, A. Lemaître, I. Sagnes, O. Krebs, P. Voisin, P. Senellart, and L. Lanco, Phys. Rev. Lett. **109**, 166806 (2012).
26. A. Auffèves-Garnier, C. Simon, J.-M. Gérard, and J.-P. Poizat, Phys. Rev. A **75**, 053823 (2007).
27. E. Waks and J. Vuckovic, Phys. Rev. Lett. **96**, 153601 (2006).
28. F. Masia, N. Accanto, W. Langbein, and P. Borri, Phys. Rev. Lett. **108**, 087401 (2012).

Quantum dot nonlinearity through cavity-enhanced feedback with a charge memory

Morten P. Bakker,[1] Thomas Ruytenberg,[1] Wolfgang Löffler,[1] Ajit
Barve,[2] Larry Coldren,[2] Martin P. van Exter,[1] and Dirk Bouwmeester[1, 2]

[1]*Huygens-Kamerlingh Onnes Laboratory, Leiden University,
P.O. Box 9504, 2300 RA Leiden, The Netherlands*
[2]*University of California Santa Barbara, Santa Barbara, California 93106, USA*
(Dated: March 30, 2015)

In an oxide apertured quantum dot (QD) micropillar cavity-QED system, we found strong QD hysteresis effects and lineshape modifications even at very low intensities corresponding to $< 10^{-3}$ intracavity photons. We attribute this to the excitation of charges by the intracavity field; charges that get trapped at the oxide aperture, where they screen the internal electric field and blueshift the QD transition. This in turn strongly modulates light absorption by cavity QED effects, eventually leading to the observed hysteresis and lineshape modifications. The cavity also enables us to observe the QD dynamics in real time, and all experimental data agrees well with a power-law charging model. This effect can serve as a novel tuning mechanism for quantum dots.

Cavity quantum electrodynamics with quantum dots (QDs) coupled to microcavities enables various applications such as single-photon switches [1–5], generation of non-classical states of light [6–8] and hybrid quantum information schemes [9, 10]. However, QDs deviate from an ideal atom-like systems as they strongly interact with their environment, for example through nuclear spins [11, 12] and via charge traps [13, 14]. These interactions need to be understood and controlled in order to improve the QD coherence properties. For this purpose cavities are very useful to probe the QD environment, through increased light-matter interaction.

In this Letter we investigate such a QD-cavity system. For sufficiently low optical field intensity this system can be described by the QED of an effective 2-level system in a single-mode cavity. For increasing intensities we report on bistable and strong nonlinear behavior. The sample under study consists of InAs self-assembled QDs inside a PIN diode structure embedded in a micropillar. This system combines QD charge and Stark shift control by applying a bias voltage with high-quality polarization-degenerate cavity modes [15–19]. The mode confinement in the transversal direction is achieved by an oxide aperture formed through a wet oxidation step. The observed bistability and nonlinear behavior in the cavity QED system can be explained by attributing a second role to the oxide aperture, namely that of a charge memory. Charges in this memory, created by resonant absorption, will cause a modification to the applied bias voltage which in turn shifts the QD frequency, and modify the amount of absorption. In Figure 1 (a) the sample structure, with charges trapped at the oxide aperture, is schematically shown.

We consider one of the fine-split transitions of a charge neutral QD coupled to a polarization degenerate cavity mode in the intermediate coupling regime. Figure 1 (b) shows reflection spectra, recorded at a sufficiently low incident intensity $P_{in} = 1$ pW such that no nonlinear effects occur. Upward and downward frequency scans

overlap perfectly and can be fitted by theory for a dipole inside an optical cavity, which we will discuss later in detail. However, when a higher intensity of 1 nW is used, several strong deviations occur, see Fig. 1 (c). First of all, a hysteresis feature appears when the QD is tuned at or below the cavity resonance. Second, while at the
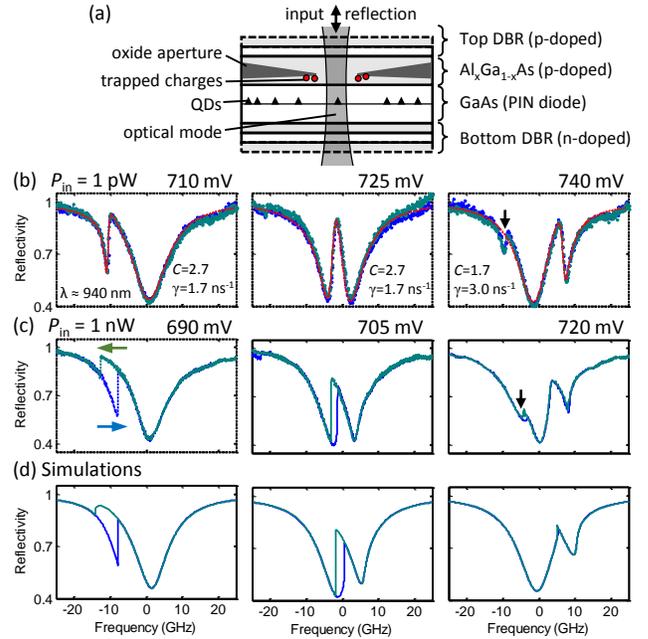
FIG. 1. (a) Schematic of the sample structure with charges trapped at the oxide aperture. Figure is not to scale and only a couple DBR pairs are shown. Resonant reflection spectroscopy scans recorded using laser intensities of (b) 1pW and (c) 1 nW for various applied bias voltages. Blue (green) curve: upward (downward) frequency scan. Red lines in (b) are fits using Eqn. 1 and reflectivity $R = |1 - t|^2$. The QD cooperativity C and dephasing rate γ obtained from the fits are named in the figures. The black arrows denote a second QD in the same cavity. Scans were taken on $\sim$s timescale. (d) presents simulations that predict the scans in (c).

high frequency side of the cavity resonance the hysteresis is much less, a line shape modification is still visible. Finally, in order to obtain the same QD detuning compared to the low intensity scans, a lower bias voltage has to be applied. After a thorough characterization of this effect, we present a model that explains all features as is shown in Fig. 1 (d).

A first hint on the underlying dynamics is provided by investigating the power dependence in single-laser scans. In Fig. 2 (a) we first keep the QD bias voltage constant and show scans for increasing laser intensity. A QD blueshift occurs, as is displayed in Fig. 2 (c). In a second set of measurements in Fig. 2 (b), we keep the QD-cavity detuning constant by changing the bias voltage as function of the laser intensity. A lower bias voltage has to be applied for increasing laser intensity, shown in Fig. 2 (d). Furthermore, the hysteresis width increases with intensity, see Fig. 2 (e), up to nearly 6 GHz, but then saturates and even decreases slightly when the intensity is above the QD saturation intensity (~ 2.5 nW). All three observations in Figs. 2 (c-e) obey the same empirical power-law $\propto P_{in}^{\beta}$, with $\beta = 0.35$. Already at an incident intensity $P_{in} = 11$ pW, corresponding to a maximum mean photon per cavity lifetime of $\langle \overline{n} \rangle \sim 4 \times 10^{-4}$,

a QD blueshift and line shape modification is clearly visible. Here the mean intracavity photon number is found from $\langle \overline{n} \rangle = P_{out}/\kappa_m \hbar \omega$, where $\kappa_m \sim 11$ ns^{-1} is the mirror loss rate, ω is the light angular frequency, and the maximum output intensity $P_{out} = |t|^2 P_{in} \sim 1$ pW (see below).

FIG. 3. Two-laser scans with resonant lasers. (a-c) Reflectivity color maps as function of the weak (1 pW) probe laser frequency and the second high intensity (1 nW) pump laser frequency for various applied bias voltages. The blue line shows the pump laser frequency compared to the probe laser. The arrows indicate the QD position. (d) Relative QD frequency shift as function of the pump laser-cavity detuning. The arrows denote where the laser is resonant with the QD. Gray dashed lines: Lorentzian function convoluted with the power-law from Fig. 2 (c) that have been added as a reference. Vertical offsets are added to the curves.

We now switch to a two-laser experiment (see Fig. 3) in order to further investigate the phenomenon that the QD blueshifts with increasing laser intensity. The QD transition is probed with a low intensity (1 pW) probe laser such that no line shape modification occurs. We then add a second high intensity (1 nW) pump laser with orthogonal polarization, such that it can be filtered out with a crossed polarizer in the detection channel. The pump laser is scanned in steps across the cavity resonance; for each step the QD-cavity spectrum is measured with the weak probe laser. Figure 3 (a-c) presents these measurements for various bias voltages such that the average QD-cavity detuning is varied. For every bias voltage the QD-cavity and pump laser-cavity detunings are determined, and the relative QD frequency as function of the pump laser-cavity detuning is shown in Fig. 3 (d). The maximum QD blueshift (of about 8 GHz) occurs when the pump laser is resonant with the cavity mode, corresponding to the vertical dashed line. An in-

FIG. 2. Characterization of the QD blueshift and nonlinearity. (a) Resonant reflection spectra for a fixed bias voltage and various intensities of the scanning laser. Blue (green): low to high (high to low) frequency scan. (b) Scans where the QD-cavity detuning is kept constant by varying the bias voltage for various laser intensities. (c) Relative QD shift (estimated from the vertical arrows in (a)), (d) applied bias voltage to keep the QD-cavity detuning constant (vertical dashed line in (b)), and (e) hysteresis width (horizontal arrow in (b)), all as function of the laser intensity. Red lines in (c,d,e) show empirical power-law fits. Vertical offsets have been added to the scans in (a,b).

creased blueshift also occurs when the pump laser is close to the QD frequency, indicated by the arrows in Fig. 3 (d), at which point the intracavity field also increases due to cavity QED effects. The gray dashed curves are Lorentzian lines convoluted with the $\propto P_{in}^{0.35}$ power-law from Fig. 2 (c) and correspond to the data nicely. In conclusion, the data clearly shows that the QD resonance blueshifts when the intracavity field increases, and this effect is independent of the QD-laser or the QD-cavity detuning.

We now introduce a model that explains the dynamic line shape modifications. We start from the transmission amplitude of a cavity with a coupled dipole [20, 21]:

$$t = \eta_{out} \frac{1}{1 - i\Delta + \frac{2C}{1 - i\Delta'}}, \qquad (1)$$

where $\Delta = 2(\omega - \omega_c)/\kappa$ is the relative detuning between the laser (ω) and cavity (ω_c) angular frequencies, C is the device cooperativity, $\Delta' = (\omega - \omega_{QD})/\gamma$ is the relative detuning between the laser and QD transition (ω_{QD}), η_{out} is the output coupling efficiency, κ is the total intensity damping rate of the cavity and γ is the QD dephasing rate. We obtain close to perfect mode-matching, and therefore the total transmittivity through the cavity is given by $T = |t|^2$, and the total reflectivity is given by $R = |1 - t|^2$. In Fig. 1 (a) we show that the model fits the low intensity measurements very well. The QD cooperativity and dephasing parameters C and γ are noted in the subfigure windows, and a cavity damping rate $\kappa \sim 77$ ns^{-1} and an output coupling efficiency $\eta_{out} = 2\kappa_m/\kappa \sim 0.3$ is found, corresponding to a cavity Q-factor of $Q \sim 2.6 \times 10^4$.

As a next step, we introduce a QD frequency $f_{QD} = \omega_{QD}/2\pi$ that dynamically changes with the intracavity intensity, which is proportional to $|t|^2$:

$$f_{QD} = f_0 + \alpha |t|^{2\beta}, \qquad (2)$$

where f_0 equals the QD frequency in the limit of vanishing intracavity intensity. Based on the empirical values determined in Fig. 2 (c), we use $\alpha = 1.5 \times (P_{in}/\eta_{out}^2)^\beta$ GHz, with P_{in} in pW, and $\beta = 0.35$. Due to cavity QED effects, the intracavity field depends strongly on the QD frequency such that the cavity can change from being largely transparent to being largely reflective through only small changes in the QD frequency. This interplay leads to the observed nonlinear behaviour.

Finally, we take into account that we are operating the QD–cavity system close to the saturation intensity, which slightly suppresses the QD features. We take this into account by calculating the reflectivity R' by taking the weighted sum of the reflectivities of a coupled (R) and uncoupled (R_0) cavity: $R' = xR + (1 - x)R_0$, with $x = 0.8$. This is a strong simplification of a more rigorous approach based on the quantum master equation and

calculation of the intracavity photon number [4], but is sufficient for our purpose. For QD cooperativity C and dephasing rate γ we use the values obtained in the fits in Fig. 1 (a). Figure 1 (c) shows that the predicted scans match the actual measurements very well.

As the underlying physical mechanism we hypothesize that charges are excited by the resonant laser and get trapped at the oxide aperture. Reasonably high doping concentrations were used, up to 6×10^{18} cm^{-3} for the carbon p-doped layers and up to 5×10^{18} cm^{-3} for the silicon n-doped layers, and it is well-known that absorption takes place in these doped layers [22], resulting in a non-neglible photocurrent (see the Supplemental Material section I [33]). The excited charges partly screen the internal electric field responsible for the quantum confined stark effect in the QD, leading to the observed blueshift of the QD transitions.

Furthermore, the fact that even for a very low cavity mean photon number of ~ 0.001 ($P_{in} = 11$ pW) non-linearities take place, indicates that the oxide aperture must form an efficient charge memory compared to the QD-cavity decay rate (77 ns^{-1}). It is well known that the interface between GaAs and aluminum oxide (AlO$_x$), produced by wet oxidation of AlAs, provides a very high density of charge traps, in the form of amorphous oxide and micro crystallites [23], and in the form of elemental interfacial As [24], leading to spatially non-uniform Fermi level pinning [25]. The time-resolved charge decay measurements presented below confirm that the charges are relatively long-lived on a ~ 10 ms timescale. Also, a comparison with QDs observed outside of the oxide aperture region show that laser induced blueshift is neglible in these regions (see Supplemental Material section II [33]). Furthermore, the charging hypothesis agrees with the observed $\propto P^{0.35}$ sublinear power-law, which would be the consequence of Coulomb repulsion between trapped charges, possibly in combination with increased filling of trap states that have an increasing decay rate.

Our results agree with observations in Ref. [13], where single–charge fluctuations are probed at a GaAs/AlAs interface located about 50 nm away from the QDs, while a gradual variation was observed for charge traps more than 150 nm away. We did not observe any single–charge influences as the distance between the QDs and the oxide aperture is about 200 nm in our sample. In contrast to our work, the GaAs/AlAs interface studied in Ref. [13] is located in the intrinsic region, while the aperture in our sample is located in the p-doped region, but a similar QD blueshift for increasing laser intensity and constant bias voltage was observed.

Finally, we performed a set of measurements to gain insight in the temporal dynamics of the charge build-up and decay. For this purpose we use a laser ($\lambda = 852$ nm) that is off-resonant with the cavity but is resonant with the wetting layer. At a larger laser intensity, more charges are excited compared to the resonant laser and
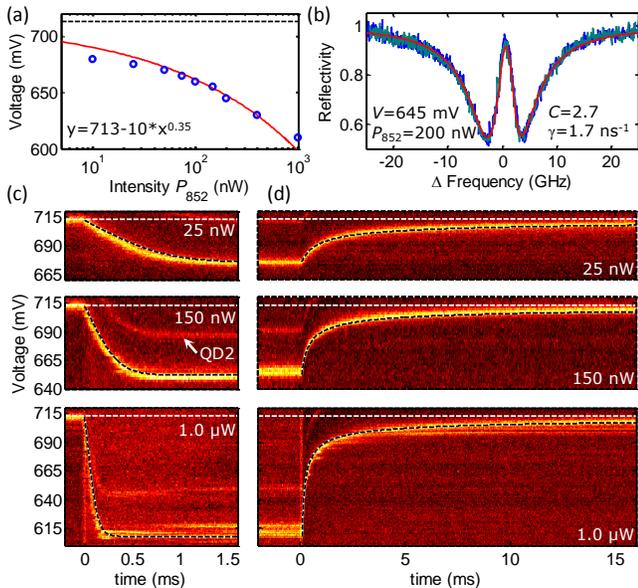
FIG. 4. Two-laser scans with an off-resonant ($\lambda = 852$ nm) laser. (a) shows the bias voltage where the QD transition is resonant with the cavity mode, as function of the intensity P_{852} of the off-resonant laser. The black dashed line indicates the QD bias voltage when no off-resonant laser is applied. (b) Example of resonant reflection scans using a weak (1 pW) probe laser, recorded in the presence of an off-resonant laser. Text in the figures denotes the applied bias voltage V, intensity P_{852}, and QD cooperativity C and dephasing rate γ of the predicted red line. (c,d) Colormaps of the reflected intensity of the probe laser fixed to the center of the cavity resonance (light/dark: high/low signal, corresponding to an on(off) resonant QD), as function of the time and applied bias voltage, for various off-resonant pump intensities. The off-resonant laser is turned on (c) and off (d) at $t = 0$ ms. The red line in (a) and the black-white dashed in (c,d) are reproduced using the same parameters (see main text for explanation). Note that the time axes of (c,d) are different.

larger QD shifts can be obtained. We now use the coupled QD-cavity system as a very sensitive probe of the internal electric field, a principle that was also used to monitor a single charge trap in real-time [26].

Figure 4 (a) shows, for various off-resonant pump laser intensities, the bias voltage that has to be applied to tune the QD to the cavity resonance, determined by using a weak (∼1 pW) resonant probe laser. Again, as in Fig. 2 (d), a clear sub-linear behavior $\propto P_{in}^{\beta}$ is visible. At an even higher intensity of 100 μW, a bias voltage of 350 mV had to be applied to tune the QD in to resonance, clearly indicating that the charge buildup and QD blueshift is not easily saturated. Strikingly, even for an excitation power of 200 nW, the QD has the same cooperativity C and dephasing rate γ as when no off-resonant laser is present, see Fig. 4 (b). This indicates that, even though many charges are excited, they are located relatively far away and give rise to a more-or-less constant effective

electric field, thereby preserving the QD coherence.

In order to directly monitor the time dynamics of the charge buildup and decay, we fix a weak probe laser that will not excite any additional charges at the cavity resonance, and monitor the reflectivity as function of bias voltage and time. Figure 4 (c) shows, for various off-resonant pump laser intensities, reflectivity colormaps of the probe laser when the off-resonant pump laser is turned on at $t = 0$ ms. For $t < 0$ ms, the QD is resonant with the cavity resonance at $V = 713$ mV (white dashed lines), corresponding with a high probe laser reflectivity at this voltage and a low reflectivity at different voltages. The reflectivity at $V = 713$ mV abruptly decreases as the pump laser is turned on, but is then restored at lower bias voltages, demonstrating direct probing of the charge build-up. For increasing pump laser intensities, the reflectivity is restored at a lower voltage, but also the time for the charge build-up to reach an equilibrium decreases.

The decay of the charges is monitored in Fig. 4 (d), where the pump laser is turned off at $t = 0$ ms. For $t < 0$ ms the QD reflectivity signal is now highest for a low bias voltage when the charge reservoir is saturated. After the pump is turned off and the charges disappear, the reflectivity now gets restored at an increasing bias voltage. The charge decay rate is initially fastest, when many charges are still present and the QD is resonant at a lower bias voltage, but then strongly decreases and finally occurs on a ∼10 ms timescale, much slower than the charge build-up rate.

We now introduce a simple power-law model to describe the charge build-up and decay dynamics. We assume that the QD voltage shift ΔV is proportional to the number of trapped charges Q, and increases as a function of the pump laser intensity P, such that $\Delta V = -Q = -\Gamma P^{\beta}$. As a result, the charge decay and buildup is described using: $\frac{dQ}{dt} = P - (Q/\Gamma)^{1/\beta}$. The red line in Fig. 4 (b) and the white-black dashed lines Fig. 4 (c-d) are reproduced with $\Gamma = 10$ and the same power-law scaling factor $\beta = 0.35$ as found earlier, and describe the data nicely.

The effect we found enables a novel method to tune QD transitions without the need for electrical contacts, or enable independent tuning of QDs sharing the same voltage contacts. Furthermore it could serve as a low power all-optical switch mediated by a charge memory. The cavity-enhanced feedback mechanism with the charge environment could in principle also occur in other solid-state microcavity structures, where doped layers are present in which charges can be excited and where material defects or interfaces could act as a charge trap. This interaction therefore also has to be taken into account when studying dynamical nuclear spin polarization (DNP) effects in a cavity, which is of general interest to prolong the QD coherence time and the potential to form a quantum memory. DNP gives rise to QD line shape modifications,

hysteresis and bistability behavior [11, 27–32]; phenomena that could also give rise to cavity-enhanced feedback mechanisms.

In conclusion, we have studied a neutral QD transition coupled to a microcavity and observed strong cavity-enhanced feedback with the charge environment. Hysteresis and modifications of the QD line shape are demonstrated at intensities of way less than 1 photon per cavity lifetime, which we explain and model by a QD frequency blueshift attributed to charges trapped at the oxide aperture as a function of the intracavity field. In general, these results demonstrate the potential of studying and controlling the QD environment using a cavity QED system.

APPENDIX

In this Supplemental Material we will first present photocurrent measurements. To confirm that a $\lambda \sim 940$ nm resonant laser excites charges in the cavity region, we compare the photocurrent with when a $\lambda = 852$ nm off-resonant laser is used. Then we compare photoluminescence data with and without the presence of an aperture, to demonstrate that the oxide aperture plays an important role in trapping the charges,. These observations support our claim that the mechanism behind the observed nonlinear effects in the resonant QD scans, is the excitation of charges that are trapped by the oxide aperture.

I. Photocurrent measurements

Current as function of bias voltage was measured without (dark) and with the presence of a $\lambda = 852$ nm or a $\lambda \sim 940$ nm laser, see Fig. 5 (a). The $\lambda \sim 940$ nm laser frequency was locked at the cavity resonance, such that the absorption is increased due to the high finesse ($\sim 2 \times 10^3$) of the cavity, as is the case during the resonant scans in the main text. When no additional pump laser is applied, a current flows through the device in the same direction as that the forward bias voltage is applied, giving rise to an IV-curve that is typical for a PIN diode device. In the presence of an additional pump laser charges are now optically excited and flow in the opposite direction due to the internal field being present, giving rise to an additional negative photocurrent. In Fig. 5 (b) we compare the absolute value of the photocurrent produced by the $\lambda \sim 940$ nm and $\lambda = 852$ nm laser, normalized by the pump laser intensity. For both lasers a strong bias voltage dependency is visible and the collected photocurrent is smaller at a larger bias voltage,

which is closer to the flatband regime. This indicates that either the absorption, or the collection efficiency of the excited charges, is voltage dependent. The 940 nm laser gives rise to a photocurrent of about 0.5 mA/W at a bias voltage of 700 mV where charge neutral QDs are typically operated, which at an intensity of 1 nW corresponds to about 3×10^6 charges being excited and collected per second.
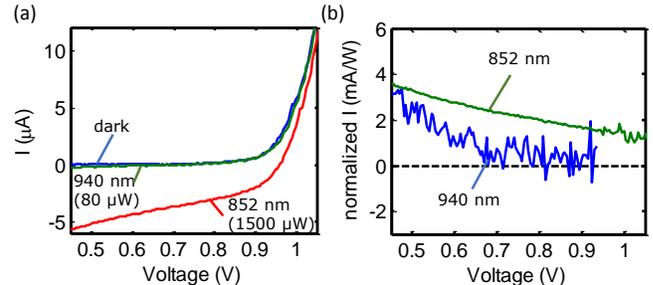
FIG. 5. (a) The current through the sample as function of the applied bias voltage without (dark) and with the presence of a 852 nm or ~ 940 nm laser. The 940 nm laser was locked at the microcavity resonance. The used intensity is mentioned between brackets.(b) Difference between the current when no laser and when an 852 nm or 940 nm laser is present, normalized by the input laser intensity.

II. Photoluminescence measurements

Next, we compare the photoluminescence collected from the oxide-aperture microcavity and from a region with an unbalanced cavity. In the unbalanced cavity region the top DBR has been nearly completely etched away, in order to enhance the collection efficiency, and no oxide aperture has been applied. Figure 6 (a,c) present colormaps of the PL spectra as a function of applied bias voltage and collected wavelength, using a $\lambda = 852$ nm pump laser of various intensities. Figure 6 (b) shows the PL intensity as function of voltage at the cavity resonance. Single QD lines (marked by the arrows) are hardly distinguishable from the background cavity emission, which originates from broadband wetting layer emission. For increasing pump laser intensity, it is clearly visible that the QD lines appear at a lower bias voltage. For the QDs in the region without an oxide aperture, the shift in voltage is however much smaller. The QDs in Fig. 6 (c) are now better visible, even though at high pump laser intensities for increasing voltage again broadband emission 'washes out' clear QD signatures. Figure 6 (d) presents the mean PL counts for various pump intensities. A shoulder is visible, which corresponds with the voltage range where the QDs are on average charge neutral. The shoulder does shift to a lower voltage range, but the shift (in total ~ 50 mV for 1100 μW) is much smaller compared to the total ~ 700 mV (for 1500 μW)

voltage shift of the QDs in the microcavity. Even though it is likely that roughly the same amount of charges are excited by the $\lambda = 852$ nm laser in the microcavity region compared to elsewhere in the sample, these results indicate that the oxide aperture provides a charge memory, causing a much larger effective charge buildup resulting in a larger voltage shift of the QDs.
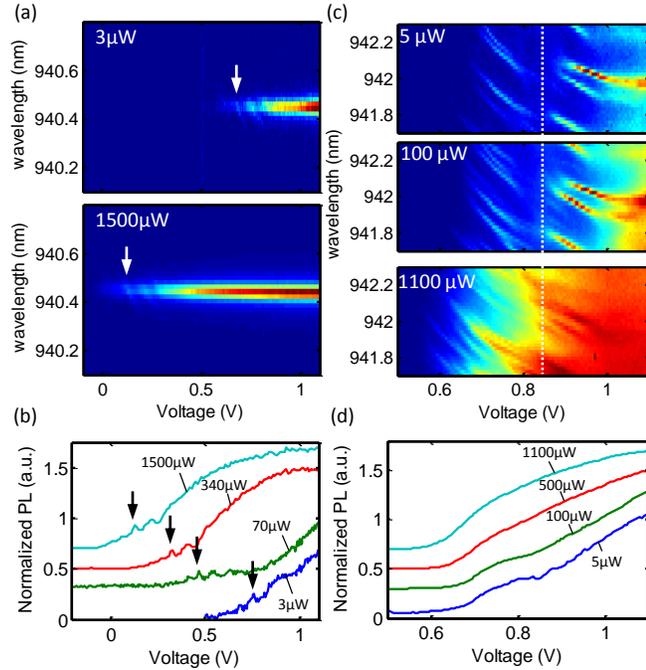
FIG. 6. Photoluminescence (PL) colormaps as function of the applied bias voltage and collection wavelength recorded at (a) the microcavity, and (c) from an unbalanced planar cavity. The intensity of the ($\lambda = 852$ nm) pump laser is indicated in the top left corner of the figures. (b) PL intensity as function of bias voltage at the cavity resonance, for various pump laser intensities. The vertical arrows in (a, b) denotes the same QD peak. (d) average PL intensity as function of voltage collected from the unbalanced planar cavity. The white dashed vertical line serves as a reference. An offset has been added between the curves in (b, d).

[1] D. E. Chang, A. S. Sorensen, E. A. Demler, and M. D. Lukin, *Nat Phys*, Nature Physics **3**, 807 (2007).

[2] D. Englund, A. Majumdar, M. Bajcsy, A. Faraon, P. Petroff, and J. Vučković, Physical Review Letters **108**, 093604+ (2012).

[3] R. Bose, D. Sridharan, H. Kim, G. S. Solomon, and E. Waks, Physical review letters **108** (2012).

[4] V. Loo, C. Arnold, O. Gazzano, A. Lemaître, I. Sagnes, O. Krebs, P. Voisin, P. Senellart, and L. Lanco, Phys. Rev. Lett. **109**, 166806 (2012).

[5] T. Volz, A. Reinhard, M. Winger, A. Badolato, K. J. Hennessy, E. L. Hu, and A. Imamoglu, Nat Photon **6**, 605 (2012).

[6] I. Fushman, D. Englund, A. Faraon, N. Stoltz, P. Petroff, and J. Vučković, Science **320**, 769 (2008).

[7] C. S. Munoz, E. del Valle, A. G. Tudela, K. Muller, S. Lichtmannecker, M. Kaniber, C. Tejedor, J. J. Finley, and F. P. Laussy, Nat Photon **8**, 550 (2014).

[8] A. Majumdar, M. Bajcsy, A. Rundquist, and J. Vučković, Phys. Rev. Lett. **108**, 183601 (2012).

[9] H. J. Kimble, Nature **453**, 1023 (2008).

[10] C. Bonato, F. Haupt, S. S. R. Oemrawsingh, J. Gudat, D. Ding, M. P. van Exter, and D. Bouwmeester, Physical Review Letters **104**, 160503+ (2010).

[11] B. Urbaszek, X. Marie, T. Amand, O. Krebs, P. Voisin, P. Maletinsky, A. Högele, and A. Imamoglu, Rev. Mod. Phys. **85**, 79 (2013).

[12] E. A. Chekhovich, M. N. Makhonin, A. I. Tartakovskii, A. Yacoby, H. Bluhm, K. C. Nowack, and L. M. K. Vandersypen, Nat Mater **12**, 494 (2013).

[13] J. Houel, A. V. Kuhlmann, L. Greuter, F. Xue, M. Poggio, B. D. Gerardot, P. A. Dalgarno, A. Badolato, P. M. Petroff, A. Ludwig, D. Reuter, A. D. Wieck, and R. J. Warburton, Phys. Rev. Lett. **108**, 107401 (2012).

[14] A. V. Kuhlmann, J. Houel, A. Ludwig, L. Greuter, D. Reuter, A. D. Wieck, M. Poggio, and R. J. Warburton, Nat Phys **9**, 570 (2013).

[15] N. G. Stoltz, M. Rakher, S. Strauf, A. Badolato, D. D. Lofgreen, P. M. Petroff, L. A. Coldren, and D. Bouwmeester, Applied Physics Letters **87**, 031105+ (2005).

[16] S. Strauf, N. G. Stoltz, M. T. Rakher, L. A. Coldren, P. M. Petroff, and D. Bouwmeester, Nature Photonics **1**, 704 (2007).

[17] M. T. Rakher, N. G. Stoltz, L. A. Coldren, P. M. Petroff, and D. Bouwmeester, Physical Review Letters **102**, 097403+ (2009).

[18] C. Bonato, D. Ding, J. Gudat, S. Thon, H. Kim, P. M. Petroff, M. P. van Exter, and D. Bouwmeester, Applied Physics Letters **95**, 251104+ (2009).

[19] M. P. Bakker, A. V. Barve, A. Zhan, L. A. Coldren, M. P. van Exter, and D. Bouwmeester, Applied Physics Letters **104**, 151109+ (2014).

[20] A. Auffèves-Garnier, C. Simon, J.-M. Gérard, and J.-P. Poizat, Phys. Rev. A **75**, 053823 (2007).

[21] E. Waks and J. Vuckovic, Phys. Rev. Lett. **96**, 153601 (2006).

[22] S. M. Sze and K. K. Ng, *Physics of Semiconductor Devices*, 3rd ed. (Wiley-Interscience, 2006).

[23] R. D. Twesten, D. M. Follstaedt, K. D. Choquette, and R. P. Schneider, Applied Physics Letters **69**, 19 (1996).

[24] C. I. H. Ashby, J. P. Sullivan, P. P. Newcomer, N. A. Missert, H. Q. Hou, B. E. Hammons, M. J. Hafich, and A. G. Baca, Applied Physics Letters **70**, 2443 (1997).

[25] E. I. Chen, N. Holonyak, and S. A. Maranowski, Applied Physics Letters **66**, 2688 (1995).

[26] C. Arnold, V. Loo, A. Lemaître, I. Sagnes, O. Krebs, P. Voisin, P. Senellart, and L. Lanco, Phys. Rev. X **4**, 021004 (2014).

[27] P. F. Braun, B. Urbaszek, T. Amand, X. Marie, O. Krebs, B. Eble, A. Lemaitre, and P. Voisin, Physical Review B **74**, 245306+ (2006).

[28] A. I. Tartakovskii, T. Wright, A. Russell, V. I. Fal'ko, A. B. Van'kov, J. Skiba-Szymanska, I. Drouzas, R. S. Kolodka, M. S. Skolnick, P. W. Fry, A. Tahraoui, H.-Y. Liu, and M. Hopkinson, Phys. Rev. Lett. **98**, 026806 (2007).

[29] P. Maletinsky, A. Badolato, and A. Imamoglu, Phys. Rev. Lett. **99**, 056804 (2007).

[30] B. Eble, O. Krebs, A. Lemaître, K. Kowalik, A. Kudelski, P. Voisin, B. Urbaszek, X. Marie, and T. Amand, Phys. Rev. B **74**, 081306 (2006).

[31] C. Latta, A. Hogele, Y. Zhao, A. N. Vamivakas, P. Maletinsky, M. Kroner, J. Dreiser, I. Carusotto, A. Badolato, D. Schuh, W. Wegscheider, M. Atature, and A. Imamoglu, Nat Phys **5**, 758 (2009).

[32] A. Högele, M. Kroner, C. Latta, M. Claassen, I. Carusotto, C. Bulutay, and A. Imamoglu, Phys. Rev. Lett. **108**, 197403 (2012).

[33] See Supplemental Material at [URL will be inserted by publisher] for details on photocurrent measurements with lasers of different wavelengths, and a comparison between photoluminescence measured at the microcavity and measured in a region without oxide aperture.